Error Modelling of Pseudolite Signal Reception on Conducting Aircraft Surfaces

eingereicht von

Dipl.-Ing. Robert Biberger

Vollständiger Abdruck der an der Fakultät für Bauingenieur- und Vermessungswesen der Universität der Bundeswehr München zur Erlangung des akademischen Grades eines Doktors der Ingenieurwissenschaften (Dr.-Ing.) eingereichten Dissertation.

Vorsitzender:	Univ.-Prof. Dr.-Ing. Helmut Mayer
1. Berichterstatter:	Univ.-Prof. Dr.-Ing. Günter Hein
2. Berichterstatter:	Univ.-Prof. Dr.-Ing. Bernd Eissfeller
3. Berichterstatter:	Prof. Per Enge (Stanford University, USA)

Die Dissertation wurde am 13. Juni 2006 bei der Universität der Bundeswehr München, Werner-Heisenberg-Weg 39, D-85577 Neubiberg eingereicht.

Tag der mündlichen Prüfung: 8. September 2006

ABSTRACT

Airport Pseudolites (APLs) can help to accomplish the stringent performance requirements towards GNSS based Category II and III approach systems. The application of APLs has the potential to improve system performance with respect to all four RNP parameters i.e. accuracy, integrity, continuity and availability.

However, due to error effects which have to be considered and modelled in a different way than for satellite born GNSS navigation signals, a more precise positioning using APL measurements cannot be taken for granted. Among those are signal creeping and the resulting multipath propagation on conducting aircraft surfaces.

Signal creeping and multipath propagation can occur when environmental features (like conducting aircraft surfaces) cause diffraction. Diffracted signals have a longer signal path than direct line-of-sight signals because they creep on the conducting surfaces and experience therefore a so-called signal path extension. Furthermore, diffracted replica signals could cause multipath effects when they arrive at the GNSS/APL receiving antenna. These signals, in combination with the original line-of-sight signal, could cause distortion of the correlation function and hence generate errors in receiver code- and carrier-phase measurements which cannot be mitigated by differential techniques.

The research aim of this PhD thesis is to enhance the understanding of APL signal reception by top-mounted aircraft antennas. The work presented in this dissertation describes the research, development, implementation and validation of

- a real test bed for demonstrating diffraction phenomena originating on conducting aircraft surfaces (see chapter 3),
- an APL signal propagation model based on a numerical solution of Maxwell’s full set of equations considering material parameters for analysis of multipath propagation field behaviour on conducting aircraft surfaces (see chapter 4),
- a correlator/discriminator model that processes the results of the numerical APL signal propagation model into resultant error effects (see chapter 4), and
- an analytical error model for APL signal reception on cylindrical and box-shaped aircraft bodies (see chapter 5).

ZUSAMMENFASSUNG

Airport Pseudolites (APLs) können dazu beitragen, die hohen Leistungsanforderungen an ein GNSS basiertes Kategorie II und III Anflug System zu erfüllen. Durch APLs ist es möglich, die Systemleistung hinsichtlich aller vier RNP Parameter (Genauigkeit, Integrität, Kontinuität und Verfügbarkeit) zu steigern.

Es treten jedoch Fehlereffekte auf, die anders berücksichtigt und modelliert werden müssen als dies für herkömmliche GNSS Navigationssignale erforderlich ist. Damit kann eine genauere Positionierung unter Verwendung von APL Messungen nicht als selbstverständlich betrachtet werden. Zu diesen Fehlern gehören das Signalkriechen und die daraus resultierende Mehrwegeausbreitung an leitenden Flugzeugoberflächen.

Signalkriechen und Mehrwegeausbreitung entstehen, wenn die Umgebungseigenschaften (wie leitende Flugzeugoberflächen) eine Beugung des Signals hervorrufen. Gebeugte Signale haben einen längeren Signalweg als direkte Signale, da sie auf den leitenden Oberflächen entlang kriechen und der Signalweg dadurch verlängert wird. Darüber hinaus können durch zusätzliche Signale, die aufgrund der Beugung entstanden sind, Mehrwegeeffekte an der GNSS/APL Empfangsantenne auftreten. Mehrwegesignale können eine Verformung der Korrelationsfunktion hervorrufen und dadurch die Kode- und Trägerphasenmessungen des Empfängers verfälschen. Diese Fehler sind nicht durch differentielle Verfahren korrigierbar.

Das wissenschaftliche Ziel der Doktorarbeit ist es, die Kenntnisse über den APL Signalempfang an der Flugzeugoberseite auszubauen. Die Dissertation beinhaltet die Untersuchung, Entwicklung, Ausführung und Überprüfung

- einer Versuchseinrichtung zur Demonstration von Beugungseffekten an leitenden Flugzeugoberflächen (siehe Kapitel 3),
- eines APL Signalausbreitungsmodells, das auf der vollständigen numerischen Lösung der Maxwell Gleichungen unter Berücksichtigung von Materialparametern basiert und die Mehrwegeausbreitung an leitenden Flugzeugoberflächen beschreibt (siehe Kapitel 4),
- eines Korrelator/Diskriminator Modells, welches die Ergebnisse des numerischen APL Signalausbreitungsmodells weiterverarbeitet und die resultierenden Fehlereffekte aufzeigt (siehe Kapitel 4) und
- eines analytischen Fehlermodells für den APL Signalempfang an zylindrischen und kastenförmigen Flugzeugrümpfen (siehe Kapitel 5).

TABLE OF CONTENTS

LIST OF FIGURES

LIST OF TABLES

LIST OF SYMBOLS

Fundamentals

ϕ	phase shift of the replica code or chip offset
ϕ'	code-phase
I	in-phase samples
p_{REC}	received code
p_{REP}	generated code replica
Q	quadrature-phase samples
R	correlation function
T	integration time

Experimental Validation

ϕ_{CYL}^{APL}	carrier-phase measurements of the cylinder antenna to the APL
ϕ_{REF}^{APL}	carrier-phase measurements of the reference antenna to the APL
ϕ_{CYL}^{GPS}	measured carrier-phase residuals of the cylinder antenna to the reference satellite
ϕ_{REF}^{GPS}	measured carrier-phase residuals of the reference antenna to the reference satellite
C/N_0	carrier power to noise power spectral density ratio; [dBHz]
$DD_{CYL-REF}^{GPS-APL}$	carrier-phase double-differences between the cylinder and the reference station measurements

Numerical Error Modelling

α	angle between the propagation direction of the emitted APL signal **s** and the horizontal projection of the longitudinal axis of the fuselage
β	elevation angle of the aircraft
γ	constant
ε_r	relative permittivity
θ	pitch angle of the aircraft, positive angles are associated with an ascending aircraft
κ	(electric) conductivity; $\left[1/\Omega\text{m}\right]$
μ_r	relative permeability

ρ	material density; $[kg/m^3]$
ϕ_{del}	carrier-phase delay
φ	bank angle of the aircraft, positive angles are associated with a left banking aircraft
A	amplitude
c_j	code sequence
d	correlator spacing; [chips]
f_C	chipping rate, f_C =10.23 MHz
f_{L1}	carrier frequency, f_{L1} =1575.42 MHz
p	single chip function at RF level
ΔR	difference of the absolute values of the correlation functions
R_{body}	correlation function for the body case
R_{empty}	correlation function for the empty case
R_I	real part of the correlation function R
R_Q	imaginary part of the correlation function R
s	emitted APL signal
S	S-function
t	time; [s]
T_C	chip length; [s]

Analytical Error Modelling

$-\alpha_n$	zeros of the Airy function
$-\alpha'_n$	zeros of the Airy function derivative
δ	geometric path delay; [m]
$\tilde{\delta}$	geometric path delay; [chips]
Δ	signal path extension; [m]
η	multipath relative amplitude or amplitude ratio between two signal components
λ	wave length; [m]
ρ	distance between the centre of the cylinder and the antenna phase centre; [m]
ϑ	phase tracking error; [m]

ϕ	angle between the x-axis and the line between the centre of the cylinder and the antenna phase centre
χ	multipath relative phase
Ω_n^e	attenuation constant for the electric polarisation
Ω_n^m	attenuation constant for the magnetic polarisation
a	cylinder radius; [m]
Ai	Airy function
Ai'	Airy function derivative
D_n^e	amplitude weighting factor for the electric polarisation
D_n^m	amplitude weighting factor for the magnetic polarisation
E_y	electric polarisation in the y-direction
H_y	magnetic polarisation in the y-direction
k	wave number
$\mathbf{r}$	vector describing the direction of the longitudinal axis of the aircraft
$\mathbf{R_x}$	rotation matrix about the x-axis
$\mathbf{R_y}$	rotation matrix about the y-axis
$\mathbf{R_z}$	rotation matrix about the z-axis
$\mathbf{s}$	vector describing the direction of the APL signal rays
V_y	field component in the y-direction
w	distance from the phase centre of the antenna to the rounded edge of the fuselage; [m]

Conclusion

$\Delta_{\text{worst case, cyl}}$	maximum ranging error due to SPE for cylindrical aircraft bodies
$\Delta_{\text{worst case, box}}$	maximum ranging error due to SPE for box-shaped aircraft bodies
$\Delta_{\text{stable approach, cyl}}$	ranging error due to SPE for cylindrical aircraft bodies on a stable landing approach
$\Delta_{\text{stable approach, box}}$	ranging error due to SPE for box-shaped aircraft bodies on a stable landing approach
ψ	azimuth

Classical Electrodynamics

δ	diffusion constant
ε	dielectric constant; permittivity
ε_0	dielectric constant of vacuum; $\cong 8.854 \cdot 10^{-12}\,\mathrm{As/Vm}$
κ	(electric) conductivity; $\left[1/\Omega\mathrm{m}\right]$
μ	permeability
μ_0	permeability of vacuum; $4\pi \cdot 10^{-7}\,\mathrm{Vs/Am}$
ρ	charge density; $\left[\mathrm{As/m^3}\right]$
χ_e	dielectric susceptibility
χ_m	magnetic susceptibility
B	magnetic flux; $\left[\mathrm{T}\right] = \left[\mathrm{Vs/m^2}\right]$
c	speed of light
c_0	vacuum speed of light; $c = 2.99792458 \cdot 10^8\,\mathrm{m/s}$
C	constitutive matrix (6x6)
D	electric flux; $\left[\mathrm{C/m^2}\right] = \left[\mathrm{As/m^2}\right]$
E	electric field strength; $\left[\mathrm{V/m}\right]$
E’	normalised electric field strength
H	magnetic field strength; $\left[\mathrm{A/m}\right]$
H’	normalised magnetic field strength
J	current density; $\left[\mathrm{A/m^2}\right]$
$\mathbf{J}_E$	impressed current density
$\mathbf{J}_K$	convection current density
$\mathbf{J}_L$	conduction current density
L	matrix (3x3) with elements of constitutive parameters
M	matrix (3x3) with elements of constitutive parameters
P	matrix (3x3) with elements of constitutive parameters
Q	matrix (3x3) with elements of constitutive parameters
U	polarisation vector
v	velocity vector

$\mathbf{W}$	magnetisation vector
Y_0	admittance
Z_0	wave impedance

Finite Integration Technique

δ	Kronecker delta
$\mathbf{\Omega}$	finite volume
A_i	elementary area
$\tilde{A}_i$	elementary area on dual grid
$\mathbf{b}$	vector holding the magnetic (grid)-flux
b_i	magnetic (grid)-flux
$\mathbf{C}$	discrete curl operator
$\tilde{\mathbf{C}}$	discrete curl operator on dual grid
$\mathbf{d}$	vector holding the electric (grid)-flux
d_i	electric (grid)-flux
$\mathbf{D}_{\varepsilon}$	discrete material matrix of averaged permittivity
$\mathbf{D}_{\kappa}$	discrete material matrix of averaged (electric) conductivity
$\tilde{\mathbf{D}}_{\mu}$	discrete material matrix of averaged permeability on dual grid
$\mathbf{D}_A$	diagonal matrix of elementary areas
$\tilde{\mathbf{D}}_A$	diagonal matrix of elementary areas on dual grid
$\mathbf{D}_s$	diagonal matrix of elementary lines
$\tilde{\mathbf{D}}_s$	diagonal matrix of elementary lines on dual grid
e	vector holding the electric (grid)-voltage
e_i	electric (grid)-voltage
G	FIT-grid
$\tilde{G}$	dual FIT-grid
h_i	magnetic (grid)-voltage
j_i	total electric (grid)-current
$\mathbf{j}$	vector holding the total electric (grid)-current

$\mathbf{j}_l$	vector holding the conduction electric (grid)-current
L_i	elementary line
$\tilde{L}_i$	elementary line on dual grid
P_i	grid point
q_i	discrete charges
$\mathbf{S}$	discrete divergence operator
$\tilde{\mathbf{S}}$	discrete divergence operator on dual grid
$-\mathbf{S}^{\mathbf{T}}$	discrete gradient operator
$-\tilde{\mathbf{S}}^{\mathbf{T}}$	discrete gradient operator on dual grid
V_i	elementary volume

Pulsing of APL Signals

$n_{chips/pulse}$	number of chips per pulse
$n_{chips/\mathrm{s}}$	number of chips per second
n_{pulse}	number of pulses per second

Modelling the APL RF Signal

c_e	emitted code as a function of code-phase
f_P	frequency of the carrier-phase; [1/s]
s_e	emitted signal in the I-channel

LIST OF ACRONYMS

Abs	Absolute
APL	Airport Pseudolite
BOC	Binary Offset Carrier
BPSK	Binary Phase Shift Keying
BW	Bandwidth
CAD	Computer Aided Design
CAT	Category
CST	Computer Simulation Technology
DGNSS	Differential Global Navigation Satellite System
DLL	Delay Lock Loop
DSSS	Direct Sequence Spread Spectrum
E	Electric
FAA	Federal Aviation Administration
FD	Finite Difference
FE	Finite Element
FIR	Finite Impulse Response
FIT	Finite Integration Technique
FLL	Frequency Lock Loop
GDOP	Geometric Dilution of Precision
GIP	Government Industry Partnership
GNSS	Global Navigation Satellite System
GO	Geometrical Optics
GPS	Global Positioning System
GSV	GPS Silicon Valley
GTD	Geometrical Theory of Diffraction
HF	High Frequency
ICAO	International Civil Aviation Organisation
ICD	Interface Control Document
IF	Intermediate Frequency
ILS	Instrument Landing System
INS	Inertial Navigation System
LAAS	Local Area Augmentation System

LNA	Low-Noise-Amplifier
LO	Local Oscillator
LOS	Line-of-Sight
ML	Maximum Likelihood
NCO	Numerical Controlled Oscillator
PC	Personal Computer
PDC	Pulse Duty Cycle
PL	Pseudolite
PLL	Phase Lock Loop
PPS	Pulse Per Second
PRN	Pseudo Random Noise
PRU	Pulser RF Unit
PSG	Pulse Sequence Generator
R&D	Research and Development
RF	Radio Frequency
RNP	Required Navigation Performance
RTCA	Radio Technical Commission for Aeronautics
RTCM	Radio Technical Commission for Maritime Services
SIS	Signal-in-Space
SNR	Signal-to-Noise Ratio
SOC	Sinusoidal Offset Carrier
SPE	Signal Path Extension
VHF	Very High Frequency
WAAS	Wide Area Augmentation System
WB	Wide Band

1 Introduction

1.1 APL and LAAS

Aviation authorities including the International Civil Aviation Organisation (ICAO) and the United States Federal Aviation Administration (FAA) have been working to define the next generation of aircraft navigation aids based on the Global Navigation Satellite System (GNSS) [*Cobb et al., 1999*]. The current proposal for enroute navigation, known as the Wide Area Augmentation System (WAAS) is entirely satellite-based. However, the system proposed for navigation during takeoff and landing, known as the Local Area Augmentation System (LAAS), requires ground equipment at each airport. The LAAS ground equipment includes an elaborate reference station to generate differential GNSS (DGNSS) corrections, and a Very High Frequency (VHF) data link transmitter to send them to nearby aircraft. It may also include a monitor station for monitoring system performance and one or more GNSS-band transmitters known as Airport Pseudolites (APLs) to accomplish the stringent performance requirements in system availability towards Category (CAT) II and III operations (see Table 1-1). Figure 1-1 shows a simplified block diagram of a LAAS architecture for the Global Positioning System (GPS).

Each APL provides an additional GNSS-like signal for nearby aircraft to use in their navigation solutions. In general, four such signals are needed to achieve a basic position fix. One or more additional signals may be needed to achieve all the elements of Required Navigation Performance (RNP) specified by ICAO for aircraft on final landing approach. Simulations of satellite visibility frequently find that the number of GNSS satellite signals available at certain places and times is lower than the number needed for RNP. Each APL adds one more signal to the number available. To achieve the level of availability required by RNP one or more APLs may be needed. APLs may serve as an augmentation with regard to availability and continuity. Although the benefit of an APL is allocated toward improving availability in RNP calculations, each APL should also provide an improvement in navigation accuracy. GNSS satellite signals are all transmitted from above the aircraft's horizon, but APL signals are transmitted from below the horizon. Therefore, adding an APL to the navigation solution improves its Geometric Dilution of Precision (GDOP) which should result in a smaller position error for the same number of signals. The greatest improvement is usually in the vertical error which is the most critical for aircraft on final landing approach. However, due to a few effects that have to be considered and modelled in a different way than for GNSS signals (e.g. APL tropospheric delay), a more precise positioning using APL measurements cannot be taken for granted.

This PhD thesis addresses APLs from the perspective of signal reception considerations on aircraft bodies. Reception of the APL signal by a user will be affected by the aircraft antenna location and the APL position relative to its approach path [*Bryant*, *1995*]. Ideally, the APL signals would be received by a top-mounted antenna, the same one used for receiving the satellite signals. This could be accommodated by locating the APL transmitting antenna at an appropriate elevation and offset from the glide slope. Even if the line-of-sight (LOS) to the APL is below the aircraft antenna horizon, the increased signal level in the vicinity of the APL will tend to cancel the loss in antenna gain for signals near or below the horizon. On the basis of multiple flight tests it was clear to see that the signal is strong enough that even a loss in the LOS to the APL does not interrupt signal reception because of diffraction phenomena [*Biberger et al.*, *2005*]. It seems that the APL signal creeps on the conducting surface of the aircraft body. However, this effect produces unwanted signal path extensions and additional signal rays leading to multipath. Resulting measurement errors (code- and carrier-phase biases) originating locally around the receiver antenna cannot be mitigated by differential processing and hence contribute to remaining (uncorrected) navigation errors. Therefore, these errors must be analysed to guarantee a precise positioning.

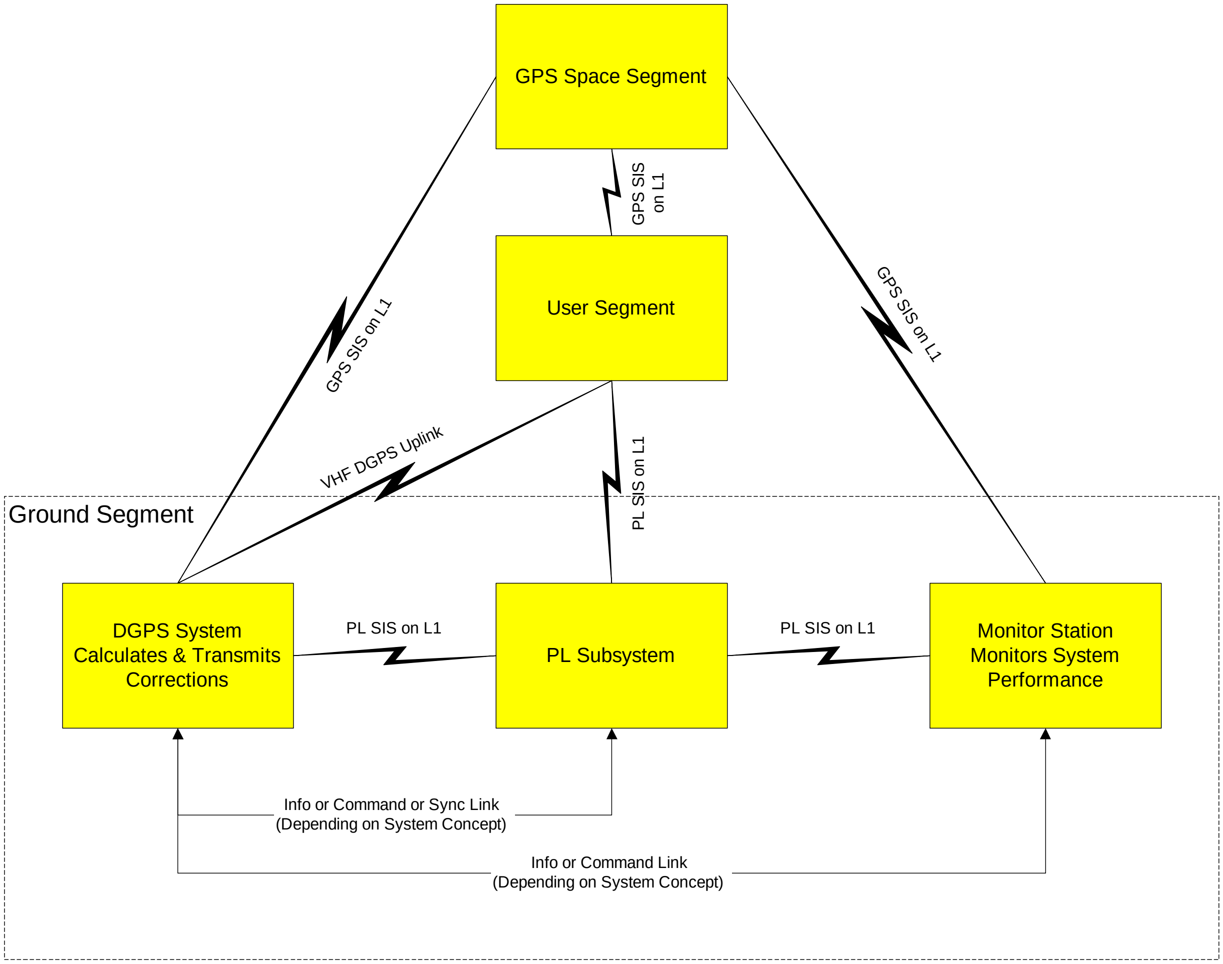

Figure 1-1: Diagram of a possible LAAS architecture [*Werner and Ott, 1997*]

Operation	Accuracy (horizontal 95%)	Accuracy (vertical 95%)	Integrity	Time-to-alert	Continuity Risk	Availability
CAT I	16 m	6 m to 4 m	2 x 10^{-7} / approach (150 sec)	6 sec	8 x 10^{-6} / 15 sec	0.99 to 0.99999
CAT II/IIIa	6.9 m	2 m	10^{-9} / 15 sec	1 sec	4 x 10^{-6} / 15 sec	0.99 to 0.99999
CAT IIIb	6.2 m	2 m	10^{-9} / 30 sec (lateral) 10^{-9} / 15 sec (vertical)	1 sec	2 x 10^{-6} / 30 sec (lateral) 2 x 10^{-6} / 15 sec (vertical)	0.99 to 0.99999

Table 1-1: GNSS performance requirements for CAT approaches [*Olson, 2003*]

1.2 Objectives and Structure of this Thesis

For a proper understanding of diffraction phenomena on conducting aircraft surfaces and the impact on navigation receivers, the electromagnetic properties of the transmitted signal, the receiver signal processing and the nature of electromagnetic fields and their behaviour in the presence of media have to be known. Chapter 2 deals consequently with APL signal characteristics and GPS/APL receiver signal processing. Classical electrodynamics and its numerical treatment which will be required in later developments can be found in the appendices 8.1 and 8.2. Furthermore, the appendix 8.3 contains a hardware description of an APL focused on transmitting pulsed signals.

In order to demonstrate and validate diffraction phenomena originating on conducting aircraft surfaces during APL signal propagation, an aluminium cylinder test bed – which is prescribed in chapter 3 – has been developed. The cylinder which represents a simplified part of an aircraft body is radiated with the APL signal. For analysis, signal power and carrier-phase measurements on the cylinder surface were performed with a navigation receiver. The obtained data are used for verifying the results of the numerical simulation in chapter 4.

In chapter 4 the navigation signal propagation is analysed by a very complete and complex three-dimensional numerical simulation with Computer-Aided Design (CAD) generated parts of aircraft bodies. The propagation of the navigation signal is represented by a numerical solution of Maxwell's full set of equations. They are solved by using the Finite Integration Technique (FIT). The results provide the input for a GPS/APL receiver model for the visualisation and generation of resultant receiver error measurements.

This numerical approach requires a tremendous computing effort and real time processing is not possible. In particular, it is hard to assess a qualitative analysis of the impact of certain parameters. Therefore, a three-dimensional analytical propagation model is desirable. Based on the Geometrical Theory of Diffraction (GTD), a two-dimensional solution for the conducting circular cylinder is given and applied in chapter 5. Signal creeping, signal interference and multipath propagation on a conducting cylindrical aircraft surface will be discussed. This two-dimensional model for the circular cylinder is the key for a three-dimensional analytical code and carrier-phase delay error model for pseudolite signal reception on conducting cylindrical and box-shaped aircraft bodies. The error model is verified by comparing it to the results of the numerical simulation.

1.3 Current Status of LAAS and Pseudolites

LAAS is a critical component of the FAA's plan to transition from a ground-based navigation and landing system to a satellite-based navigation system [*GAO, 2005*]. LAAS will provide lateral, vertical and area navigation in terminal areas and precision approach and landing service for CAT I/II/III at an airport. It will broadcast highly accurate information to aircraft in a flight's final phases, providing more precise approach paths than the current Instrument Landing System (ILS), reducing the required separation between incoming aircraft and increasing airspace capacity. LAAS will also provide airports with precision approach capability for all runways, eliminating the need for multiple ILS installations.

The program consists of three parts:

- The Government Industry Partnership (GIP)
- LAAS Category I System Design, Development and Production
- LAAS CAT II/III Research and Development (R&D) followed by full-scale development

The LAAS GIP was established to develop a non-Federal CAT I system under the FAA type acceptance process. The GIP activities have produced engineering prototypes; however, the GIP systems have not met type acceptance criteria at this time and cannot be used operationally.

The LAAS CAT I Development Phase commenced April 2003 with a contract award to Honeywell.

Based on results of the LAAS CAT II/III R&D efforts, the FAA will make a decision on the feasibility of awarding a full-scale development and production contract.

LAAS CAT I

During the first months of the CAT I contract, it became apparent that the work required to resolve the integrity risks would take longer than originally estimated by Honeywell. FAA and the contractor agreed that these difficulties have resulted from a lack of communication. When the contract was awarded, FAA assumed that LAAS was 80 percent developed but later discovered that only about 20 percent was complete. Poorly established requirements resulted in the addition of 113 new requirements to the initial specification, entailing unplanned work including significant software and hardware changes. In addition, FAA underestimated LAAS' software complexity because it inadequately assessed the system's technology maturity. In particular, the agency misunderstood the potential for radio interference through the atmosphere which could limit LAAS' operations. FAA therefore suspended funding in fiscal year 2005 and used the remaining $18 million to resolve the integrity requirement problem, among other things, in fiscal year 2004. Although FAA had not requested funding, Congress did approve an additional $10 million for LAAS in fiscal year 2005. The FAA continued to work on resolving LAAS integrity and safety assurance issues during fiscal year 2005. During fiscal year 2006, the program office will develop a business case justification on whether to continue the LAAS program.

LAAS CAT II/III

The FAA identified preliminary integrity, continuity and availability allocations and discussed them with the aviation industry at a Radio Technical Commission for Aeronautics (RTCA) working group meeting. The FAA identified different possible approaches for LAAS CAT II/III development, one of which depends significantly on the integration of aircraft avionics and capabilities like inertial systems and enhanced vision systems. The FAA also entered into a contract with Boeing to support “Trade-off Studies” where Boeing will provide analysis toward completion of LAAS Ground Facility and aircraft requirements allocation and validation. These analyses are ongoing and will support the development of Minimum Aviation System Performance Standards by RTCA.

APLs have been an integral part for LAAS as an availability component during the time of this work. However, recently they have been removed from the latest version of the GNSS Based Precision Approach Local Area Augmentation System Signal-in Space Interface Control Document (ICD) (RTCA/DO-246C) because of missing regulations with regard to the airborne receivers and unsolved concerns about jamming caused by APLs. New signal structures and the development of more flexible navigation receivers should give them a more important role in the future.

2 Fundamentals

2.1 APL Signal Characteristics

The prevailing APL signal broadcast is designed to minimise GPS receiver hardware modifications [*RTCA*, *2001*]. The basic signal characteristic is similar to GPS, using the same frequency and modulation technique. In addition, the code-phase timing is maintained close to GPS time to provide a ranging capability. However, the APL signal structure must be modified with respect to the GPS signal structure to minimise the interference to the GPS signals.

2.1.1 Background – Near-Far Problem

Because the GPS satellites are far away, and because their antenna broadcast beam is shaped, the received GPS signal power varies only slightly over the earth coverage (above 5 ° elevation angle) [*Van Dierendonck et al.*, *1997*]. However, because the APLs are near-by, the APL received power varies much stronger with the distance between the user's receiving antenna and the APL. Thus, if the average APL received signal power is made to match that of the satellite at one range, it will dominate at another range while being too weak at yet another. The effect of this is that, unless carefully designed, the APL signal will act as a strong jammer to the satellite signals at short range and the APL signal will be too weak to be useful at long range. To solve this near-far problem, the APL signals are pulsed, a Wideband (WB) Pseudorandom Noise (PRN) code is selected as spreading code and the carrier frequency can be shift with respect to the code frequency.

2.1.2 Preliminary APL Signal Specification

This section specifies the preliminary signal structure of the proposed ground-based augmentation APL described in the GNSS Based Precision Approach Local Area Augmentation System Signal-in Space Interface Control Document [*RTCA*, *2001*]. It should be noted that only those signal characteristics are given here which are of importance to this work.

Carrier Frequency and Spectrum

The LAAS APL Signal-in-Space (SIS) is centred at the frequency 1575.42 MHz which is the GPS L1 frequency.

Modulation

The composite binary signal (APL-code and navigation data) is impressed upon the L1 carrier in a process called Binary Phase Shift Keying (BPSK). At binary code transitions from 0 to1, or from 1 to 0, the phase of the carrier is shifted by 180°.

Polarisation

The APL broadcast signal is vertically polarised to minimise the effects of multipath and to maximise reception power into top-mounted antennas [*Van Dierendonck et al.*, *1997*]. The multipath advantage is because, theoretically, only the horizontal component of a signal reflects from an ideally reflective surface. The signal reception advantage is because the reception antenna is basically vertically polarised at negative elevation angles.

Spreading Code

The APL-code is a ranging code of seven days in length at a chipping rate of 10.23 MHz (WB code or P-code).

Signal Pulsing

The APL SIS is transmitted as a pulsed signal. The pulses are generated coherently to the chips of the WB code. A pseudorandom pulse sequence is used to prevent the user receiver from locking on to the pulse pattern. The average pulse repetition rate is sufficiently high so that the APL signal will appear to be continuous in the user's receiver post correlation signal processing, while appearing to be pulsed during wideband processing prior to correlation. The pulse sequence includes at least one pulse every millisecond. For the required low duty cycle, a relatively high pulse repetition rate results in relatively narrow pulses (on the order of a few microseconds). Details of the pseudorandom pulse sequence are documented in the ICD [*RTCA, 2001*].

The down side of pulsing is that GNSS receivers can exhibit pseudorange bias errors when receiving pulsed signals of high peak amplitude [*Van Dierendonck, 1998*]. These errors are a function of the received signal strength. Only a careful design of the user received dynamic range of the APL signal level will make the bias controllable. Note that the P-code is much less affected than the C/A-code.

The appendix 8.3 contains a detailed treatment of the pulsing of Pseudolite (PL) signals.

2.2 GPS/APL Receiver Signal Flow

2.2.1 Generic GPS/APL Receiver

A generic GPS/APL receiver would consist of the following functional elements as shown in Figure 2-1 [*Hannah, 2001*]: antenna, Radio Frequency (RF) amplification and filtering, reference oscillator, frequency synthesis, down-conversion, Intermediate Frequency (IF) section, signal processing and application processing.

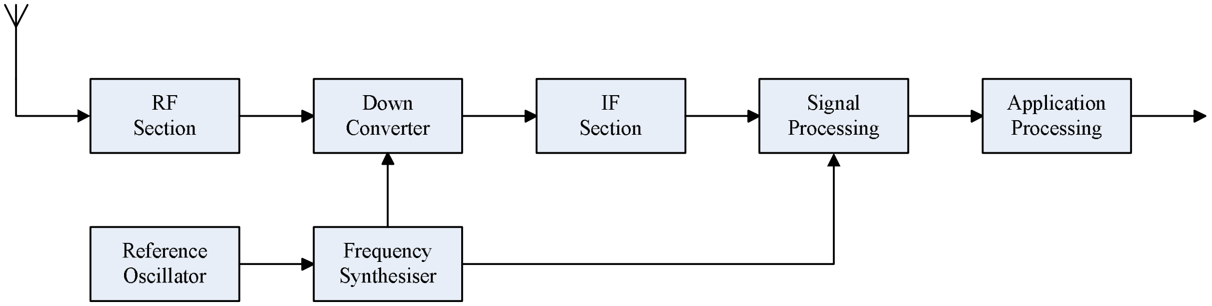

Figure 2-1: Generic GPS/APL receiver [*Hannah, 2001*]

These functions are described in various excellent GPS-specific sources including [*Van Dierendonck, 1995*] and [*Ward, 1996*]. All functions are briefly described here for completeness, but it is the signal processing function that forms the core of a GPS/APL receiver and it is this function that is the focus of later sections.

Antenna and RF Section

The GPS signals, received from the GPS satellites, are of very low power. The antenna and RF sections therefore need to maximise the signal reception. The antenna needs to have a near hemispherical gain pattern, so as to maximise the number of satellites for tracking. The antenna may be designed as an active device with some amplification occurring before the signal is sent to the RF section. The RF section usually consists of filtering and amplification functions. The filtering is used to reduce the effects of out-of-band noise and interference. The amplification is achieved with a Low-Noise-Amplifier (LNA), with the gain selected so as to establish the designed receiver noise figure.

Reference Oscillator and Frequency Synthesis

The reference oscillator provides the time and frequency reference for the GPS/APL receiver. The parameters of the reference oscillator (size, stability, and phase noise) are trade-offs between cost and performance. The higher the stability, the more costly the oscillator becomes. In GPS receivers the reference oscillator is used by the frequency synthesiser to generate all Local Oscillators (LO) and clocks.

Down conversion and IF

The local oscillators are used in the down converter to convert the RF signal down to a lower IF. The IF section provides additional amplification, filtering and provides a conditioned signal that can be used by the signal processing section.

Signal Processing

The signal processing section is really the core function in a GPS/APL receiver. It performs multi-channel acquisition and carrier/code tracking of satellites and APLs, navigation data demodulation, code-phase (pseudorange), carrier-phase (delta pseudorange) and carrier frequency (integrated Doppler) measurements, in addition to extracting the Signal-to-Noise Ratio (SNR) of the received signals.

Application Processing

The last function is called application processing, thus covering a broad set of applications. The application may be that of navigation processing, differential surveying, time transfer, or simply data collection.

2.2.2 Code and Carrier Tracking

GPS/APL signal acquisition and tracking is a two-dimensional process [*Hannah, 2001*]. The receiver must correlate the received code p_{REC} (plus noise) with a shifted internally generated code replica p_{REP} as well as maintain lock with the carrier (including Doppler) of the signal. In the code-phase dimension, when the code-phases are matched there is maximum correlation. Minimum correlation occurs when the replica code is offset by more than one chip. The correlation function R is given in equation (2-1).

$$R(\phi) = \int_{\phi'=0}^{T} p_{REC}(\phi') p_{REP}(\phi'+\phi) d\phi', \qquad (2\text{-}1)$$

where ϕ' is the phase of the code, ϕ is the phase shift of the replica code and T is the integration time. The code-phase tracking loop is of a similar form to that used in other Direct Sequence Spread Spectrum (DSSS) systems—a Delay Lock Loop (DLL). The DLL used can be either coherent or noncoherent. The coherent DLL requires parallel tracking of the carrier-phase whilst the noncoherent DLL requires no carrier tracking. The form of the DLL is determined by the type of discriminator used.

In addition to tracking the signal in the code-phase dimension, the receiver must also track the signal in the carrier-phase dimension. The tracking of the carrier-phase can be achieved by a variety of tracking loops that are of either Phase Lock Loop (PLL), Costas PLL, or Frequency Lock Loop (FLL) form. In each of these forms, there is a variety of discriminator functions that can be utilised. A generic form of the carrier and code tracking loops is shown in Figure 2-2 [*Hannah, 2001*].

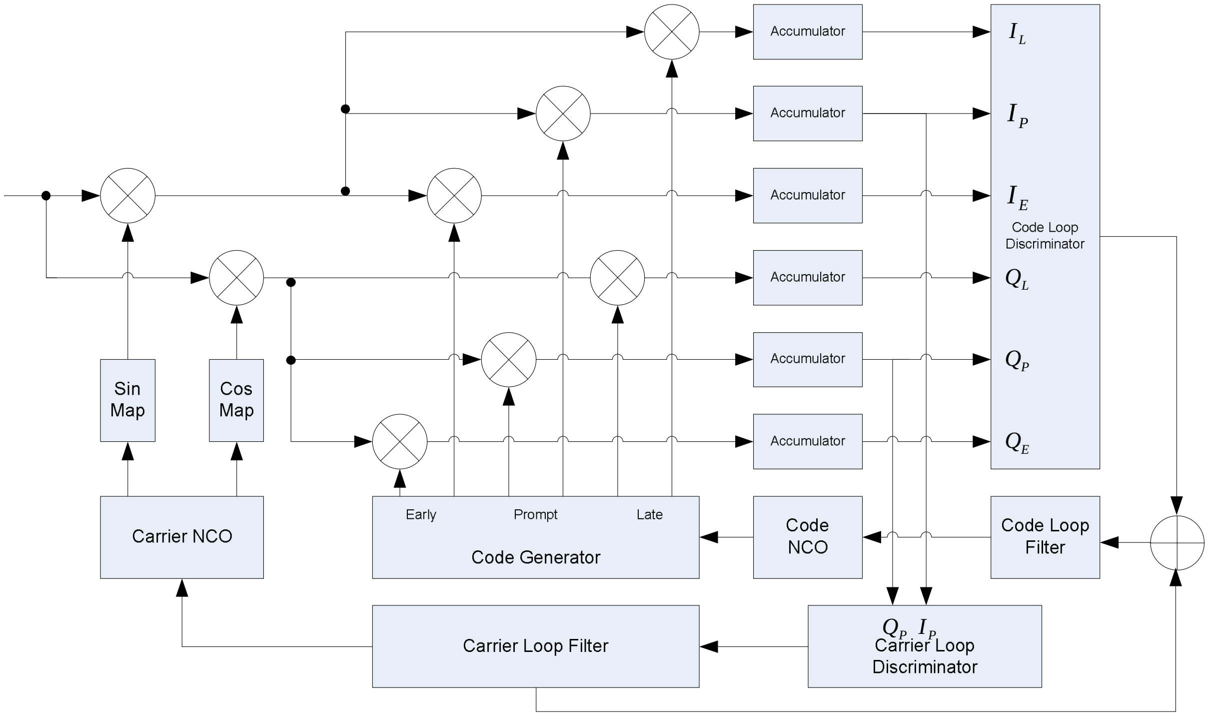

Figure 2-2: Receiver tracking loops [*Hannah, 2001*]

The input is digital IF, and the carrier is stripped or wiped-off by mixing with a replica carrier (plus carrier Doppler, to account for relative receiver dynamics). The outputs are In-Phase (I) and Quadrature-Phase (Q) samples. This signal is then despread by code stripping using Early (E), Late (L) and Prompt (P) correlators and processed by some form of discriminator. The code and carrier loops are controlled by Numerically Controlled Oscillators (NCO). The early/late correlators provide the input to the code discriminator which is implemented by one of several different early minus late forms.

The early minus late discrimination of these correlators produces a discrimination characteristic (tracking error) that controls the closed loop operation of the DLL. Some common DLL discrimination algorithms [*Ward, 1996*] are given in Table 2-1.

DLL Discriminator Algorithm	Description
$\sum(I_E - I_L)I_P + \sum(Q_E - Q_L)Q_P$	Dot Product Power – noncoherent
$\sum\left(I_E^2 - Q_E^2\right) - \sum\left(I_L^2 - Q_L^2\right)$	Early-Late Power – noncoherent
$\sum\sqrt{\left(I_E^2 - Q_E^2\right)} - \sum\sqrt{\left(I_L^2 - Q_L^2\right)}$	Early-Late Envelope – noncoherent
$\dfrac{\sum\sqrt{\left(I_E^2 - Q_E^2\right)} - \sum\sqrt{\left(I_L^2 - Q_L^2\right)}}{\sum\sqrt{\left(I_E^2 - Q_E^2\right)} + \sum\sqrt{\left(I_L^2 - Q_L^2\right)}}$	Normalised Early-Late Envelope – noncoherent
$\sum \mathrm{sign}(I_P)(I_E - I_L)$	Early-Late – coherent

Table 2-1: DLL discriminator algorithms [*Ward, 1996*]

Note that for every code loop discriminator, the power or the envelope values may be summed to reduce the iteration rate of the code loop filter as compared to that of the carrier loop filter when the code loop is aided by the carrier loop [*Ward, 1996*].

Each consecutive noncoherent algorithm increases in computational load, with the dot-product having the lowest, and the normalised envelope the highest. The coherent algorithm is included here but its performance is marginal at low SNR and is obviously unusable when carrier tracking is not possible. The noncoherent DLL implementations are the most robust.

The discriminator output is the relative tracking error of the DLL and is filtered and applied to the code NCO which in turn provides the necessary adjustment to the code generator phase for correct code-phase alignment of the replica and received codes.

For the carrier tracking loop there are, again, several implementations that may be used. If the receiver does not need to demodulate the navigation message (pure phase tracking for data less signals) then a pure PLL implementation can be used. Since however, most receivers will need to demodulate this data, a different PLL (Costas PLL) is often used. Other implementations may make use of FLLs. The FLL achieves carrier wipe-off by replicating the approximate frequency of the carrier.

The common algorithms [*Ward, 1996*], for the pure PLL and Costas PLL implementations, are presented in Table 2-2.

The performance of these discriminator algorithms is different under variable SNR conditions. The decision-directed, generic, and tangent discriminator algorithms are identical for the pure PLL and Costas PLL implementations. The decision-directed algorithm is near optimal for high SNR and has the least computational burden. The generic algorithm is near optimal at low SNR with moderate computational burden, while the tangent algorithm is suboptimal, but performs reasonable well at high and low SNR, with high computational burden. In addition, the tangent algorithm must check for divide by zero errors near ± 90 degrees. The final algorithm—arctangent— is an optimal Maximum Likelihood (ML) estimator at high and low SNR. In the pure PLL implementation it is a four-quadrant arctangent, while for the Costas PLL, it is two-quadrant.

PLL Discriminator Algorithm	Description
$\operatorname{sign}\left(I_p\right)Q_P$	Decision-Directed PLL (Costas)
$I_p Q_P$	Generic PLL (Costas)
$\dfrac{Q_P}{I_P}$	Tangent PLL (Costas)
$\tan^{-1}\left(\dfrac{Q_P}{I_P}\right)$	Arctangent – two-quadrant (Costas)/four-quadrant (pure PLL)

Table 2-2: PLL discriminator algorithms [*Ward, 1996*]

3 Experimental Validation

For demonstrating and validating diffraction phenomena originating on conducting aircraft surfaces during APL signal propagation, an aluminium cylinder test bed has been developed.

3.1 Test Bed Design

The test bed is realised as follows [*Biberger et al., 2001*]:

An aluminium cylinder (diameter...82 cm, height...80 cm, wall thickness...0.65 mm) with a NovAtel 511 antenna is mounted on a precision turntable. The cylinder is horizontally aligned through levelling. Figure 3-1 shows the configuration.

Figure 3-1: Aluminium cylinder on a precision turntable

An IntegriNautics IN500 APL (see Figure 3-2) with a NovAtel 501 antenna with choke ring (see Figure 3-3) transmits a L1 P-code signal (PRN 34) synchronised to the corresponding signals from the GPS satellite constellation. The NovAtel 501 antenna with choke ring is also used as a receiving antenna for the necessary reference station.

Figure 3-2: IntegriNautics IN500 APL and notebook with control software

Figure 3-3: NovAtel 501 antenna with choke ring for APL signal transmitting

The APL signal is pulsed according to the RTCA recommended APL signal specification (see appendix 8.3). Modified NovAtel OEM3 Propak II L1 navigation receivers (see Figure 3-4) are used for tracking the APL signal and the GPS satellites. These receivers operate with a special software version that was procured from GPS Silicon Valley (GSV).

Figure 3-4: Modified NovAtel OEM3 Propak II L1 navigation receivers

To avoid pseudorange bias errors in the receiver, the APL transmit power is adjusted with the IN500 control software such that the APL received peak power level (measured with a spectrum analyser) stays below -80 dBm [*Van Dierendonck, 1998*] during the experiment. Van Dierendonck demonstrated that for a received peak power level below -80 dBm there are no P-code pseudorange shifts. Because the carrier-phase is much less affected by the bias effect than the P-code [*Kiran and Bartone, 2004*], precise carrier-phase measurements are assured for the experimental validation.

Figure 3-5 shows the experimental arrangement of the cylinder (CYL), APL transmitter (APL) and reference station (REF) on the campus of the University Federal Armed Forces Munich.

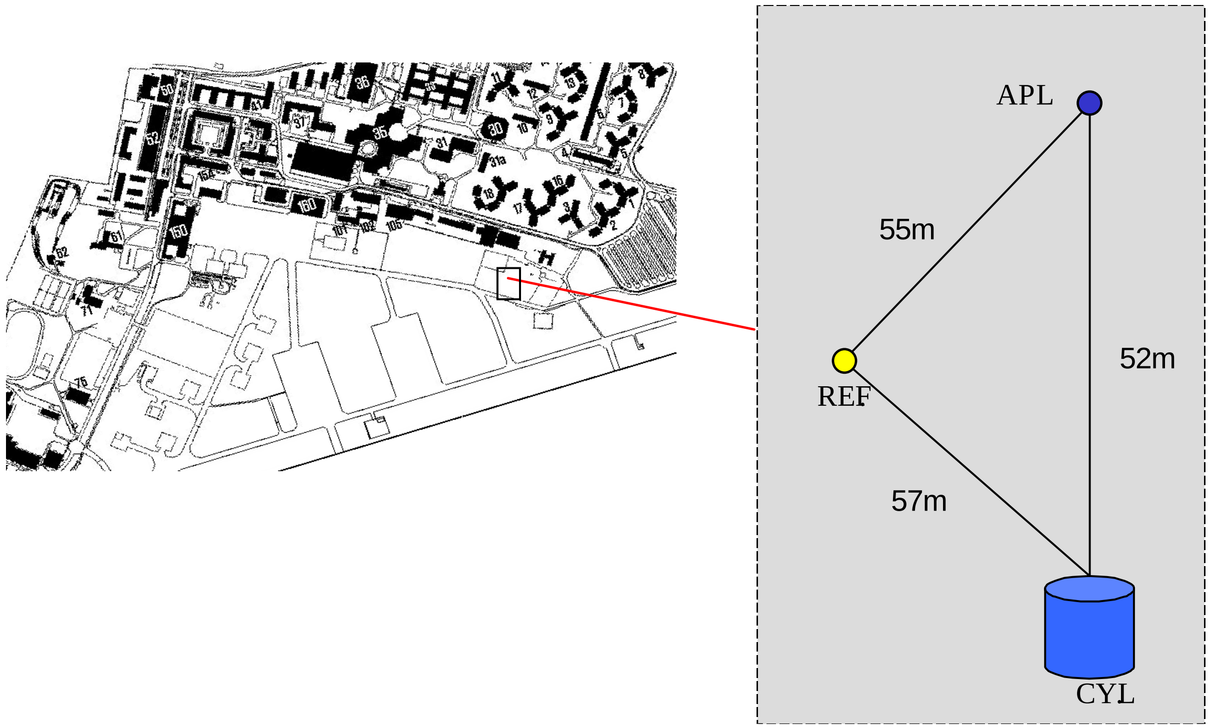

Figure 3-5: Experimental arrangement

Because of the precision turntable, the cylinder can be rotated over 360°. For the experimental verification it will be turned from 0° to 180° in steps of ten degree. A rotation angle of 0° means that the cylinder antenna is directly headed to the APL transmitting antenna and a rotation angle of 180° means that the cylinder antenna is headed away from the APL transmitting antenna. The signal power represented by the carrier power to noise power spectral density ratio (C/N_0) and the carrier-phase of the pulsed APL signal are measured on the cylinder surface as well as at the reference antenna with the NovAtel navigation receivers. Both receivers track also GPS satellite signals. Thus, relative distance measurements between the phase centres of the APL transmitting antenna and the cylinder antenna can be realised by forming carrier-phase double-differences between the cylinder and the reference station measurements.

3.2 Signal Power Measurements

Figure 3-6 shows the C/N_0 over the GPS system time depending on the rotation angle of the aluminium cylinder. The observations are logged for duration of approximately 10 minutes for each 10° step of the rotation angle. Up to a rotation of the cylinder of 90° the C/N_0 decreases slightly because of the antenna radiation pattern. After a rotation of 90° the C/N_0 decreases obvious stronger because the cylinder antenna moves into the shadow region of the cylinder. The C/N_0 increases again after a rotation of 160° up to a maximum rotation of 180° which is not expected because the cylinder antenna reaches maximum shadowing by the aluminium cylinder at 180° rotation angle.

The signal power measurements show that tracking of the APL signal without direct line-of-sight is possible on conducting surfaces. Further, the C/N_0 minimum at a rotation angle of about 160° (and not at 180°) indicates interference of the APL signal with itself and possible multipath.

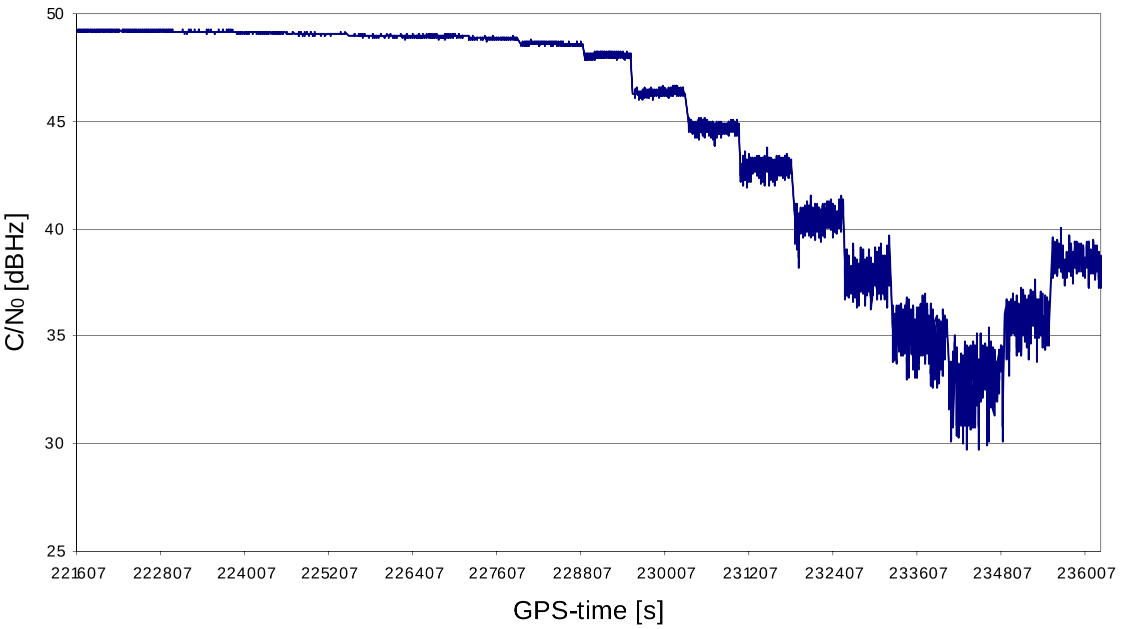

Figure 3-6: Carrier power to noise power spectral density ratio over GPS time

3.3 Relative Distance Measurements

By forming carrier-phase double-differences [*Cosentino and Diggle, 1996*] between the cylinder and the reference station measurements as follows

$$DD_{CYL-REF}^{GPS-APL} = \left(\phi_{CYL}^{GPS} - \phi_{REF}^{GPS}\right) - \left(\phi_{CYL}^{APL} - \phi_{REF}^{APL}\right), \tag{3-1}$$

relative distance measurements can be realised. ϕ_{CYL}^{GPS} and ϕ_{REF}^{GPS} are the measured carrier-phase residuals of the cylinder and reference antenna to the reference satellite. These residuals are calculated by subtracting the shift in carrier-phase because of the movement of the reference satellite. Respectively, ϕ_{CYL}^{APL} and ϕ_{REF}^{APL} are the carrier-phase measurements of the cylinder and reference antenna to the APL. Figure 3-7 illustrates the relative distance measurements (*) and the real geometric distance changes (o) (including the path around the cylinder) between the phase centres of the APL transmitting antenna and the cylinder antenna depending on the rotation angle. Because the exact phase centre of the combination aluminium cylinder plus NovAtel 511 antenna is unknown, the phase centre of a NovAtel 501 antenna plus chokering [*Larrimore, 2005*] is taken as a rough guess. Therefore, the distance between the centre of the aluminium cylinder and the phase centre of the cylinder antenna is the radius of the cylinder plus 9.7 cm [*Larrimore, 2005*] for the new phase centre of the cylinder antenna. Due to cycle slips in the navigation receiver, reliable carrier-phase measurements could only be realised up to a rotation angle of 140°.

The two curves in Figure 3-7 are very similar and we can conclude that the APL signal propagates along the curved metallic surface of the cylinder. After a rotation of the cylinder of 140°, the weak signal of the APL (because of shadowing effects and interference) causes cycle slips in the navigation receiver. Furthermore, multipath effects resulting from the APL signal from the reverse side of the cylinder might be also a reason for cycle slips in the navigation receiver [*Bauer*, *1997*].

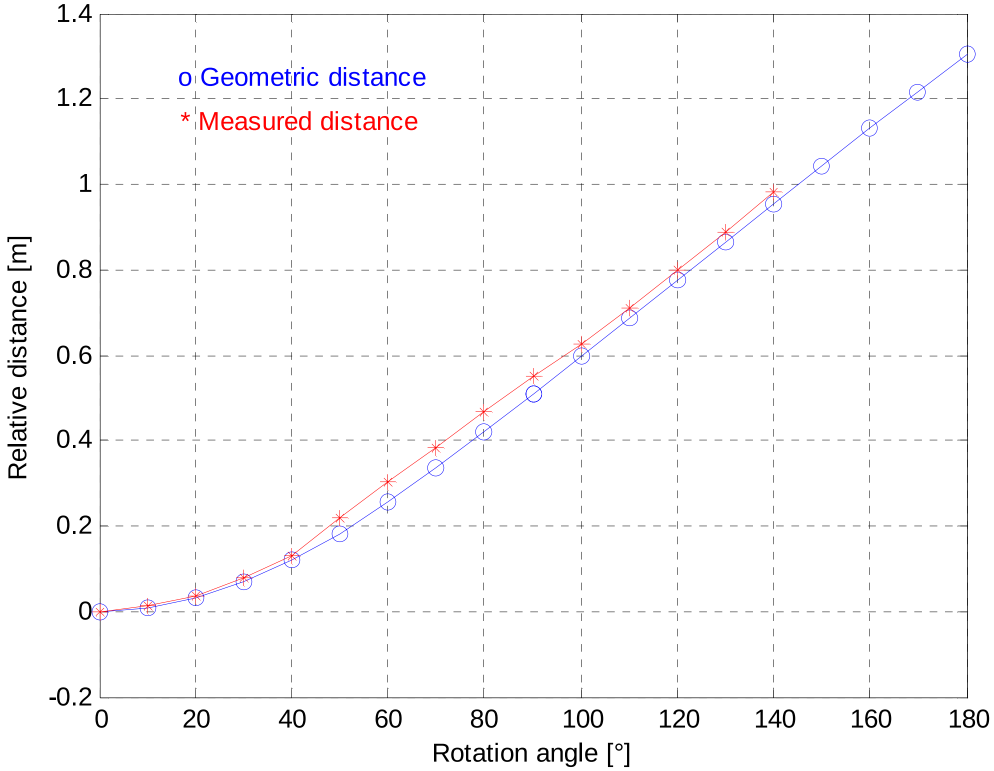

Figure 3-7: Relative distance measurements

4 Numerical Error Modelling

4.1 Numerical Field Theory

Computational techniques have revolutionised the way in which electromagnetic problems are analysed. Electrical engineers rely on efficient and accurate computer models to analyse and evaluate electromagnetic behaviour of antennas, propagation, scattering and component designs.

Although, most electromagnetic problems ultimately involve solving only one or two partial differential equations subject to boundary constraints, very few practical problems can be solved without computer-based methods [*Hannah, 2001*]. Computational electromagnetics involves the development of numerical algorithms for the solution of Maxwell's equations, and their subsequent use in analysing electromagnetic problems. Whereby, analytical techniques make simplifying assumptions about the geometry of the problem in order to apply a closed-form solution, numerical techniques attempt to solve the fundamental field equations directly, subject to the boundary constraints posed by the geometry. In the appendix 8.1 detailed descriptions of the fundamental field equations and representations of the electromagnetic field are given. A full treatment of general time-dependent fields and electromagnetic waves which will be required in later developments can also be found there.

Numerical techniques generally require more computation than analytical techniques but they are very powerful electromagnetic analysis tools. Without making a priori assumptions about which field interactions are most significant, numerical techniques analyse the entire geometry, and calculate the solution based on a full-wave analysis. A number of different numerical methods for solving electromagnetic problems are available. In essence, all the methods can be divided into two classes: semi-analytical methods and discretisation methods [*van Rienen, 2001*].

The best known semi-analytical methods are the mode matching technique, the method of integral equations, and the method of moments. In the method of integral equations, the given boundary value problem is transformed via appropriate Greens' function into an integral equation. In the method of moments which includes the mode matching technique as a special case, the solution function is expressed as a linear combination of adequate basis functions. The treatment of complex geometrical structures is very difficult for these methods and often requires geometrical simplifications: in the method of integral equations, the Greens' function has to satisfy the boundary conditions. In the mode matching technique, there must be a decomposition of the domain into subdomains such that the problem can be solved analytically in these subdomains and thus the basis functions can be given.

The best known discretisation methods are the Finite Element (FE) and the Finite Difference (FD) methods. These methods are applied to Poisson's equation, wave equation, or Helmholtz equation to compute the field numerically. The finite difference method is used for the basic equation (e.g. Poisson's equation). Choosing a difference method, one replaces all derivatives in the differential equations by some difference quotient. But this method has difficulties in the treatment of non rectangular domains and the treatment of such domains is more complex. Furthermore, the decomposition into subdomains which is undertaken in order to treat problems with piecewise homogeneous material filling results in a complicated coupling of the equations at the interfaces. The finite element method approximates the solution by some function in a finite dimensional space. Polynomials with local support are used as basis for this function space. A variational problem is solved instead of the basic differential equation.

A method which is especially well suited for the problems of field theory is the Finite Integration Technique (FIT) which is described in the appendix 8.2. In the case of Cartesian Grids, the FIT formulation can be rewritten in time domain to yield standard FD methods. However, whereas classical FD methods are limited to staircase approximations of complex boundaries, the FIT algorithm maintains the high simulation speed of the FD methods, while allowing an accurate modelling of curved structures, as in the FE methods.

4.2 Simulation of the APL Signal Propagation

The propagation of the navigation signal is based on a numerical solution of Maxwell's full set of equations considering material parameters. They are solved by using a commercially available general-purpose electromagnetic simulator (CST Microwave Studio) based on the Finite Integration Technique (FIT). This method (see appendix 8.2) provides a universal spatial discretisation scheme, applicable to various electromagnetic problems, ranging from static field calculations to high frequency applications in time or frequency domain [*CST, 2002*].

For an adequate analysis of diffraction phenomena on conducting aircraft surfaces, we analyse the navigation signal propagation effects by a very complete and complex simulation with CAD generated parts of aircraft bodies. Figure 4-1 shows an example of a box-shaped and a cylindrical fuselage part. The material parameters for the conducting surface (aluminium) [*Kuchling, 1991*] are:

$$\begin{aligned} \mu_r &= 1.0000208 \\ \kappa &= 3.7037037 \cdot 10^7 \quad [S/m] \\ \rho &= 2730 \qquad\qquad\quad [kg/m^3] \end{aligned}$$

μ_r is the relative permeability, κ is the electrical conductivity and ρ is the density of the material. The background material is air with relative permittivity $\varepsilon_r = 1.000594$ [*Kuchling, 1991*].

A plane electromagnetic wave is generated and propagates towards the navigation receiver's antenna which is located on the aircraft body. In the simulation we use a probe as an antenna which quantifies the Electric (E) field in one point. Figure 4-2 shows an example of a calculation domain with the orientation of the electromagnetic field vectors and the nose part of a cylindrical aircraft fuselage. For analysis reasons, the propagation direction of the electromagnetic field can be arbitrarily chosen.

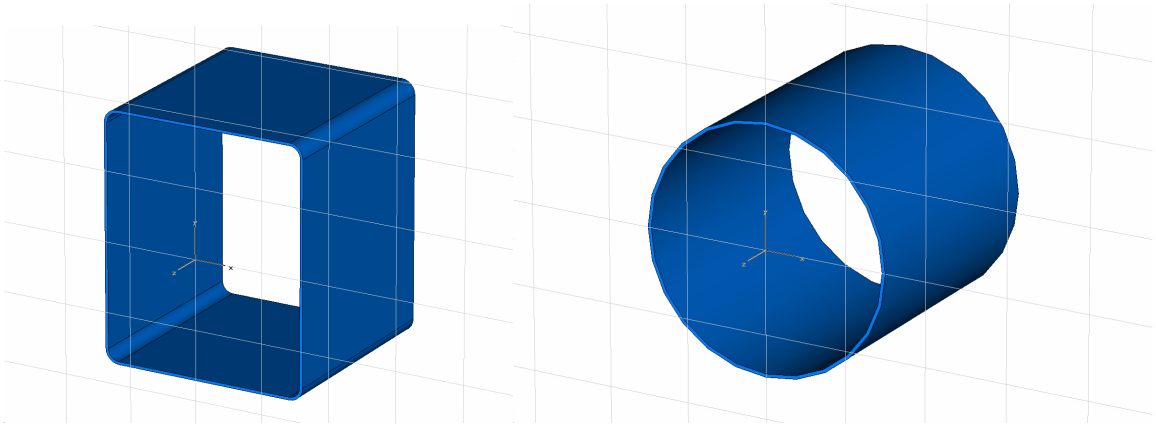

Figure 4-1: Box-shaped and cylindrical fuselage parts

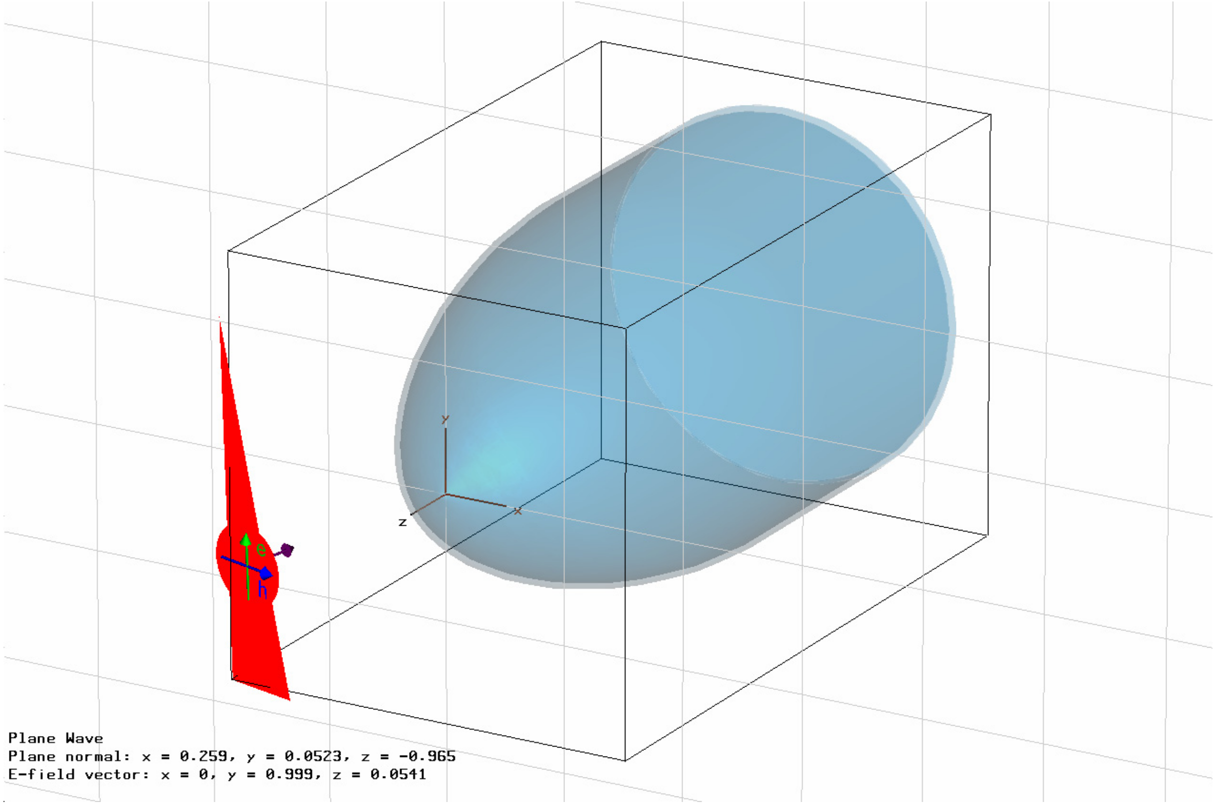

Figure 4-2: Orientation of the electromagnetic field vectors of a plane wave

The electromagnetic wave is vertically polarised and the emitted APL signal $s(t)$, the P-code on GPS L1 frequency (navigation data are not considered), can be described as [*Biberger et al., 2003*]

$$s(t) = \sum_{j=-\infty}^{\infty} A c_j p\left(t - jT_C\right). \tag{4-1}$$

Where one (+1) chip of a BPSK signal at RF level -*the single chip function at RF level*- of the emitted signal can be written as

$$p(t) = \begin{cases} \cos(2\pi f_{L1} t) & 0 \le t < T_C \\ 0 & \text{else} \end{cases} . \qquad (4\text{-}2)$$

For the carrier frequency f_{L1} we use 1575.42 MHz and for the chip length T_C we use $T_C = 1/f_C$ with a chipping rate f_C of 10.23 MHz. The time is denoted as t. It should be noted that a possible Doppler shift due to the motion of the receiver is of no importance to this investigation.

The emitted signal $s(t)$ is a convolution in the time domain of the code sequence c_j with the single chip function $p(t)$ at RF level. $p(t)$ represents the navigation signal at RF level during the period of one P-code chip. The amplitude of the signal $s(t)$ is A, but has no influence on the results. It is sufficient to consider only the single chip function $p(t)$ to calculate all propagation effects, even for the full navigation signal. Appendix 8.4 contains a detailed treatment of this assumption.

The advantage of the single chip function at RF level in comparison to the full APL signal is that the simulation needs to run only for a time of about a few chip periods (i.e. a processing time of approximately three days with a conventional PC). Figure 4-3 shows the signal $p(t)$ calculated with the electromagnetic simulator.

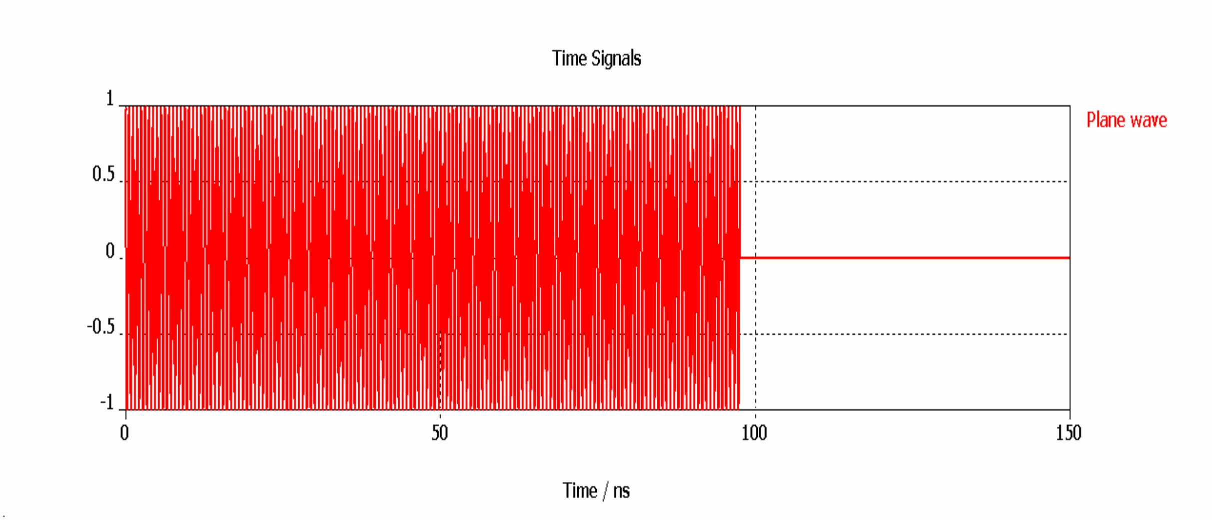

Figure 4-3: Electromagnetic wave modulated with a P-code chip

Bandpass filtering of the signal $s(t)$ to keep the power spectral density within the allocated frequency band is not included in equation (4-1). However, it will be included in the navigation receiver frontend which is described in the next chapter.

Figure 4-4 shows the single chip navigation signal $p(t)$ received by a top-mounted aircraft antenna on a box-shaped fuselage part with a width of 1.5 m and a height of 1.9 m and Figure 4-5 shows the electric field around the airframe. Both figures are results of the electromagnetic simulator. In this example we choose for the elevation β (see Figure 5-8 in chapter 5.2.1) of the aircraft 20°. The angle α (see Figure 5-9 in chapter 5.2.1) between the propagation direction of the emitted APL signal $s(t)$ and the horizontal projection of the longitudinal axis of the fuselage is 250°. The pitch angle θ and the bank angle φ of the aircraft body are both 0°. The amplitude of the received signal (see Figure 4-4) is about half of the amplitude of the transmitted signal, because of diffraction losses and the signal has a delay as we expect. We see little signal interferences in the front part of the chip and some spikes at the end. On the left side of Figure 4-5 we can see a typical interference pattern coming from interference of the incoming signal *s*(*t*) and a reflected signal from the aircraft body. The right side of Figure 4-5 shows the diffracted signal.

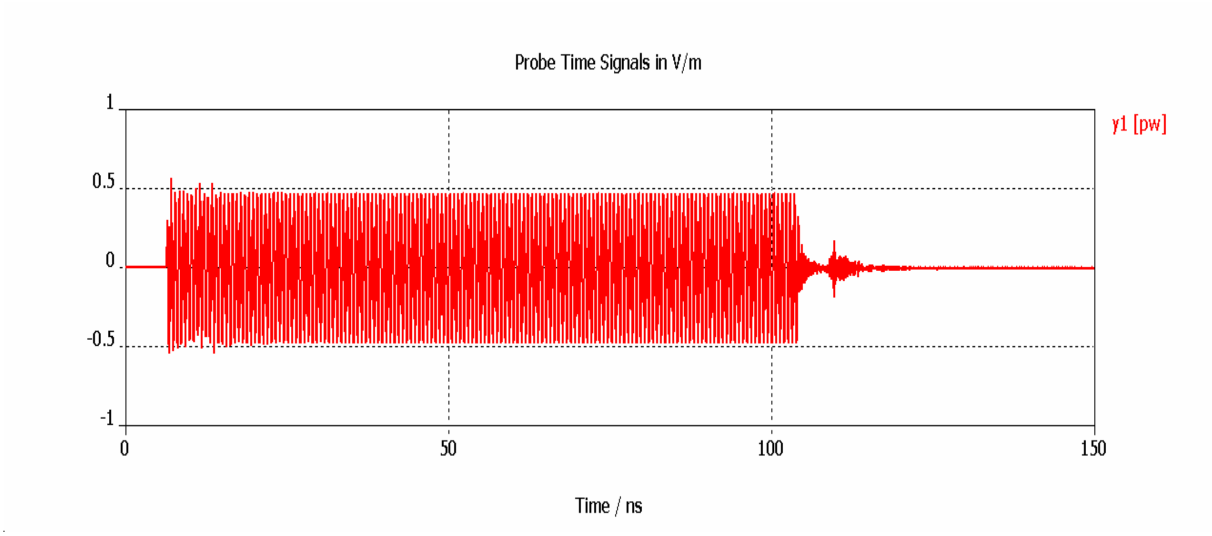

Figure 4-4: Received P-code chip calculated with the electromagnetic simulator

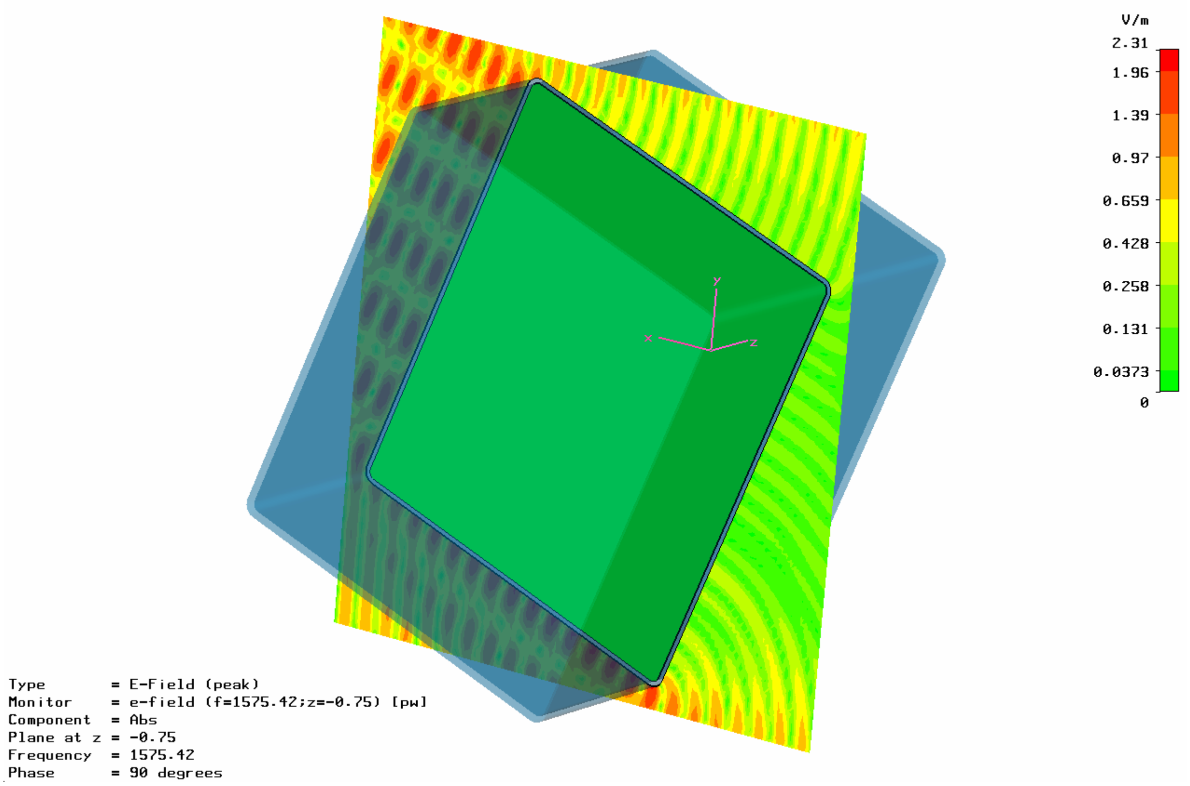

```
Type        = E-Field (peak)
Monitor     = e-field (f=1575.42;z=-0.75) [pw]
Component   = Abs
Plane at z  = -0.75
Frequency   = 1575.42
Phase       = 90 degrees
```

Figure 4-5: Electric field of the APL signal around a box-shaped airframe

In order to determine the effect on navigation performance, we analyse the received signal using a GPS/APL receiver simulation in the next chapter.

4.3 GPS/APL Receiver Signal Processing

The received signal is analysed in two steps. In the first step, the signal is passed through a frontend simulation to downconvert it from RF level to an intermediate frequency of 0 MHz or equivalently to baseband. In the second step, code and phase delay of the signal are determined by analysis of the signal's correlation function with the reference signal.

To determine receiver hardware delays coming from band- and lowpass filters, we run the propagation simulation two times. In the first case, the aircraft body is absent (see Figure 4-6) and this case is used to determine the geometric distance between emitter and receiver plus the hardware delays. A second run includes the aircraft body (see Figure 4-7) causing a further delay of the signal. The first case is referred to as empty case, the second one as body case.

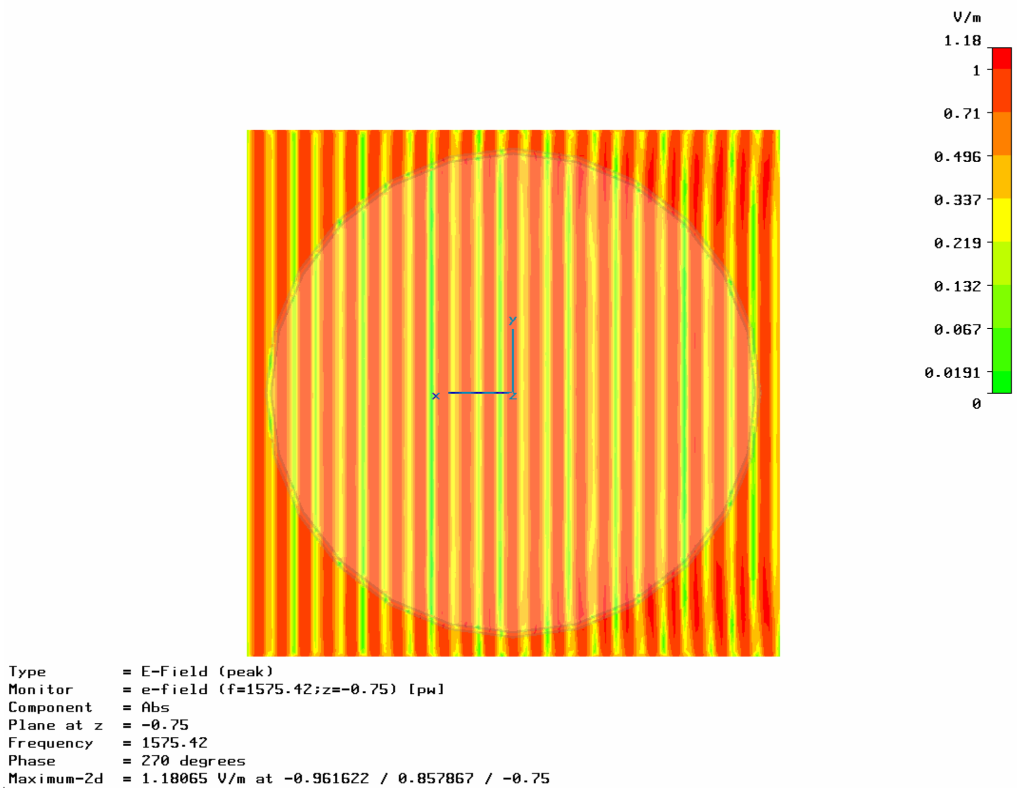

```
Type         = E-Field (peak)
Monitor      = e-field (f=1575.42;z=-0.75) [pw]
Component    = Abs
Plane at z   = -0.75
Frequency    = 1575.42
Phase        = 270 degrees
Maximum-2d   = 1.18065 V/m at -0.961622 / 0.857867 / -0.75
```

Figure 4-6: APL signal propagation simulation with aircraft body absent

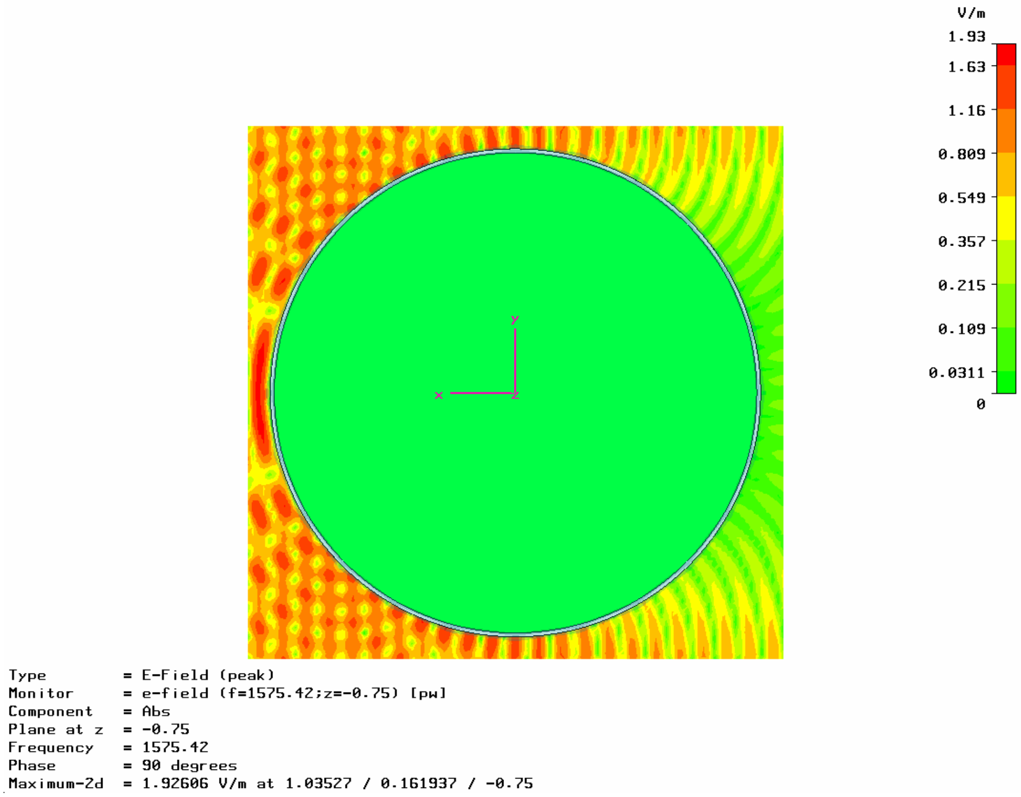

```
Type          = E-Field (peak)
Monitor       = e-field (f=1575.42;z=-0.75) [pw]
Component     = Abs
Plane at z    = -0.75
Frequency     = 1575.42
Phase         = 90 degrees
Maximum-2d    = 1.92606 V/m at 1.03527 / 0.161937 / -0.75
```

Figure 4-7: APL signal propagation simulation with cylindrical aircraft body

4.3.1 Navigation Receiver Frontend

The received single chip (see Figure 4-4) is fed into a Matlab/Simulink simulation of a receiver frontend [*Biberger et al., 2003*]. The frontend converts the real-valued signal from f_{L1} to baseband and is shown in Figure 4-8.

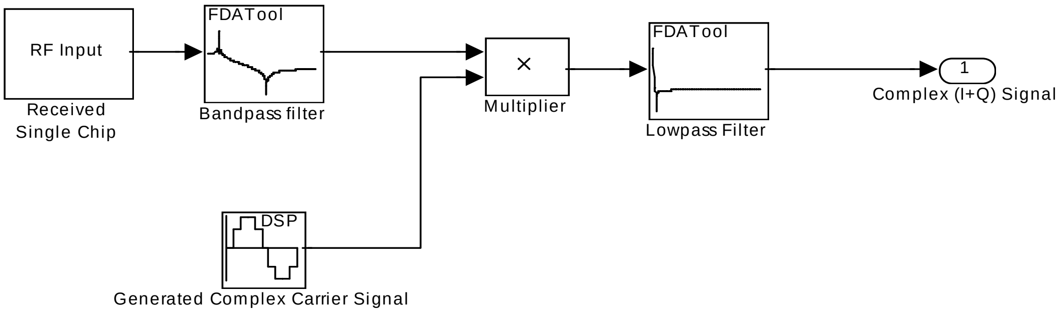

Figure 4-8: Matlab/Simulink simulation of the navigation receiver frontend

The simulation runs at a sample rate of 32 GHz and the highest frequency is two times the carrier frequency after multiplication. It is about 3 GHz.

The incoming signal is bandpass filtered by a Finite Impulse Response (FIR) filter (Hamming window) of order 1024 and is shown in Figure 4-9. The dual-sided filter bandwidth is 24

MHz and the centre frequency of the bandpass filter is at L1. At 1563.42 MHz and 1587.42 MHz the filter has an attenuation of 6 dB. The output of the bandpass filter for our example in chapter 4.2 is shown in Figure 4-10. In comparison to Figure 4-4, the bandlimited signal appears to be quite smooth, especially the spikes at the end of the pulse disappeared. From this we conclude that those spikes are numerical artefacts, not representing physical effects.

The bandpass filtered signal is multiplied by the complex nominal carrier signal with the frequency f_{L1}. The complex carrier signal of the receiver is generated as

$$\exp(i2\pi f_{L1}t)\,. \tag{4-3}$$

The real part is used for down converting the I-channel, the imaginary part for the Q-channel. The output of the multiplier is lowpass filtered and the resulting complex signal p_{REC}, i.e. the single chip function at baseband, is stored for further processing. The lowpass filter eliminates the unwanted frequencies at the doubled carrier frequency. Again, a FIR filter of order 1024 is used (Hamming window) and is shown in Figure 4-11. At 80 MHz the low-pass filter has an attenuation of 6 dB.

Both the bandpass filter and the lowpass filter have a constant group delay of 512 samples within the passband region.

The real part (dotted line) and imaginary part (solid line) of the single chip function at baseband for the empty (red line) and the body case (blue line) are shown in Figure 4-12.

It should be noted that from the single chip function output of the frontend the entire received navigation signal at baseband can be reconstructed by convoluting it with the code sequence (see appendix 8.4).

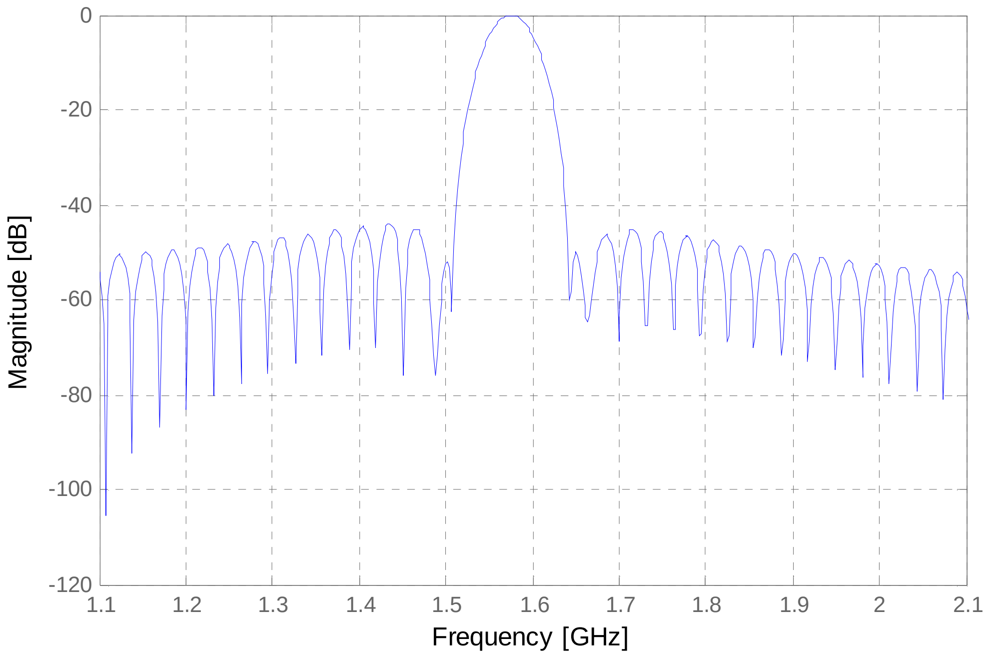

Figure 4-9: Magnitude response of the bandpass filter

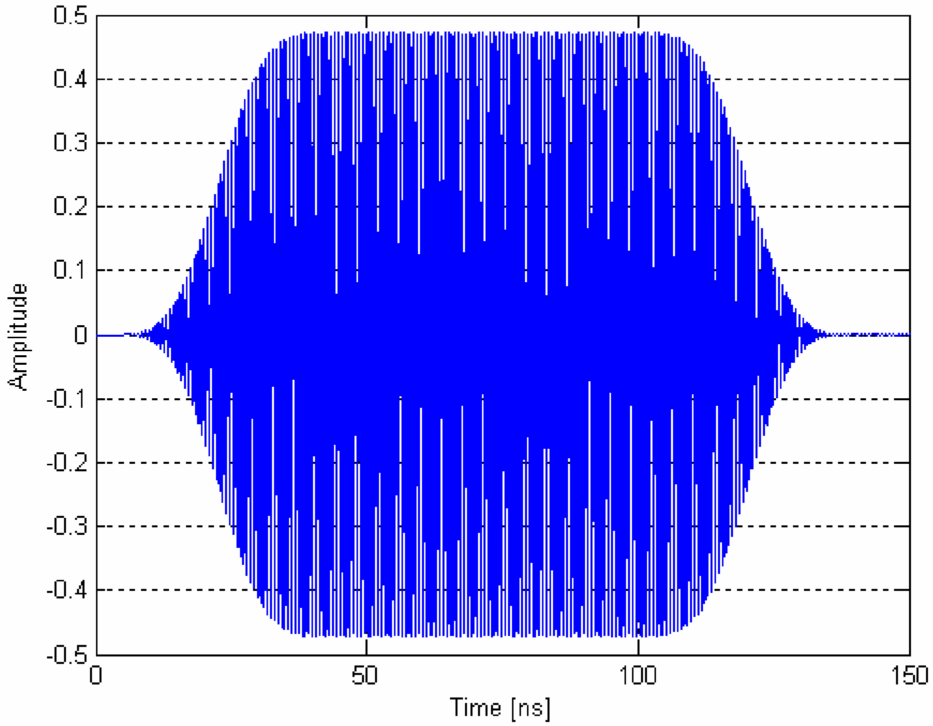

Figure 4-10: Single chip function at RF level after bandpass filtering

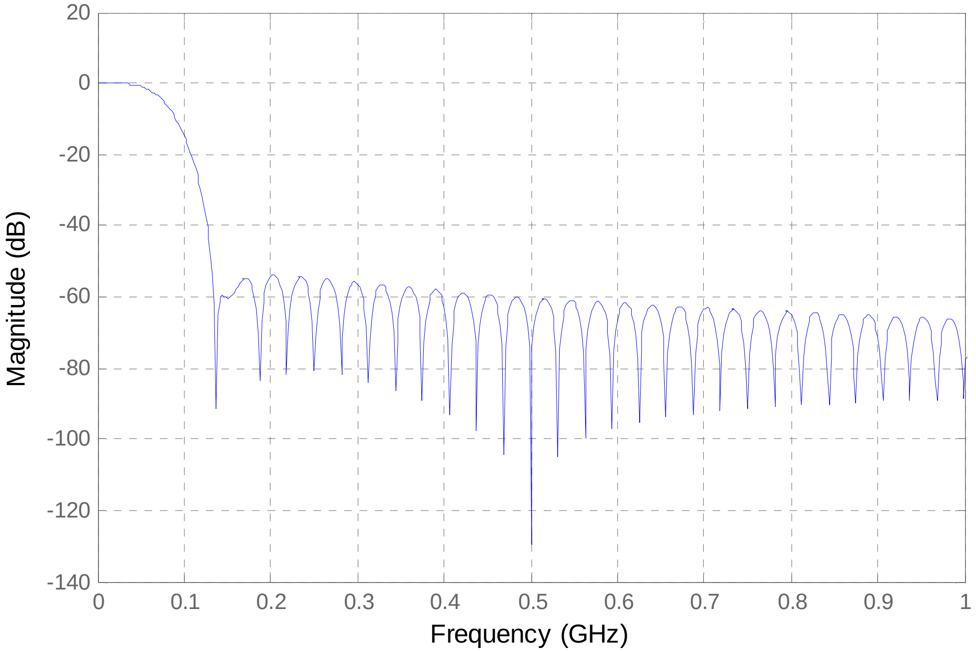

Figure 4-11: Magnitude response of the lowpass filter

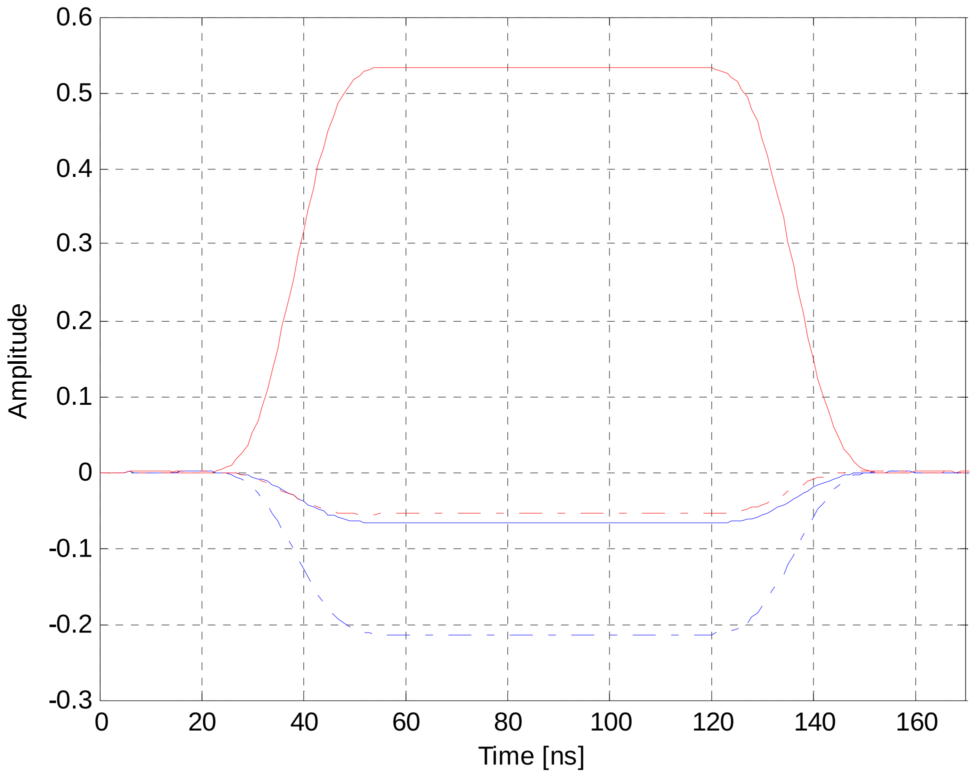

Figure 4-12: Single chip function at baseband

4.3.2 Code Tracking

We determine the code delay by evaluating the correlation function

$$R(\phi)=\int_{\phi'=0}^{T} p_{REC}(\phi')p_{REP}(\phi'+\phi)d\phi' \tag{4-4}$$

between the received single chip function p_{REC} (depending on the code-phase ϕ' [chips]) at baseband and the internally generated replica chip function

$$p_{REP}(\phi')=\begin{cases}\cos\left(2\pi\phi' f_{L1}/f_C\right) & 0\le\phi'<1\\ 0 & \text{else}\end{cases}. \tag{4-5}$$

The position of the maximum of the (complex) correlation function R (depending on the chip offset ϕ [chips]) determines the estimated total delay. Since direct determination of the maximum is impractical within a real navigation receiver, the so-called S-function is formed by correlating the incoming signal with a slightly delayed and a slightly advanced replica of the code. The distance (in units of chips) of the early and late code replica is called correlator spacing d. If the output of both correlation processes is equal, the maximum of the correlation function is approximately found.

For this analysis, we consider an early power minus late power code discriminator [*Van Dierendonck, 1995*] and the corresponding S-function is given by

$$S(\phi) = \gamma\left(\left|R(\phi - d/2)\right|^2 - \left|R(\phi + d/2)\right|^2\right). \tag{4-6}$$

The value of the constant γ must be chosen such that $S(\phi)=\phi$ for small values of ϕ.

The code delay is obtained by calculating the zero crossing of the S-function. Its value for the empty case is the delay caused by the bandpass and lowpass filter (i.e. the receiver hardware delay) plus the straight line distance between emitter and receiver. This value has to be subtracted from the delay of the body case to obtain only the code delay due to the presence of the aircraft body.

For our example, shown in Figure 4-4, we obtain a code delay of 11.5109 m for the empty case and 11.5271 m for the body case. The difference of 1.62 cm can be attributed to a signal delay due to the increased geometric length of the signal propagation path around the aircraft body called Signal Path Extension (SPE).

In addition to the SPE, at least two other effects have to be considered when code delay values are computed. First, their numerical accuracy is on the order of a few centimetres (empirically determined after several computational runs) because determination of the S-function involves numerical integration and interpolation which cannot be done arbitrarily precisely.

The second code delay error source could be multiple propagation paths. Since the propagation simulation is based on Maxwell's equations an arbitrary (even infinite) number of propagation paths can occur. At the antenna all signals superimpose and the sum is processed by the receiver, respective analysed in our simulation. Although we cannot isolate the multipath errors, by looking at the correlation function we can tell if they are present.

The real part (dotted line) and imaginary part (solid line) of the correlation function $R(\phi)$ for the empty (red line) and the body case (blue line) are shown in Figure 4-13. Both cases are practically equal and only one line can be seen. Since the empty case is per definition multipath free, we conclude that also the body case contains no strong multipath. However, since multipath with low signal amplitude of the secondary signals or multipath with very small delay values can not be identified from a visual inspection of the correlation function, we show in Figure 4-14 the differences of the absolute values of the correlation functions between the empty and the body case

$$\Delta R(\phi) = \left|R_{empty}(\phi)\right| - \left|R_{body}(\phi)\right|. \tag{4-7}$$

The maximum of these differences can be used as an indicator for the amount of the distortion of the correlation function for the body case. In our example the differences nearly vanish indicating no significant multipath influence.

It is important to note that the point ϕ=0 is determined in both cases by the zero crossing of the S-function separately.

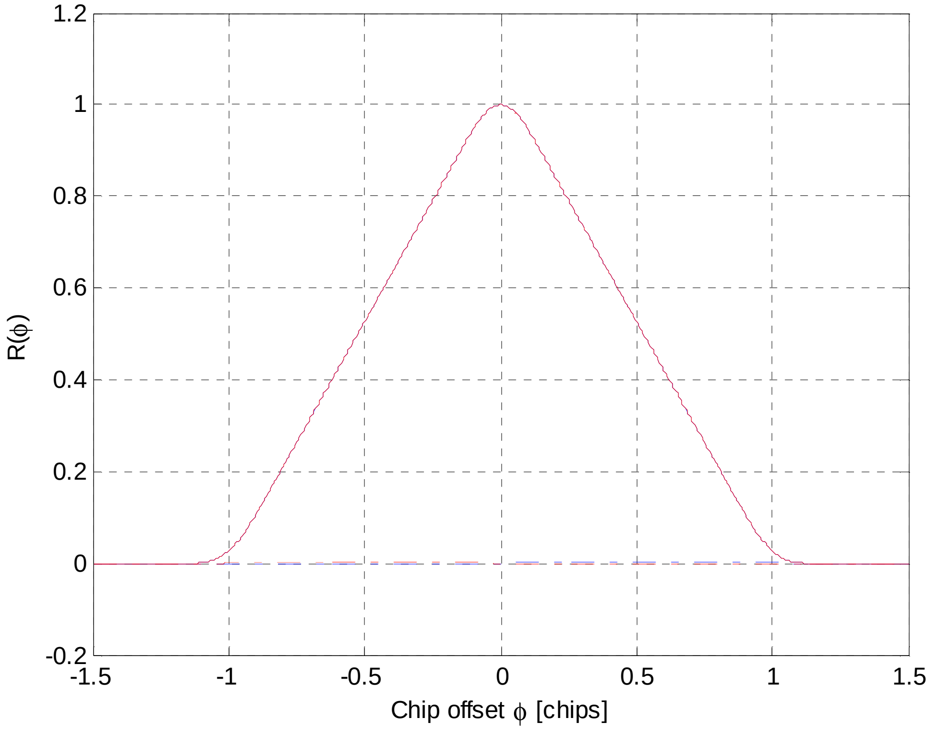

Figure 4-13: Correlation function *R*(*ϕ*)

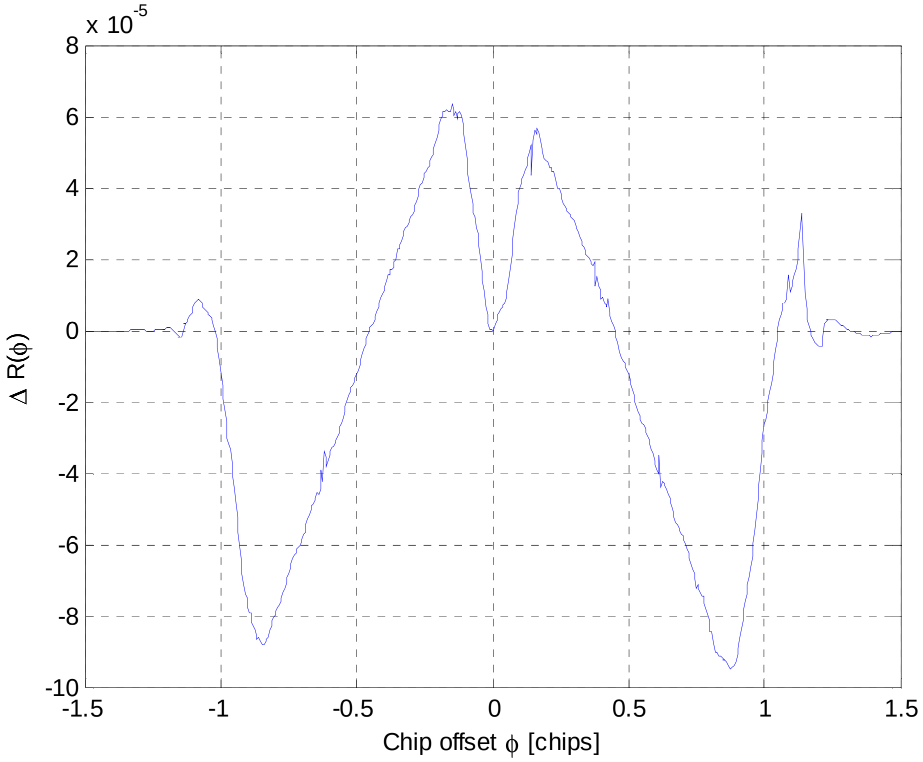

Figure 4-14: Difference of correlation functions between empty and body case

4.3.3 Carrier-Phase Tracking

The carrier-phase delay ϕ_{del} in [rad] is given by the phase angle of the complex correlation function $R(\phi)$ at the point where the S-function vanishes, i.e. $S(\phi)=0$:

$$\phi_{del} = \operatorname{atan2}\left(\frac{R_Q(\phi)}{R_I(\phi)}\right) \tag{4-8}$$

$$\begin{aligned} R_Q(\phi) &= \operatorname{Im}\left(R(\phi)\right) \\ R_I(\phi) &= \operatorname{Re}\left(R(\phi)\right) \end{aligned}. \tag{4-9}$$

Similar to the code delay, the carrier-phase delay contains the signal path extension and a possible error due to multipath.

For our example, shown in Figure 4-4, we obtain a carrier-phase delay value of 5.07 cm for the empty case and a carrier-phase delay value of 10.44 cm for the body case. The difference of 5.37 cm can be attributed to the SPE due to the presence of the aircraft body.

The accuracy of the carrier-phase delay determination with this technique is about a few millimetres due to numerical inaccuracies (empirically determined after several computational runs). This is much better than the accuracy of the code delay determination.

Carrier multipath, as another error source, is limited to a fourth of the carrier-phase wavelength, i.e. 4.76 cm [*Bauer*, *1997*]. This limit is reached for the unlikely case, if one multipath signal has the same amplitude as the direct signal. In general, significant attenuation occurs on the multiple propagation paths and carrier-phase multipath is much smaller.

Similar to the code multipath, we cannot separate the multipath contribution from the delay value. By inspection of the code correlation function we can tell if multipath is present. Note that code and carrier multipath appear always simultaneously.

4.4 Results

The previous described numerical simulation of the APL signal propagation will be applied to the aluminium cylinder described in chapter 3, an aircraft nose, a cylindrical and a box-shaped aircraft body. The sizes of these objects are chosen as large as it could be handled with a conventional Personal Computer (PC) with two gigabytes of memory because the quantitative results shall be close to the electromagnetic effects which can appear on real conducting aircraft surfaces. The calculated RF antenna data for different attitudes of the objects will be further processed and analysed with the APL receiver signal processing model. Particularly, the differences of the absolute values of the correlation functions between the empty and the body case are of interest in order to analyse the different aircraft parts with regard to multipath effects.

4.4.1 Aluminium Cylinder

A cylinder with the same dimensions like the real one in chapter 3 with material parameters for aluminium (see chapter 4.2) is generated with CAD (see Figure 4-15).

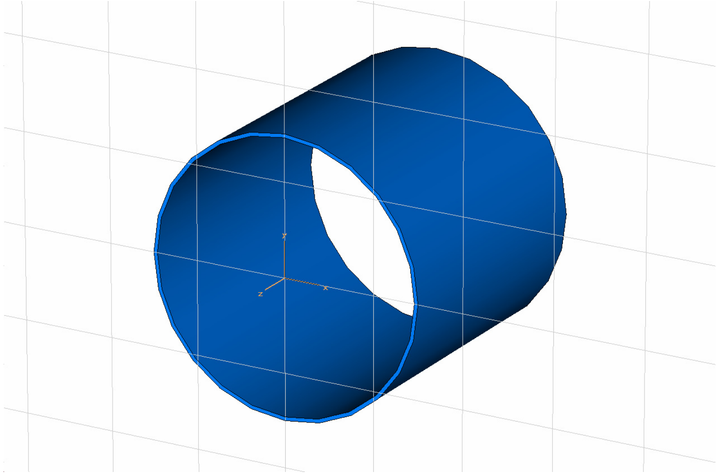

Figure 4-15: Aluminium cylinder generated with CAD

The numerical simulation calculates the relative change in carrier-phase and code delay (P-code) at the antenna (electrical field probe) because of the different rotation angles of the cylinder. This simulation results are compared to the real relative distance measurements of chapter 3.3. Figure 4-16 shows that the calculated relative code and carrier-phase delay approximately match with the relative distance measurements and calculated geometric distances for rotation angles up to 140°. After a rotation angle of about 140° the calculated code delay deviates more from the geometric distance indicating possible multipath influence. The phase delay shows a larger deviation from the geometric distance at a rotation angle of 180°.

With the possibility in our simulation to calculate the differences of the absolute values of the correlation functions between the empty and the body case, we can analyse the received signal with regard to multipath effects. The maxima of these differences are shown in Figure 4-17 depending on the rotation angle of the aluminium cylinder. For rotation angles of 150°, 170° and 180° we get increased values for the maxima explaining the code and phase delay deviations.

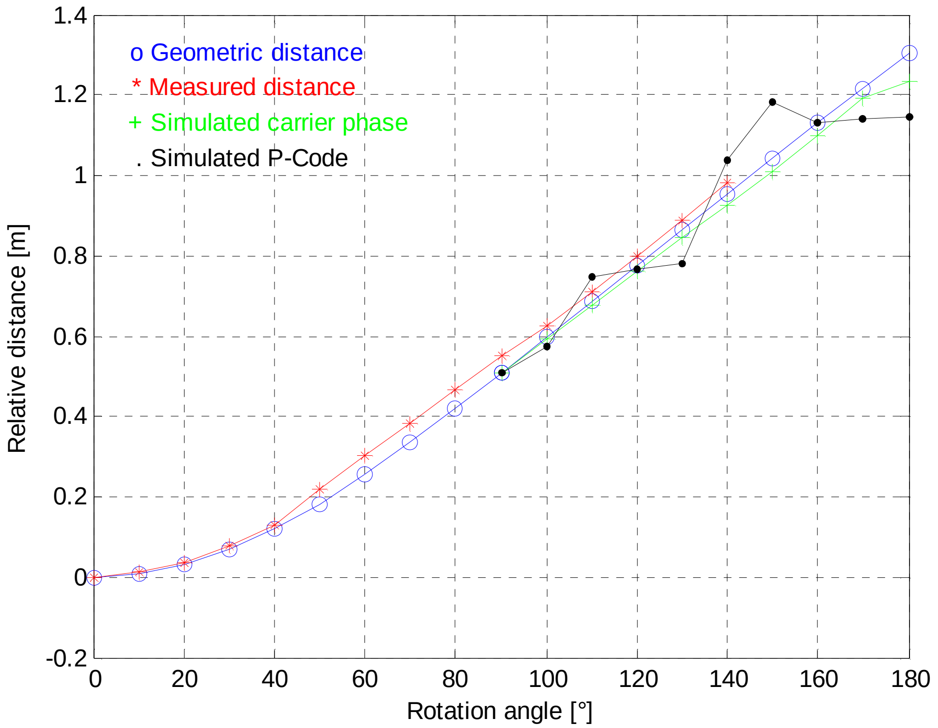

Figure 4-16: Comparison of simulated and real measurements (cylinder)

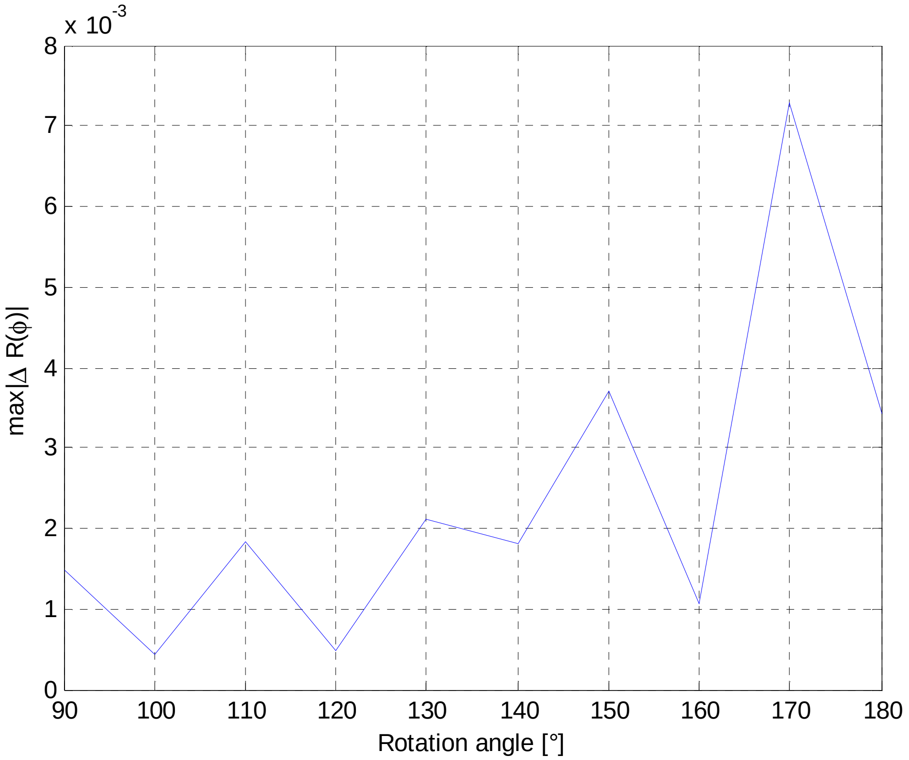

Figure 4-17: Maxima of differences of correlation functions (cylinder)

4.4.2 Aircraft Nose (Cylindrical Aircraft Body)

Figure 4-18 shows a simplified aircraft nose (CAD) consisting of a rounded front part and a cylindrical part (diameter…1.5 m) with material parameters for aluminium.

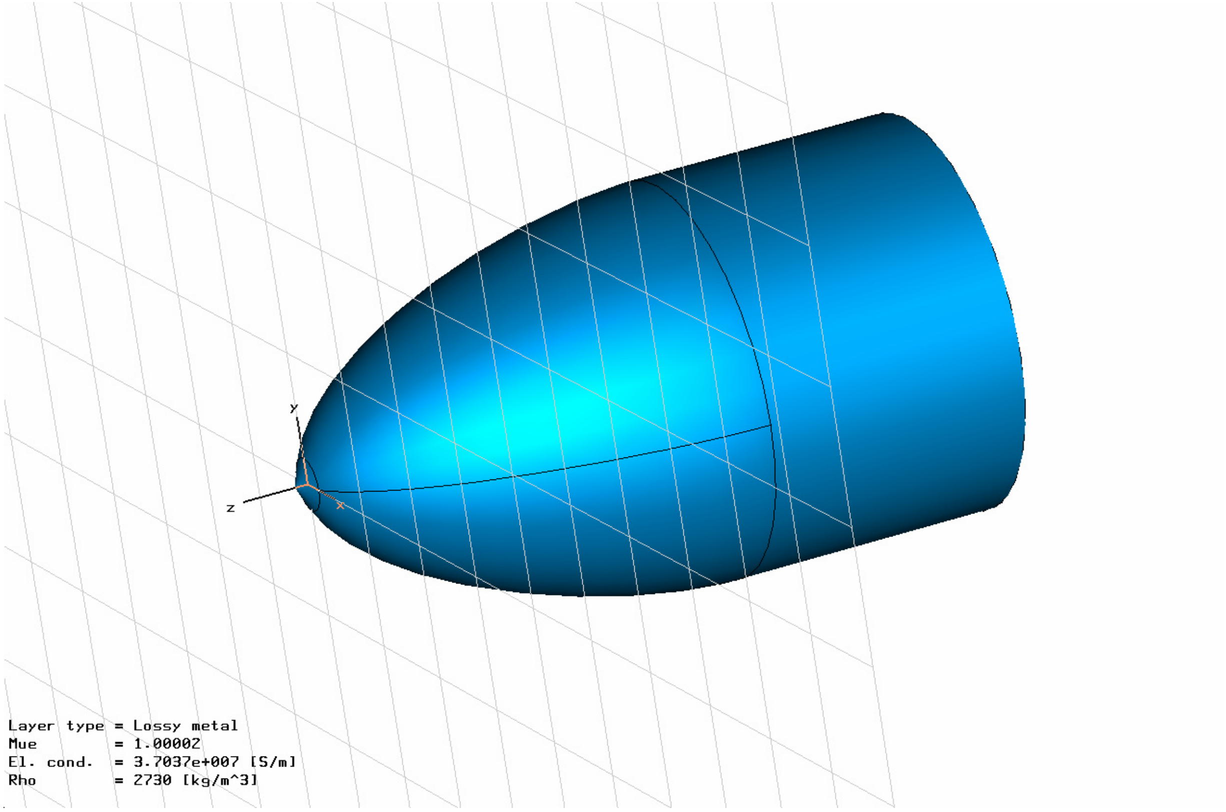

Figure 4-18: Aircraft nose (CAD) with material parameters (aluminium)

This conducting aircraft surface is analysed with regard to multipath effects by calculating the differences of the absolute values of the correlation functions between the empty and the body case for different bank angles φ (10°, 20°, 30°, and 40°) and small angles α (195°, 210°, and 225°). The elevation angle β is 3° and the pitch angle θ is 0°. The maxima of these differences are shown in Figure 4-19. Fortunately, these values remain below the multipath limit (see Figure 4-19) and are relatively small compared to the values for the aluminium cylinder at rotation angles of 150°, 170° and 180° indicating almost no multipath influence.

The multipath limit is defined as the largest calculated value for the maxima of differences of correlation functions up to a rotation angle of 140° for the aluminium cylinder in chapter 4.4.1. A rotation angle of 140° is chosen because feasible real phase measurements with the aluminium cylinder in chapter 3 were possible up to this angle.

The calculated additional signal delay due to the presence of the aircraft nose is shown in Figure 4-20 for different angles φ and α. The signal path extension remains relatively small (<6 cm) for bank angles φ up to 40°. A black curve in Figure 4-20 is representing the additional signal delay due to a geometric path over a cylinder with a diameter of 1.5 m. It can be seen that the SPE curves for the aircraft nose match more and more the black curve with increasing α. This means that the cylindrical part of the aircraft nose is more and more affecting the signal.

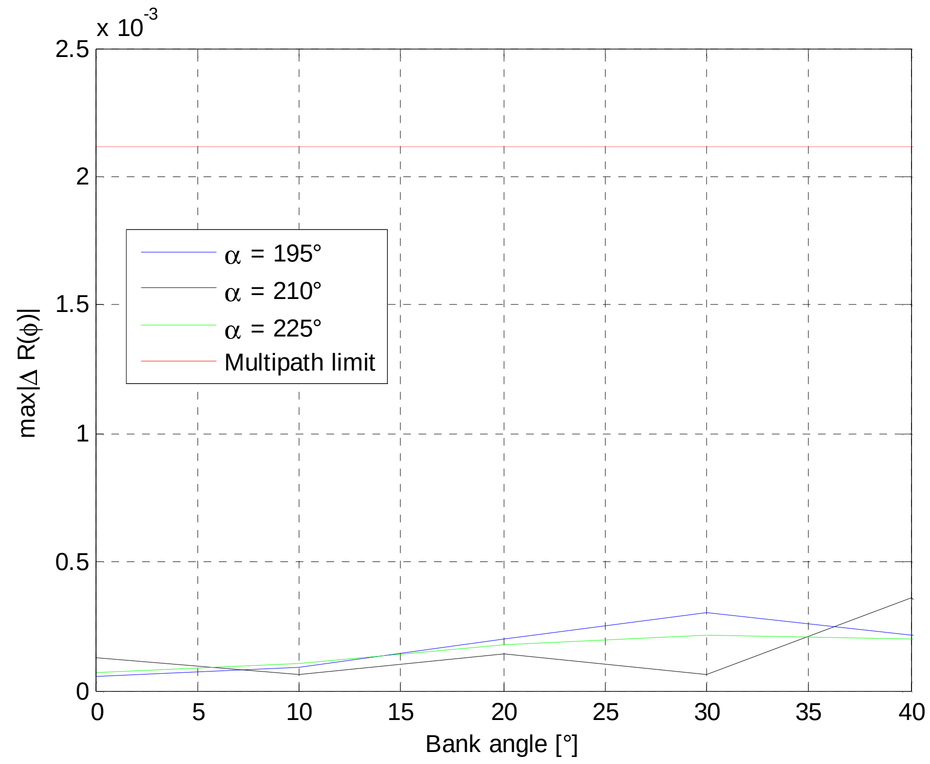

Figure 4-19: Maxima of differences of correlation functions (aircraft nose)

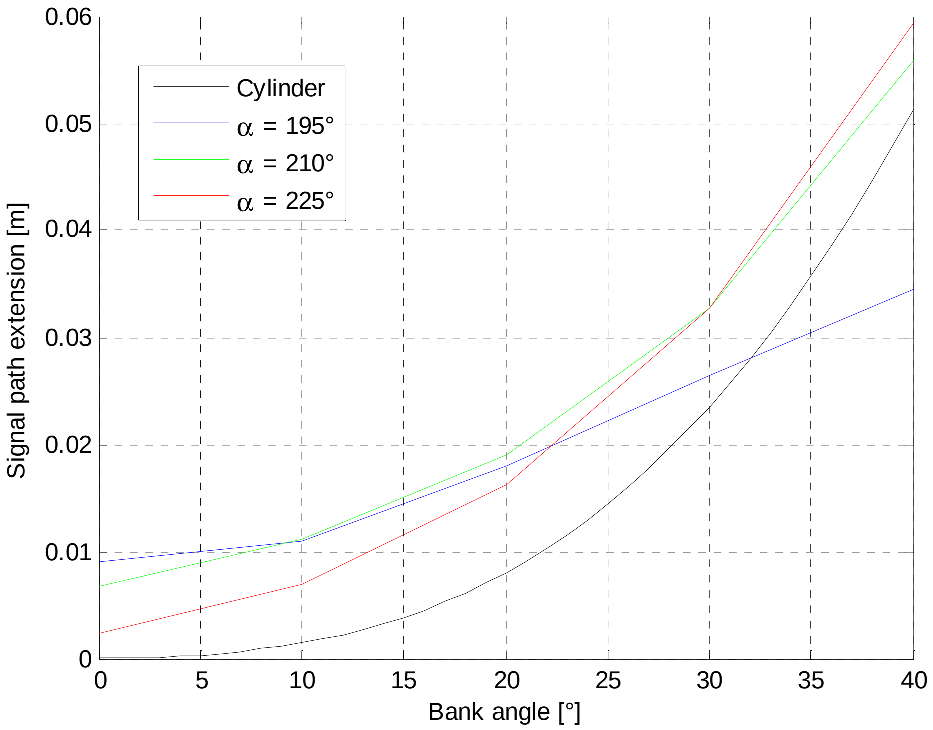

Figure 4-20: Signal path extension (aircraft nose)

4.4.3 Cylindrical and Box-Shaped Aircraft Body

For larger angles *α* we use aircraft parts like those illustrated in Figure 4-1 because the received APL signal is not affected by the aircraft nose. The diameter of the cylindrical aircraft body is 2 m and the width of the box-shaped aircraft body is 1.5 m. Again, the structures are analysed with regard to multipath effects by calculating the differences of the absolute values of the correlation functions between the empty and the body case for different elevation angles *β* (10°, 20°, 30°, and 40°) and large angles *α* (250°, 260°, and 270°). The pitch angle *θ* of the aircraft is in every case 0°. It should be noted that the angle *β* can be interpreted as a bank angle because the angle *α* is close or equal to 270°. The maxima of these differences are shown in Figure 4-21 and Figure 4-22. These values remain again below the multipath limit and are small compared to the values for the aluminium cylinder in chapter 4.4.1 at rotation angles of 150°, 170° and 180° indicating no significant multipath influence.

The calculated signal path extensions due to the presence of the aircraft bodies for different angles *β* and *α* are shown in chapter 5.2.2 (see Figure 5-14 and Figure 5-15). The SPE values remain small (<7 cm for the cylindrical aircraft body, <18 cm for the box-shaped aircraft body) for angles *β* up to 40°.

Note that there are no calculated values for the box shaped aircraft body with *α*=250° and *β*=40° because of the limited PC memory.

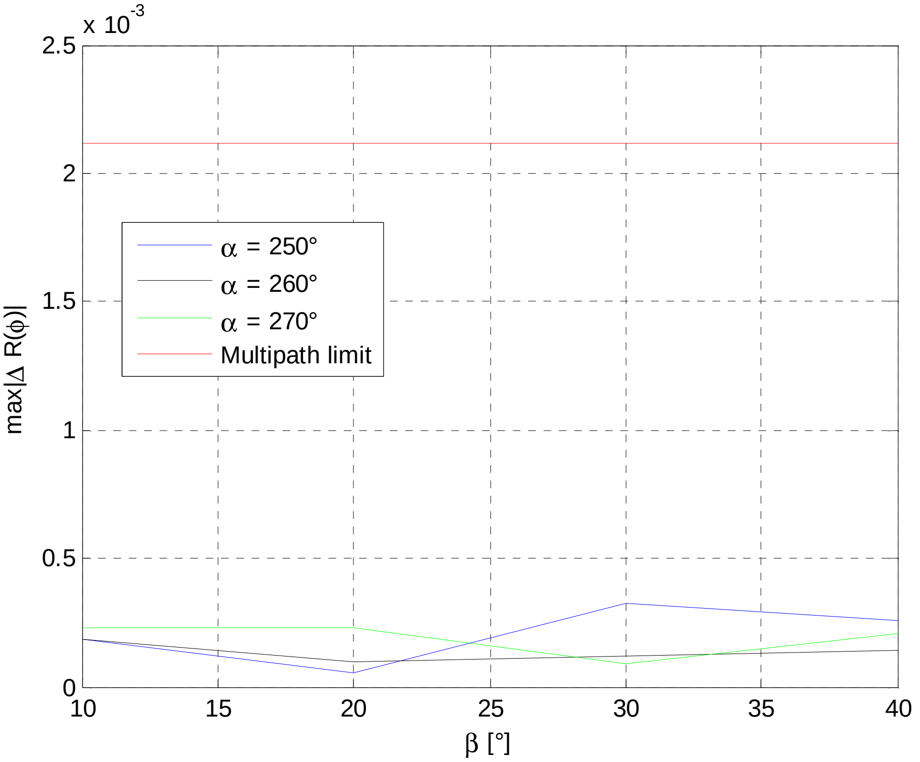

Figure 4-21: Maxima of differences of correlation functions (cylindrical body)

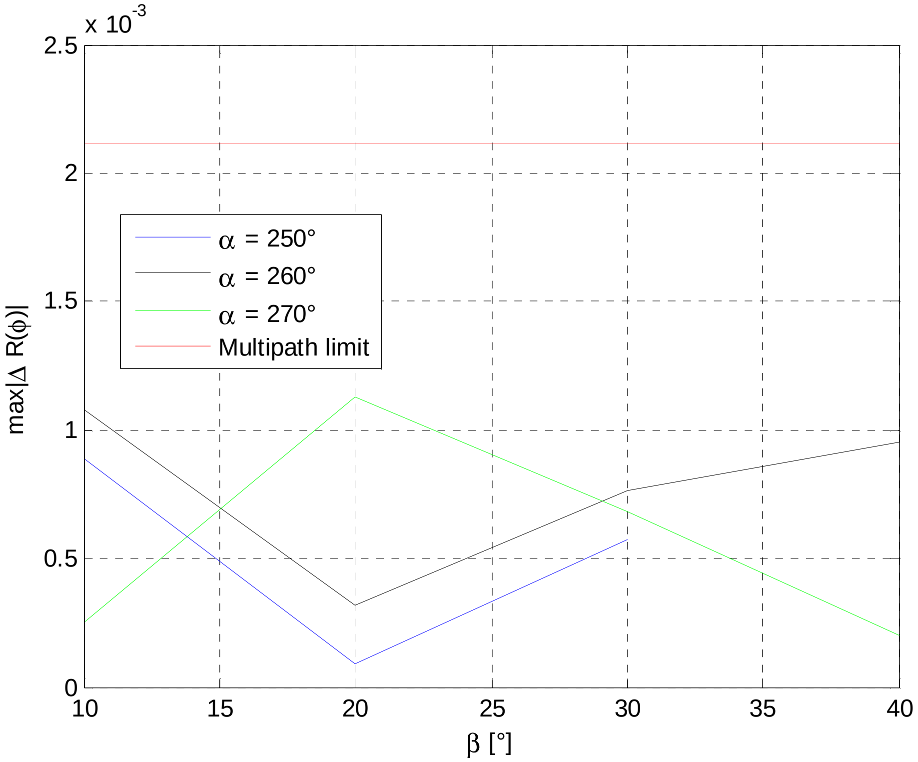

Figure 4-22: Maxima of differences of correlation functions (box-shaped body)

5 Analytical Error Modelling

5.1 Multipath Error Modelling Using the GTD

The GTD was proposed by J.B. Keller [*Graeme, 1980*], as an extension and improvement to the classic ray-based high-frequency approximation, Geometrical Optics (GO), by introducing additional rays (diffraction coefficients) to describe the diffracted field. The concept of diffracted rays was developed by Keller from the asymptotic evaluation of the known exact solution to scattering from simple shapes. These are referred to as the canonical problems for GTD. With this rigorous mathematical foundation, together with the simplicity of ray tracing techniques, we have the main attractions of the method.

In this work we will be concerned with GTD and its application to diffraction of time-harmonic fields from perfectly conducting bodies. Both GO and GTD are only accurate when the dimensions of objects being analysed are large relative to the wavelength of the field. In general, as the wavelengths of an electromagnetic field approach zero, the fields can be determined using geometric optics.

For diffraction by perfectly conducting smooth convex surfaces, such as a cylinder and a sphere, high-frequency solutions are obtained from the poorly convergent eigenfunction series using a Watson transform. The diffracted field in the shadow region decays exponentially away from the shadow boundary and is called a creeping wave.

5.1.1 Plane Wave Diffraction around a Circular Cylinder

When a plane wave is normally incident upon a perfectly conducting circular cylinder with radius *a* in a lossless medium, as shown in Figure 5-1 [*Graeme, 1980*],

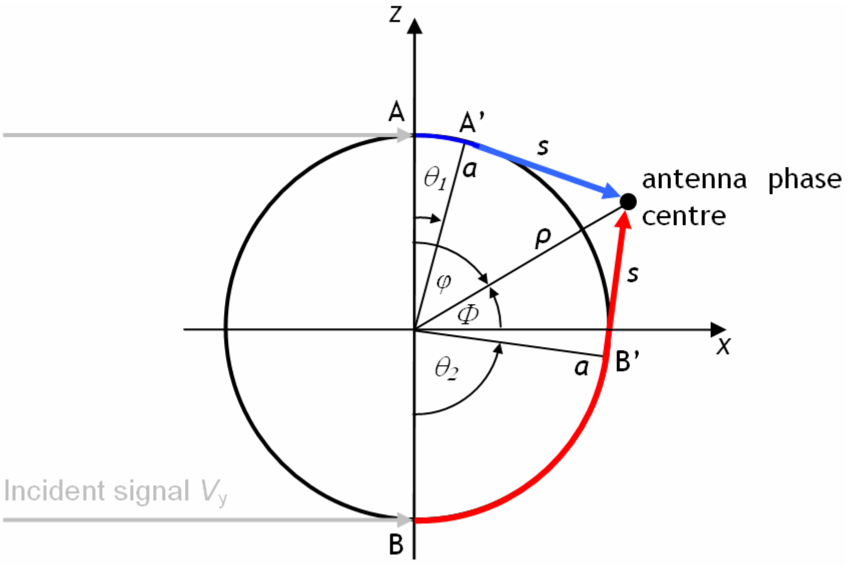

Figure 5-1: Plane wave diffraction at a circular cylinder

and has a field component V_y in the y-direction where

$$V_{\mathrm{y}} = \exp(-jk\rho\cos\phi) \tag{5-1}$$

then for large cylinders where $ka \gg 1$ the solution in the shadow region for electric and magnetic polarisation ($V_{\mathrm{y}} = E_{\mathrm{y}}$ or $V_{\mathrm{y}} = H_{\mathrm{y}}$) is given as [*Graeme, 1980*]

$$E_{\mathrm{y}} = E_{\mathrm{y}1} + E_{\mathrm{y}2} \tag{5-2}$$

$$H_{\mathrm{y}} = H_{\mathrm{y}1} + H_{\mathrm{y}2} \tag{5-3}$$

with

$$E_{\mathrm{y}1} = \sum_{n=1}^{N} D_n^e \left[\exp\left\{ -\left(jk + \Omega_n^e \right) \tau_1 \right\} \right] \frac{\exp(-jks)}{\sqrt{8j\pi ks}\left[1 - \exp\left\{ -\left(jk + \Omega_n^e \right) 2\pi a \right\} \right]} \tag{5-4}$$

$$E_{\mathrm{y}2} = \sum_{n=1}^{N} D_n^e \left[\exp\left\{ -\left(jk + \Omega_n^e \right) \tau_2 \right\} \right] \frac{\exp(-jks)}{\sqrt{8j\pi ks}\left[1 - \exp\left\{ -\left(jk + \Omega_n^e \right) 2\pi a \right\} \right]} \tag{5-5}$$

$$H_{\mathrm{y}1} = \sum_{n=1}^{N} D_n^m \left[\exp\left\{ -\left(jk + \Omega_n^m \right) \tau_1 \right\} \right] \frac{\exp(-jks)}{\sqrt{8j\pi ks}\left[1 - \exp\left\{ -\left(jk + \Omega_n^m \right) 2\pi a \right\} \right]} \tag{5-6}$$

$$H_{\mathrm{y}2} = \sum_{n=1}^{N} D_n^m \left[\exp\left\{ -\left(jk + \Omega_n^m \right) \tau_2 \right\} \right] \frac{\exp(-jks)}{\sqrt{8j\pi ks}\left[1 - \exp\left\{ -\left(jk + \Omega_n^m \right) 2\pi a \right\} \right]} \tag{5-7}$$

$$D_n^e = \left\{ Ai'(-\alpha_n) \right\}^{-2} 2\left(\frac{ka}{2} \right)^{\frac{1}{3}} \exp\left(\frac{j\pi}{6} \right) \tag{5-8}$$

$$D_n^m = \left\{ \alpha_n' \left\{ Ai(-\alpha_n') \right\}^2 \right\}^{-1} 2\left(\frac{ka}{2} \right)^{\frac{1}{3}} \exp\left(\frac{j\pi}{6} \right) \tag{5-9}$$

$$s = \sqrt{\left(\rho^2 - a^2 \right)} \tag{5-10}$$

$$k = \frac{2\pi}{\lambda} \tag{5-11}$$

$$\Omega_n^e = \frac{\alpha_n}{a} \left(\frac{ka}{2} \right)^{\frac{1}{3}} \exp\left(\frac{j\pi}{6} \right) \tag{5-12}$$

$$\Omega_n^m = \frac{\alpha'_n}{a} \left(\frac{ka}{2} \right)^{\frac{1}{3}} \exp\left(\frac{j\pi}{6} \right) \tag{5-13}$$

$$\theta_1 = \frac{\pi}{2} - \phi - \cos^{-1}\left(\frac{a}{\rho}\right) \tag{5-14}$$

$$\theta_2 = \frac{\pi}{2} + \phi - \cos^{-1}\left(\frac{a}{\rho}\right) \tag{5-15}$$

$$\tau_1 = \theta_1 a \tag{5-16}$$

$$\tau_2 = \theta_2 a \tag{5-17}$$

and where $-\alpha_n$ are the zeros of the Airy function *Ai* and $-\alpha'_n$ are the zeros of the Airy function derivative *Ai´*, some of which are given in Table 5-1. ρ is the distance between the centre of the cylinder and the antenna phase centre. ϕ is the angle between the x-axis and the line between the centre of the cylinder and the antenna phase centre (see Figure 5-1).

n	α_n	α'_n	$Ai(-\alpha'_n)$	$Ai'(-\alpha_n)$
1	2.338	1.019	0.536	0.701
2	4.088	3.248	-0.419	-0.803
3	5.521	4.820	0.380	0.865
4	6.787	6.163	-0.358	-0.911
5	7.944	7.372	0.342	0.947
6	9.023	8.488	-0.330	-0.978
7	10.040	9.535	0.321	1.004
8	11.009	10.528	-0.313	-1.028
9	11.936	11.475	0.307	1.049
10	12.829	12.385	-0.300	-1.068

Table 5-1: Airy function zeros and associated values [*Graeme, 1980*]

Each term in the series of equations (5-4) to (5-7) can now be interpreted in the following way. From the glancing points A and B on the cylinder in Figure 5-1 the incident rays travel around the surface a distance τ_1 and τ_2 respectively. While on the surface the amplitude of the rays decays exponentially due to the attenuation constant Ω which is defined in equation (5-12) and (5-13) for both polarisations. As seen from equation (5-12) and (5-13) this constant is complex and thus gives an additional phase shift to the rays travelling around the surface. At the points A‘ and B‘ the rays leave the surface tangentially and continue unattenuated to the field point P as if they were emanating from line sources at A‘ and B’. The terms D_n^e and D_n^m simply act as amplitude weighting factors for the rays.

In fact surface rays continue beyond A’ and B’, encircling the cylinder an infinite number of times, and each time shedding a ray at A’ and B’ to the field point P. The rays which propagate around the surface of the cylinder to give the diffracted field in the shadow are referred to as creeping rays. At each point on the surface a creeping ray is shed tangentially from the surface. There are, in theory, an infinite number of these creeping rays which encircle the cylinder an infinite number of times. Fortunately, the attenuation constant takes care of most of these rays. As already mentioned the exponential attenuation of the rays as they encircle the cylinder ensures that they quickly reduce to a negligible level. The Airy function roots $-\alpha_n$ and $-\alpha'_n$ increase with n and only the first one or two terms are of importance provided that τ_1 and τ_2 are non-zero. However, as $\tau_{1,2} \rightarrow 0$, an increasing number of terms in the series are required to maintain accuracy. Thus, in the vicinity of the shadow boundaries where $\tau_{1,2} \cong 0$, equations (5-2) and (5-3) are not a good representation of the field.

Only a normally incident plane wave is considered so far. When the field is at oblique incidence [*Graeme, 1980*], the only change for the cylinder is that its radius is replaced by the radius of curvature of the helical path the creeping ray now follows around the cylinder.

The calculation of the absolute values for the electric and magnetic field intensities of an APL L1 carrier wave (amplitude 1 V/m respectively 1 A/m) on the surface of a conducting cylinder with a diameter of 82 cm (like the one of our test bed in chapter 3) is shown in Figure 5-2. We use the same definition of the rotation angle like in chapter 3.1. The electric and magnetic field intensity are indicators for the expected C/N_0 because the RF signal power depends on them. We can see a similar behaviour of the field intensities and the C/N_0 measurements in the experimental tests conducted with the cylinder test bed in chapter 3. The minimum of the electric and magnetic field intensity occurs before the rotation angle reaches 180° indicating interference of the APL L1 signal with itself.

With the possibility of calculating field intensities on a conducting cylinder surface we can now assess the ranging errors due to code and carrier multipath on cylindrical aircraft bodies.

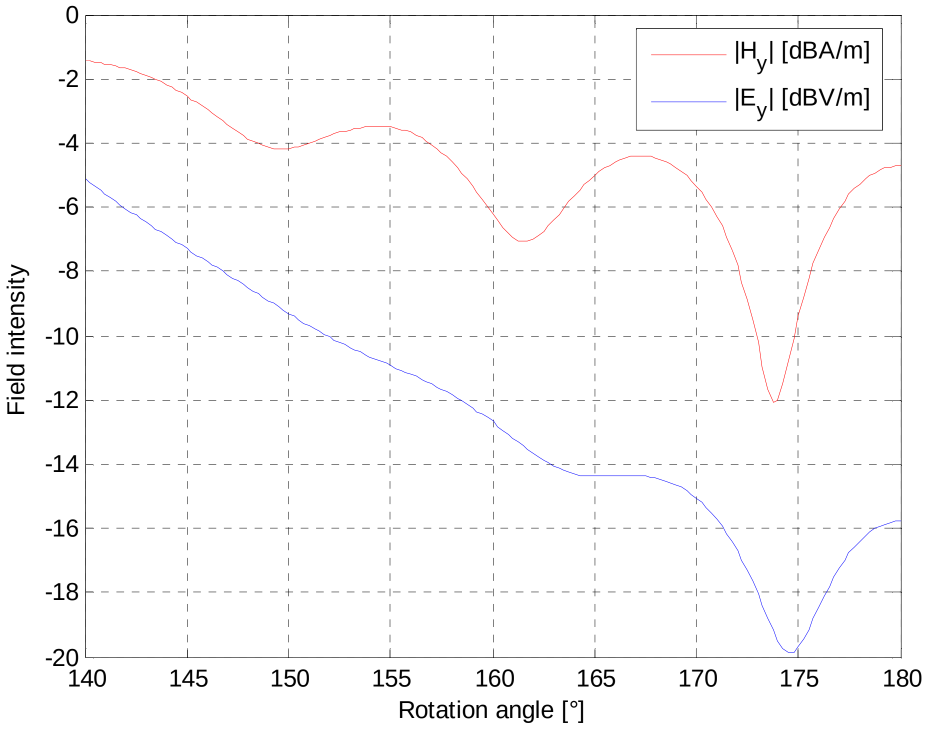

Figure 5-2: Absolute values of the field intensities around a cylinder

5.1.2 Multipath on a Cylindrical Aircraft Body

It must be assumed that an electromagnetic wave impinging on an aircraft body (like the one assumed in Figure 5-1) ends up with two signal components travelling along each side of the surface [*Biberger et al., 2005*]. Thus, any GNSS antenna mounted on this surface receives the compound signal consisting of both signal components (blue and red lines in Figure 5-1).

In the following, it is assumed that the GNSS antenna is mounted on top of the aircraft body which is modelled as a cylinder with radius a. The incident APL P-code signal comes from the left. The bank angle is denoted by φ.

Both signal components have different path lengths and show a phase shift with respect to each other. Thus, the superposition of both signal components can be interpreted as a special case of a multipath propagation where the signal with the shorter path length can be considered as the direct signal and the other one as the multipath signal. The following analyses try to assess the maximum errors due to code and carrier multipath for such a case.

The actual multipath performance of a given signal/receiver combination depends on a variety of signal and receiver parameters like signal type/modulation scheme, pre correlation bandwidth and filter characteristics, chipping rate of code, relative power levels of multipath signals, actual number of multipath signals, geometric path delay, correlator spacing, type of discriminator used for tracking and carrier frequency. Signal type respective modulation scheme, pre correlation bandwidth and the type of filter used for band-limiting the incoming signal determine the actual shape of the signal's correlation function which is used to set up the code discriminator. The chipping rate of the code determines the code chip length T_C which finally determines the resulting ranging error caused by code multipath. The remaining parameters represent the multipath environment (multipath relative amplitude, geometric path delay, number of multipath signals). With respect to the following analyses, these signal, receiver and environmental parameters are used:

Signal environment:

- P-code (BPSK(10), T_C =29.305 m) signals
- Consideration of code and carrier multipath at L1
- Consideration of one single multipath signal

Receiver parameters:

- Code discriminator: Early minus late
- Correlator spacing: d=1 (P-code)
- Pre correlation bandwidth: 24 MHz (P-code)
- Type of filter: Ideal band pass

All other required parameters can be derived from the underlying geometric conditions (geometric path delay and multipath relative power or amplitude). According to the signal and receiver parameters listed above, the correlation and discriminator functions can be computed [*Oppenheim and Schafer, 1995*] as illustrated in Figure 5-3 and Figure 5-4.

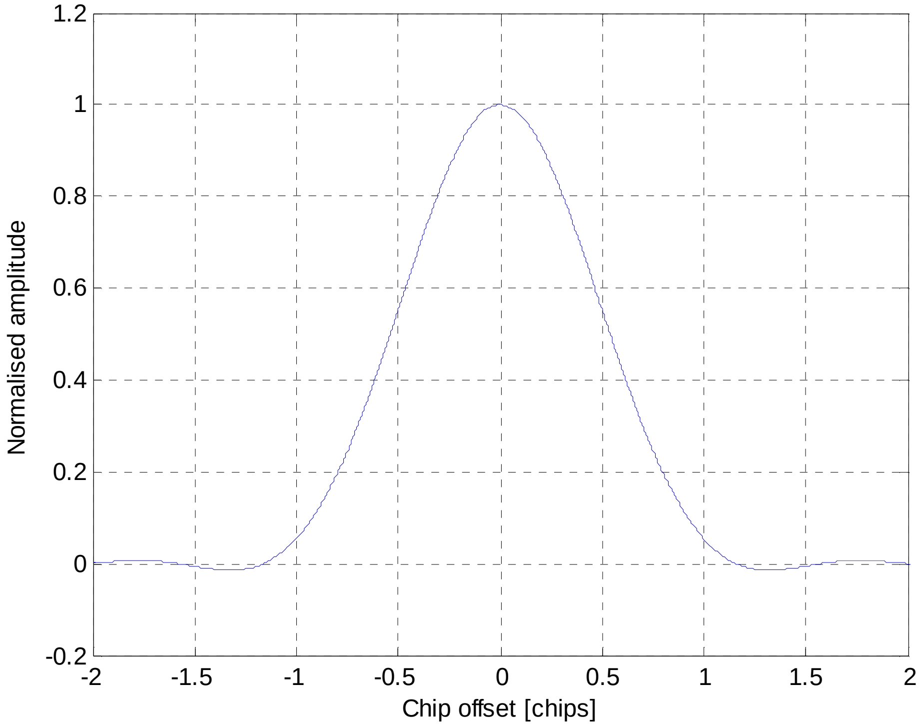

Figure 5-3: Autocorrelation function of the considered P-code signal

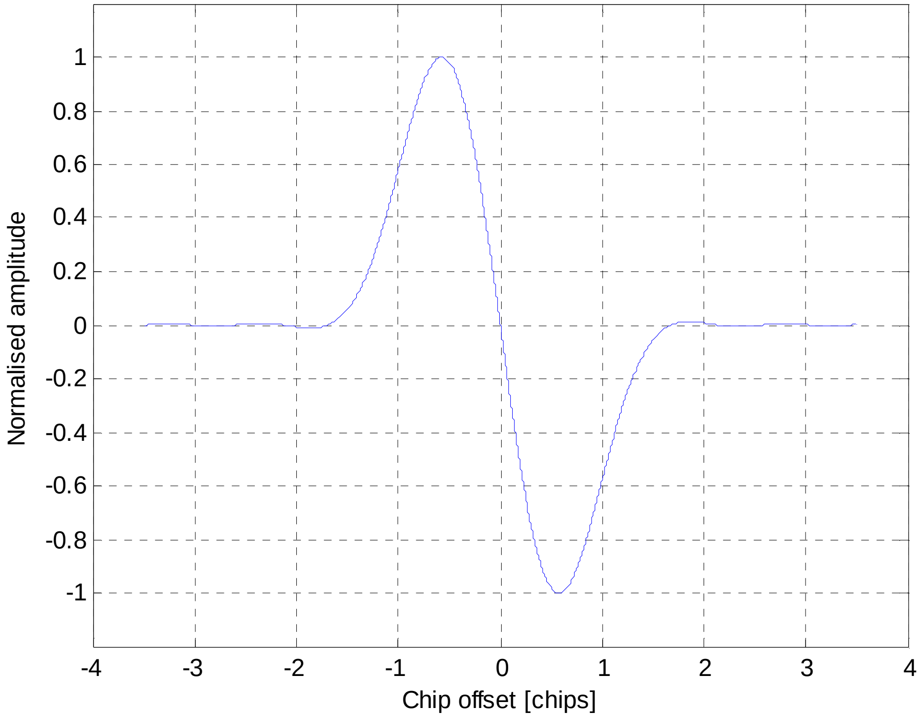

Figure 5-4: Discriminator function of the considered P-code signal

Errors caused by code multipath are commonly expressed in the form of so-called "multipath error envelopes". These diagrams illustrate the resulting ranging errors as a function of the geometric path delay assuming idealised conditions (consideration of one single multipath signal, LOS component always available, constant multipath relative power for all geometric path delays). They can be generated by simply overlaying the correlation functions for the direct and the multipath component for different geometric path delays by forming the resulting discriminator function and finally by determining its zero-crossing. The deviation of the resulting zero-crossing from the chip offset $\phi=0$ [chips] is the code multipath error.

The presence of multipath signals also affects the carrier tracking performance. According to [*Braasch, 1995*], the phase tracking error ϑ [m] caused by carrier multipath can be expressed as

$$\tan\vartheta = \frac{\eta R(\phi-\delta')\sin\chi}{R(\phi)+\eta R(\phi-\delta')\cos\chi}, \tag{5-18}$$

where χ is the multipath relative phase (relative to the phase of the direct signal) which is related to the geometric path delay δ and the carrier wavelength λ (both expressed in [m]) via

$$\chi = \frac{2\pi\delta}{\lambda}. \tag{5-19}$$

According to equation (5-18), the multipath error ϑ depends on the multipath relative amplitude η, the correlation function R and the geometric path delay δ' [chips].

In order to compute the maximum ranging errors caused by multipath due to signal creeping on a cylindrical aircraft body, the code and carrier-phase multipath error envelopes for the corresponding multipath relative amplitude η have been computed. The amplitude ratio η between the two signal components (see equations (5-4) and (5-5)) can be calculated by

$$\eta = \frac{\left|E_{y2}\right|}{\left|E_{y1}\right|}. \tag{5-20}$$

Note that GNSS patch antennas usually use the electric field of the incident RF signal to transfer it into an imaging internal electric current.

Figure 5-5 shows the amplitude ratio η as a function of the bank angle φ. The ratio η is exponentially increasing with increasing bank angles φ and η starts to increase later for larger cylinder radii *a*.

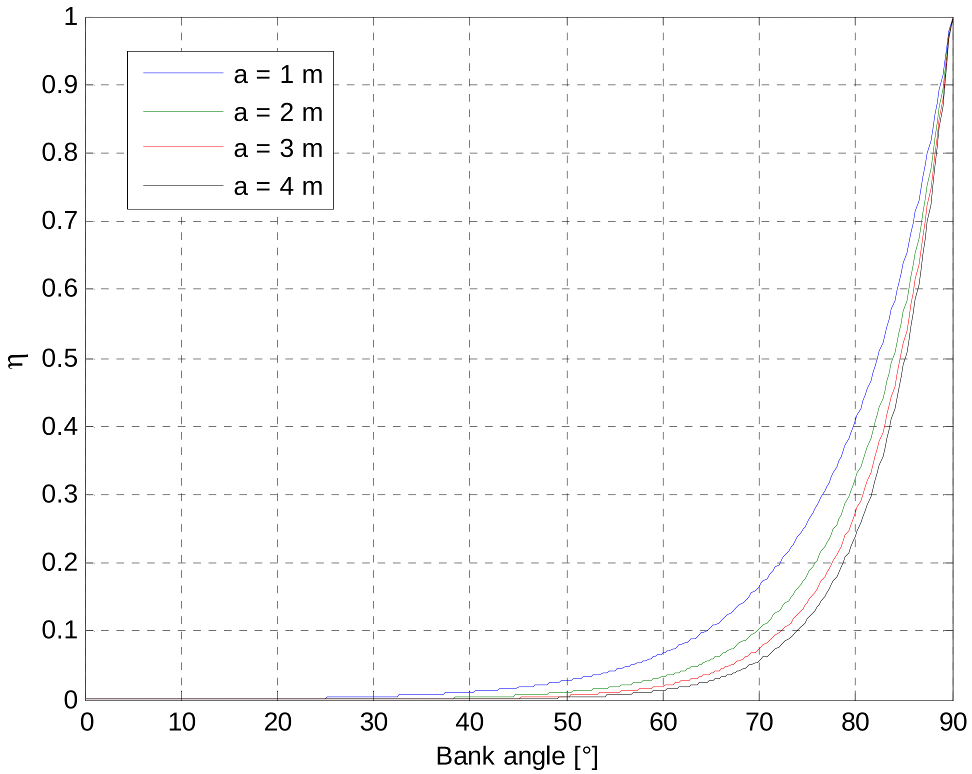

Figure 5-5: Amplitude ratio *η* for different cylinder radii *a*

By extracting the ranging errors for the respective geometric path delay δ relating to that amplitude ratio η, the ranging error envelopes for code and carrier-phase as a function of the bank angle φ can be generated.

The geometric path delay δ can be expressed as a function of the bank angle φ [rad] and the radius a [m] by

$$\delta = 2(\frac{\pi}{2} - \varphi)a\,. \tag{5-21}$$

The code and carrier-phase ranging error envelopes for different cylinder radii a are illustrated in Figure 5-6 and Figure 5-7.

It can be derived from Figure 5-6 that the occurring code ranging errors become larger when the radius of the cylinder is increasing. Another result is that code ranging errors start to increase later for larger aircraft bodies and obviously occur only for very large bank angles φ (>50°), whereas small bank angles do not cause such errors.

Similarly for the code ranging errors, carrier-phase tracking errors occur only for very large bank angles φ (>60°) (see Figure 5-7).

However, bank angles are limited to approximately 30° for typical aircraft manoeuvres according to standard instrument flight procedures and are even smaller for an aircraft on final landing approach (<10°). Therefore, multipath errors on aircraft bodies due to signal creeping effects can be neglected provided that the incident APL signal comes from the side as illustrated in Figure 5-1. This is nearly the case, if the APL has enough offset from the glide slope.

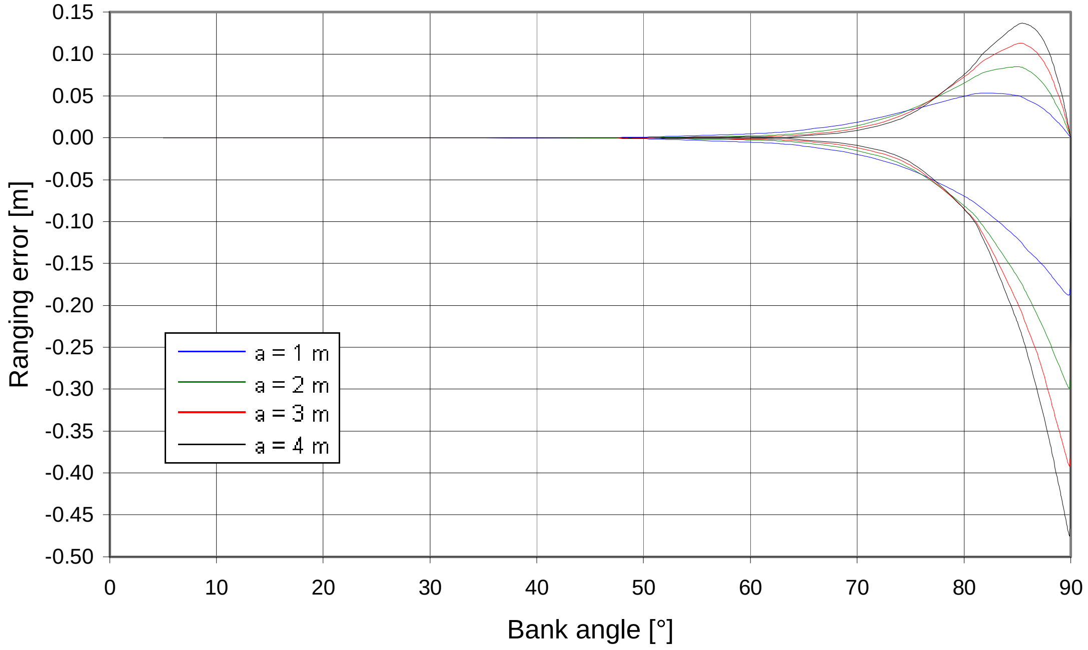

Figure 5-6: Envelopes of pseudorange error for P-code observations

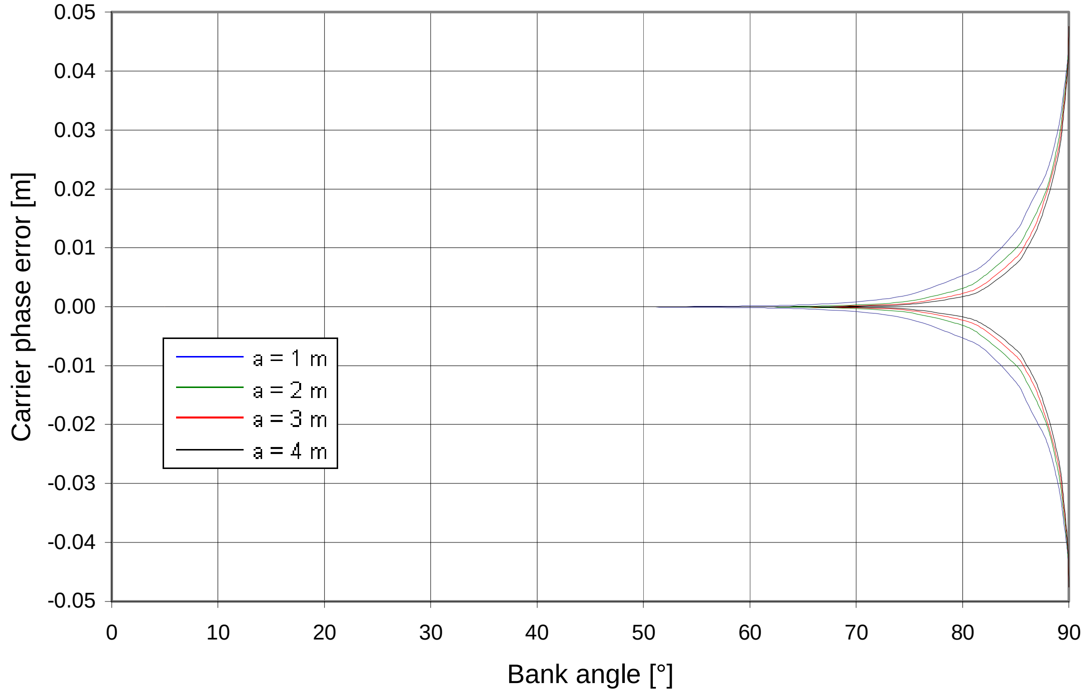

Figure 5-7: Envelopes of carrier-phase error for P-code observations

5.2 Signal Path Extension on Aircraft Bodies

5.2.1 Derivation

The intention of this chapter is to derive analytically the signal path extension on aircraft fuselages [*Biberger et al., 2005*]. Therefore the following assumptions are made:

- The signal source is far enough from the aircraft and a plane wave can be assumed.
- The signal is creeping along geodetic lines on conducting surfaces [*Graeme, 1980*].
- The signal comes either from the right or from the left side of the airframe and does not propagate along the aircraft nose (because the APL is located offset from the glide path).
- The fuselage can be described by a box with rounded edges. This description includes the special case of a circular cylinder.
- The antenna is top-mounted and centred on the fuselage. The position of the phase centre is on the surface of the aircraft body.

In the following, the coordinates given by Table 5-2 are used.

y-direction	horizontal projection of the direction signal source → aircraft antenna
z-direction	zenith direction
x-direction	completes the orthonormal right system
0	signal source

Table 5-2: Definition of the coordinate system

The elevation of the aircraft is given by β (see Figure 5-8). α is the angle between the y-axis and the horizontal projection of the longitudinal axis of the fuselage (see Figure 5-9). For the pitch angle θ, positive angles are associated with an ascending aircraft. A positive bank angle φ describes a left banking aircraft. The radius of the fuselage's rounding is denoted by a and the distance from the phase centre of the antenna to the rounded edge is denoted by w (see Figure 5-10).

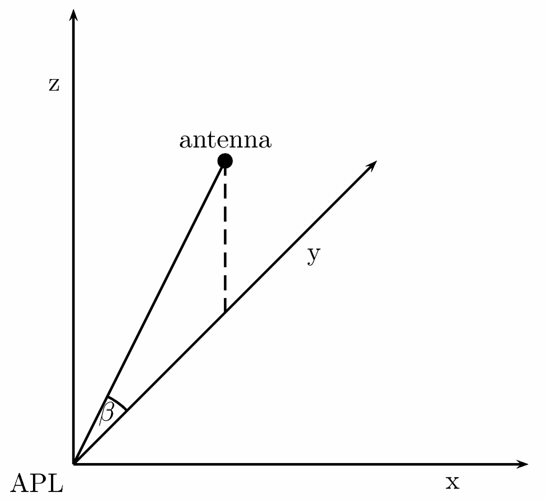

Figure 5-8: Definition of the angle ***β***

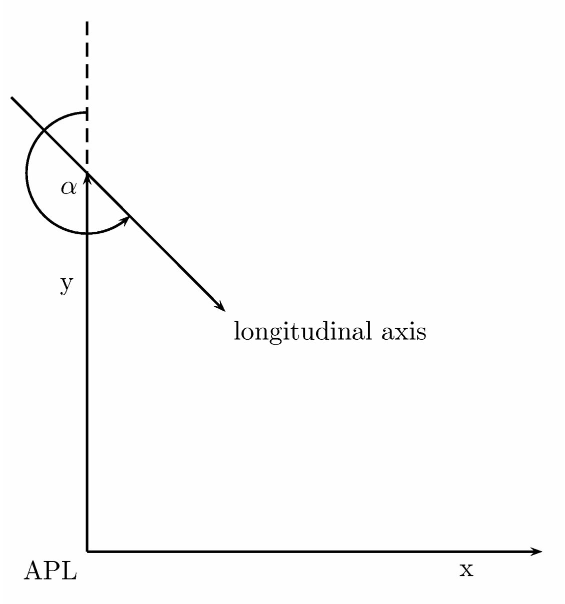

Figure 5-9: Definition of the angle ***α***

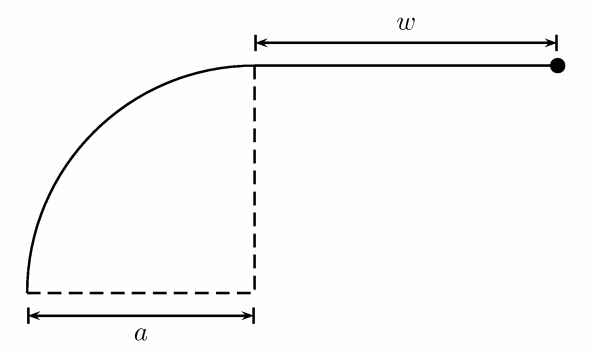

Figure 5-10: Definition of the radius ***a*** and the distance ***w***

In these terms, the direction of the APL signal rays is given by

$$\mathbf{s}(\beta)=\mathbf{R}_{\mathrm{x}}(\beta)\begin{pmatrix}0\\1\\0\end{pmatrix}=\begin{pmatrix}0\\\cos(\beta)\\\sin(\beta)\end{pmatrix} \tag{5-22}$$

and the direction of the longitudinal axis of the aircraft can be expressed by

$$\mathbf{r}(\alpha,\theta)=\mathbf{R}_{\mathrm{z}}(\alpha)\mathbf{R}_{\mathrm{x}}(\theta)\begin{pmatrix}0\\1\\0\end{pmatrix}=\begin{pmatrix}-\cos(\theta)\sin(\alpha)\\\cos(\theta)\cos(\alpha)\\\sin(\theta)\end{pmatrix}. \tag{5-23}$$

The rotation matrices write

$$\mathbf{R}_{\mathrm{x}}(\alpha)=\begin{pmatrix}1&0&0\\0&\cos(\alpha)&-\sin(\alpha)\\0&\sin(\alpha)&\cos(\alpha)\end{pmatrix} \tag{5-24}$$

$$\mathbf{R}_{\mathrm{y}}(\alpha)=\begin{pmatrix}\cos(\alpha)&0&-\sin(\alpha)\\0&1&0\\\sin(\alpha)&0&\cos(\alpha)\end{pmatrix} \tag{5-25}$$

$$\mathbf{R}_{\mathrm{z}}(\alpha)=\begin{pmatrix}\cos(\alpha)&-\sin(\alpha)&0\\\sin(\alpha)&\cos(\alpha)&0\\0&0&1\end{pmatrix}. \tag{5-26}$$

Only tangentially impacting signal rays will start to creep on the surface of the aircraft. Therefore one determines the tangent plane of the aircraft containing the direction of the signal rays. This plane can be specified by the angle μ between the z-axis and its outer normal (see Figure 5-11).

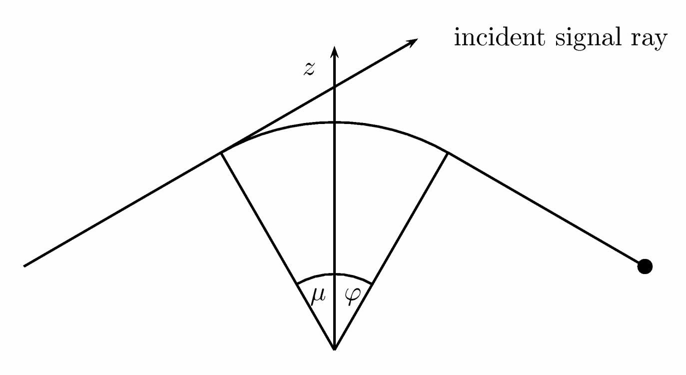

Figure 5-11: Definition of the angle *μ*

μ can be computed by resolving

$$\det\left(\mathbf{r}(\alpha,\theta),\mathbf{s}(\beta),\mathbf{R}_{\mathrm{z}}(\alpha)\mathbf{R}_{\mathrm{x}}(\theta)\mathbf{R}_{\mathrm{y}}(\mu)\begin{pmatrix}-1\\0\\0\end{pmatrix}\right)=0\,. \tag{5-27}$$

This yields to

$$\mu(\alpha,\beta,\theta)=-\arctan\left(\frac{\cos(\alpha)\sin(\theta)\cos(\beta)-\cos(\theta)\sin(\beta)}{\sin(\alpha)\cos(\beta)}\right). \tag{5-28}$$

Thus, the total angle of rotation is given by

$$\tilde{\xi}(\alpha,\beta,\theta,\varphi)=\mu(\alpha,\beta,\theta)-\varphi\,, \tag{5-29}$$

or neglecting the direction of the angle, but recognizing that the main signal will travel at most 90° on the surface

$$\begin{aligned}\xi(\alpha,\beta,\theta,\varphi)=&\left|\operatorname{mod}\left(\mu(\alpha,\beta,\theta)-\varphi,\pi\right)\right|\mathit{sign}\left({}^{\pi}\!/_{2}-\left|\operatorname{mod}\left(\mu(\alpha,\beta,\theta)-\varphi,\pi\right)\right|\right)+\\&\mathrm{Heaviside}\left(\left|\operatorname{mod}\left(\mu(\alpha,\beta,\theta)-\varphi,\pi\right)\right|-{}^{\pi}\!/_{2}\right)\pi\end{aligned} \tag{5-30}$$

where the Heaviside-function is defined by

$$\mathrm{Heaviside}(p)=\begin{cases}0, & p\le 0\\ 1, & p>0\end{cases}. \tag{5-31}$$

On the surface of the fuselage the signal rays will propagate on geodetic lines. As the fuselage is composed of parts of planes and circular cylinders, the geodetic lines are known to be lines and helical paths crossing the natural lines of longitude and lines of latitude under constant angles. The length of a helical path dependent of the travelled angle ξ, the radius a of the cylinder and the obliquity ω of the helix is computed (looking without loss of generality to the helix

$$\boldsymbol{\kappa}(t,a,\omega)=\begin{pmatrix}-\sin(t)a\\ \cos(t)a\\ b(a,\omega)t\end{pmatrix} \tag{5-32}$$

around the z-axis describing an angle of ω degrees with the lines of latitude) by

$$\Lambda(a,\xi,\omega)=\int_0^{\xi}\left\|\frac{d\boldsymbol{\kappa}(t,a,\omega)}{dt}\right\|dt=\xi\sqrt{a^2+b(a,\omega)^2}=\frac{\xi a}{\cos(\omega)} \tag{5-33}$$

with

$$b(a,\omega)=a\sqrt{\frac{1}{\cos^2(\omega)}-1}\,. \tag{5-34}$$

One can derive equation (5-34) by solving the equation

$$\cos(\omega) = \frac{\left\langle \frac{d\boldsymbol{\kappa}}{dt}(0), \begin{pmatrix} -1 \\ 0 \\ 0 \end{pmatrix} \right\rangle}{\left\| \frac{d\boldsymbol{\kappa}}{dt}(0) \right\|_2 \cdot \left\| \begin{pmatrix} -1 \\ 0 \\ 0 \end{pmatrix} \right\|_2}. \tag{5-35}$$

The feed of the helix is computed to

$$f(a,\xi,\omega) = a\xi\sqrt{\frac{1}{\cos^2(\omega)} - 1}. \tag{5-36}$$

With

$$\tilde{\Omega}(\alpha,\beta,\theta) = \arccos\left(\left\langle s(\beta), r(\alpha,\theta)\right\rangle\right) = \arccos\left(\cos(\alpha)\cos(\beta)\cos(\theta) + \sin(\beta)\sin(\theta)\right) \tag{5-37}$$

denoting the angle between the signal rays and the longitudinal axis of the fuselage and with $\Omega(\alpha,\beta,\theta)$ defined analogous to equation (5-30), the “cut” angle between the signal rays and the lines of longitudinal. The “cut” angle between the signal rays and the lines of latitude reads to

$$\omega(\alpha,\beta,\theta) = \frac{\pi}{2} - \Omega(\alpha,\beta,\theta). \tag{5-38}$$

With the above equations one is able to compute the travelled way of the creeping wave (see Figure 5-12) by

$$\upsilon(\alpha,\beta,\theta,\varphi,a,w) = \frac{\xi(\alpha,\beta,\theta,\varphi)\,a + w}{\cos\left(\omega(\alpha,\beta,\theta)\right)}. \tag{5-39}$$

To determine the signal path extension, one has to compare the length of the travelled signal path (5-39) and the distance between the wave front containing the impact point of the signal ray and the antenna. Therefore one uses the new coordinate frame described in Table 5-3.

In this coordinate frame the normal vector of the wave front simply reads

$$\mathbf{n}(\alpha,\beta,\theta) = \begin{pmatrix} \cos\left(\omega(\alpha,\beta,\theta)\right) \\ \sin\left(\omega(\alpha,\beta,\theta)\right) \\ 0 \end{pmatrix}. \tag{5-40}$$

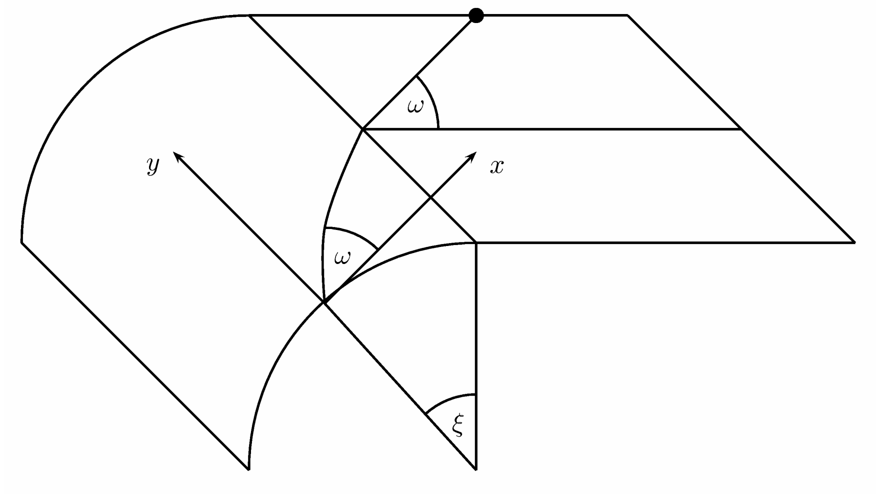

Figure 5-12: Signal path of a creeping wave

x-direction	direction of the line of latitude at the impact point of the signal ray towards the antenna
y-direction	direction of the line of longitude at the impact point of the signal ray towards the antenna
z-direction	completes the orthonormal right system
0	impact point of the signal ray

Table 5-3: Definition of the new coordinate system

Hence, one only has to compute the antenna's x- and y-coordinate to determine the distance by substituting them in the normal formulation of the wave front's plane. The y-coordinate is given by the feed of the helix plus the projection on the y-axis of the slant line on the plane part of the fuselage:

$$\mathrm{y}(\alpha,\beta,\theta,\varphi,a,w)=a\sqrt{\frac{1}{\cos^2\left(\omega(\alpha,\beta,\theta)\right)}-1}\,\xi(\alpha,\beta,\theta,\varphi)+\tan\left(\omega(\alpha,\beta,\theta)\right)w. \tag{5-41}$$

The x-coordinate reads (see Figure 5-13)

$$\mathrm{x}(\alpha,\beta,\theta,\varphi,a,w)=\sin\left(\xi(\alpha,\beta,\theta,\varphi)\right)a+\cos\left(\xi(\alpha,\beta,\theta,\varphi)\right)w. \tag{5-42}$$

Altogether the distance is given by

$$v(\alpha,\beta,\theta,\varphi,a,w)=\left\langle \mathbf{n}(\alpha,\beta,\theta),\begin{pmatrix}\mathrm{x}(\alpha,\beta,\theta,\varphi,a,w)\\ y(\alpha,\beta,\theta,\varphi,a,w)\\ 0\end{pmatrix}\right\rangle \tag{5-43}$$

and the signal path extension reads

$$\Delta(\alpha,\beta,\theta,\varphi,a,w)=\left(\upsilon(\alpha,\beta,\theta,\varphi,a,w)-\nu(\alpha,\beta,\theta,\varphi,a,w)\right)\text{Heaviside}\left(\Theta(\alpha,\beta,\theta,\varphi)\right) \tag{5-44}$$

where the substitution of the (negative) position of the APL in the normal formulation of the antenna's horizon plane

$$\Theta(\alpha,\beta,\theta,\varphi)=sign\left(\left\langle \mathbf{R}_z(\alpha)\mathbf{R}_x(\theta)\mathbf{R}_y(\varphi)\begin{pmatrix}0\\0\\1\end{pmatrix},\mathbf{s}(\beta)\right\rangle\right) \tag{5-45}$$

is indicating a direct line-of-sight by -1. The second factor is necessary because all considerations are only valid, if the antenna is in the signal shadow.

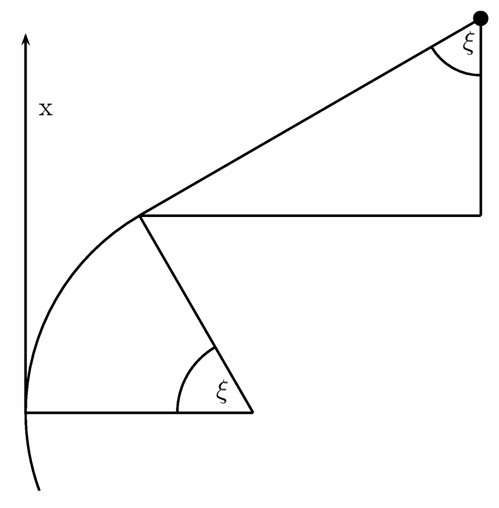

Figure 5-13: Sketch for equation (5-42)

5.2.2 Verification

For verification, we compare the analytically derived signal path extension with the numerical results for a cylindrical (a=1 m, w=0 m) and a box shaped (w=0.75 m, a=0 m) aircraft body. Figure 5-14 and Figure 5-15 show the analytical and numerical results for different angles α and β. The pitch angle θ and the bank angle φ are in each case 0°. Both the analytically derived SPE values for the box-shaped body and the cylindrical body show a good match with the numerically calculated values.

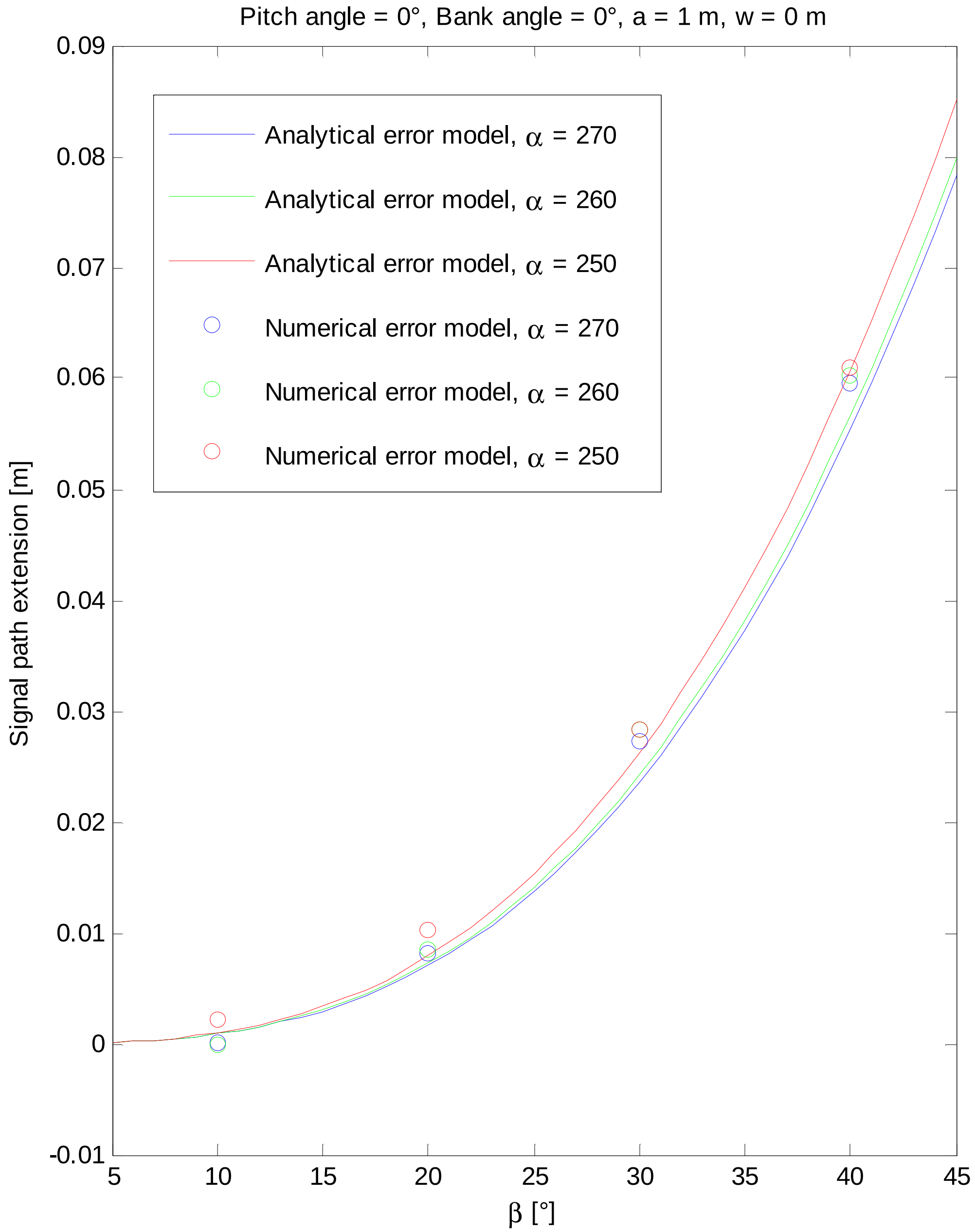

Figure 5-14: Analytical and numerical results for a cylindrical aircraft body

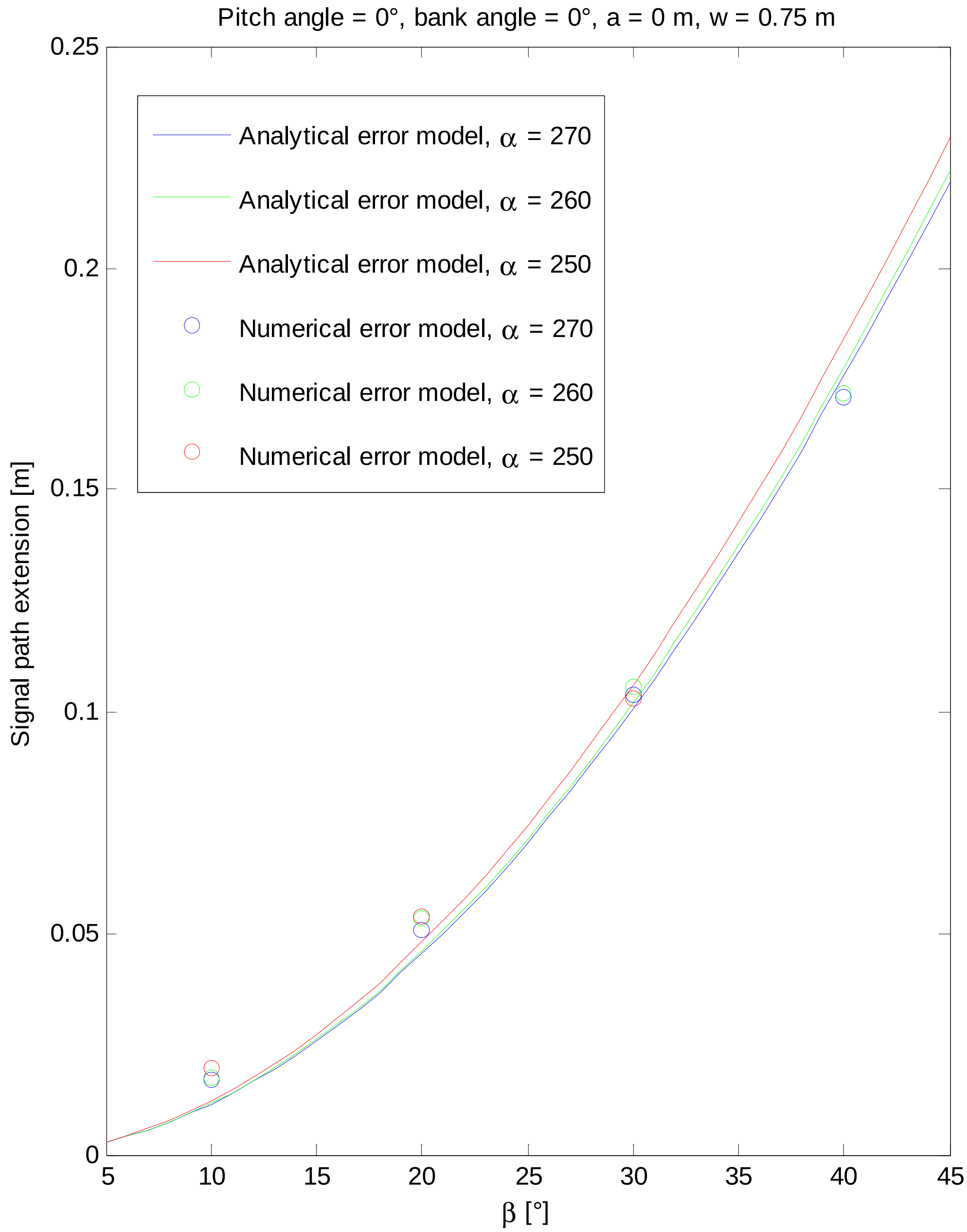

Figure 5-15: Analytical and numerical results for a box-shaped aircraft body

5.2.3 Results

Figure 5-16 to Figure 5-23 show the graphs of the signal path extension function for cylindrical and box-shaped fuselages for typical aircraft manoeuvres in a flight's final phases. The first examples (see Figure 5-16 to Figure 5-21) illustrate the signal path extension function for an Airbus A380 with a cylindrical fuselage (a=3.57 m, w=0 m) and a Shorts 360 with a box-shaped fuselage (w=0.9 m, a=0.1 m) depending on various angles like the pitch angle θ, the bank angle *φ* and *α*. The elevation angle *β* of the aircraft is 3°. This means that the aircraft has a nominal glide path angle of approximately 3°, if *α* is close to 180°. The SPE values are increasing for increasing bank angles *φ* (away from the APL) and increasing pitch angles *θ*. For high pitch angles *θ* the SPE values are increasing with decreasing angles *α* (see Figure 5-17 and Figure 5-20). It should be noted that with increasing angle *α*, the distance to the APL is decreasing.

This described behaviour of the SPE function leads to worst case ranging error graphs shown in the colour blue in Figure 5-22 and Figure 5-23. The SPE function is illustrated here depending on the fuselage radius *a* (*w*=0 m) for cylindrical aircraft bodies (see Figure 5-22) or the distance *w* (*a*=0 m) for box-shaped aircraft bodies (see Figure 5-23) for assumed maximum positive pitch angles *θ* of 10° and assumed maximum bank angles *φ* of 30°. These curves in the colour blue can be used to determine the maximum ranging errors for different airframe sizes due to SPE for an aircraft on final landing approach.

An aircraft on a stable landing approach with positive pitch angles *θ* not greater than 5° and bank angles *φ* not greater than 10° does experience only small ranging errors as shown by the red graphs in Figure 5-22 and Figure 5-23.

As a result, cylindrical fuselages have a great advantage because their SPE values are much smaller than the SPE values for box-shaped aircraft bodies.

It should be noted here that SPE is independent from the signal of the APL and therefore usable for any future APL signal structures.

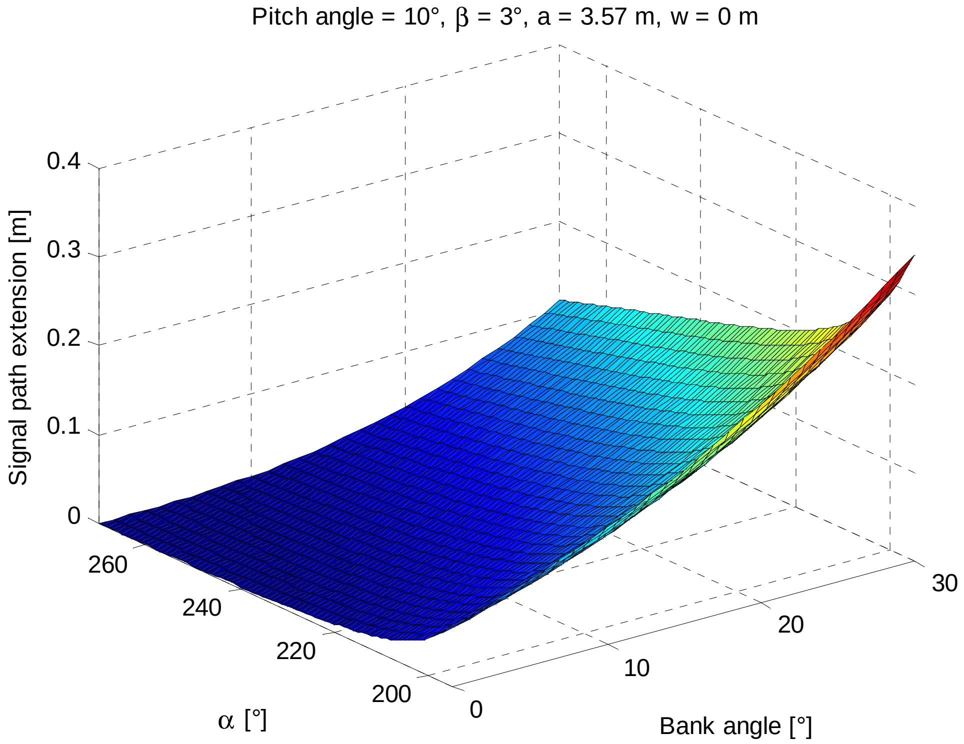

Figure 5-16: SPE of a cylindrical body (A380) for different angle *α* and *φ*

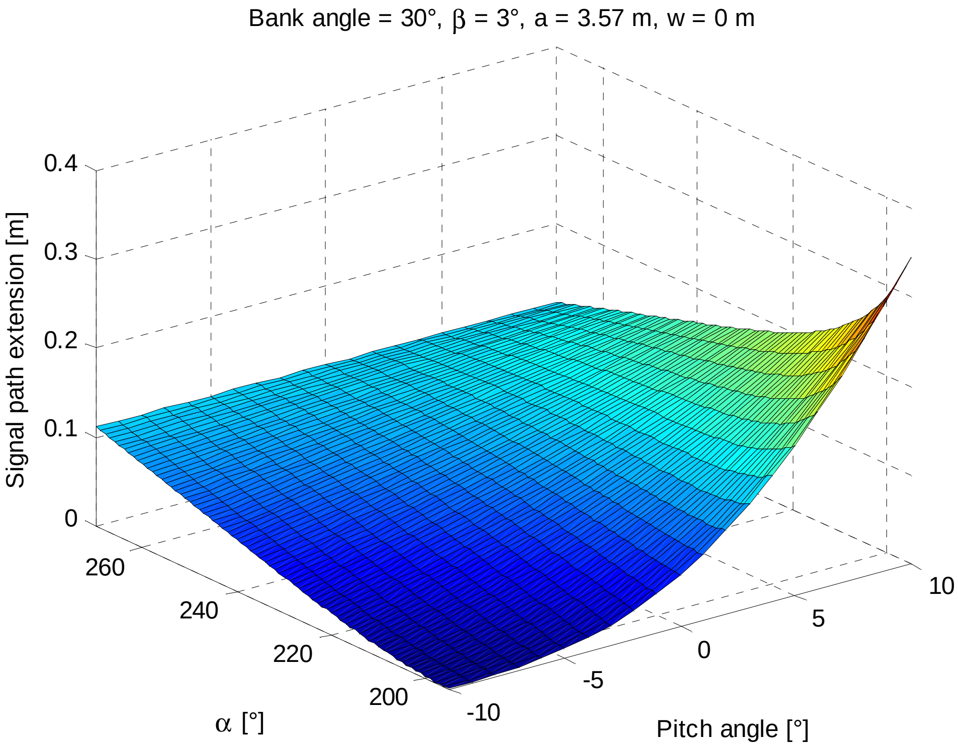

Figure 5-17: SPE of a cylindrical body (A380) for different angle *α* and *θ*

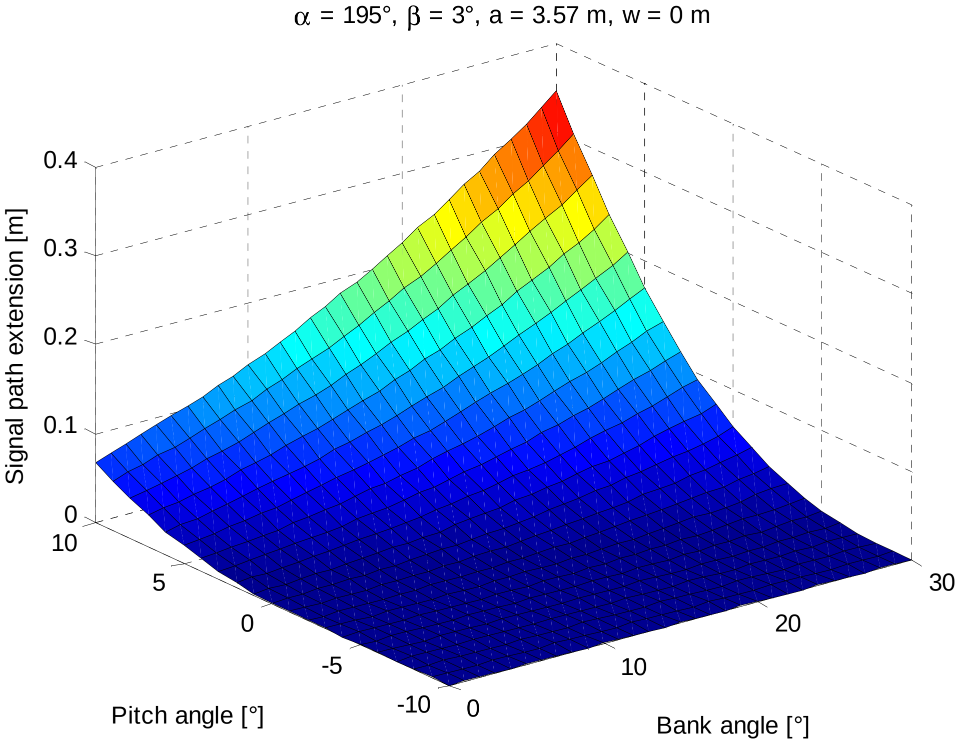

Figure 5-18: SPE of a cylindrical body (A380) for different angle *θ* and *φ*

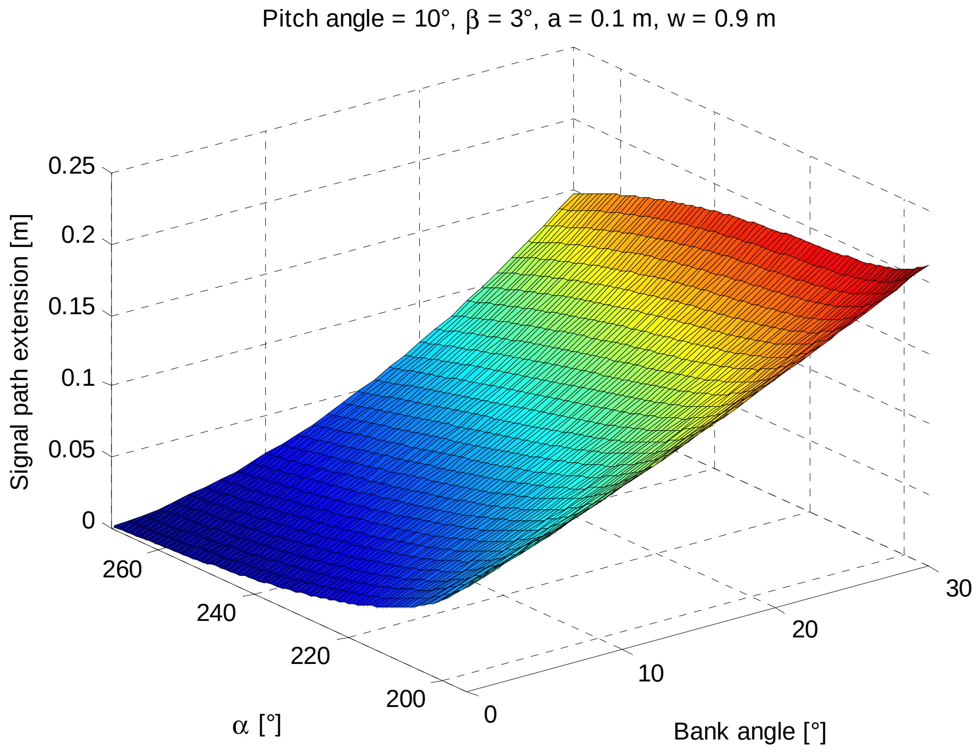

Figure 5-19: SPE of a box-shaped body (Shorts 360) for different angle *α* and *φ*

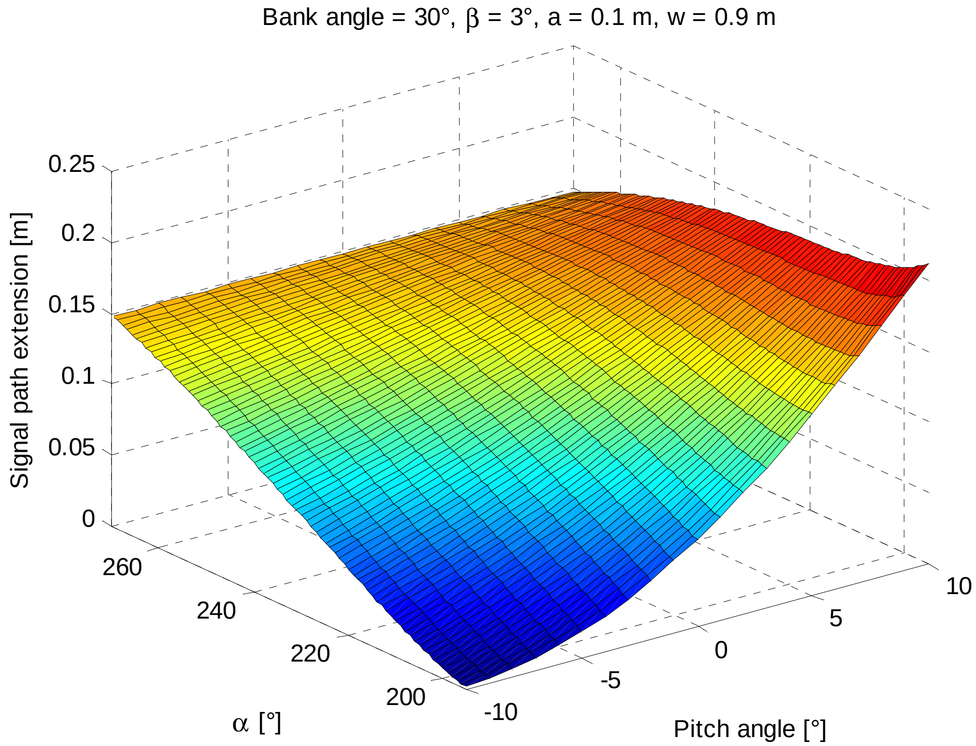

Figure 5-20: SPE of a box-shaped body (Shorts 360) for different angle *α* and *θ*

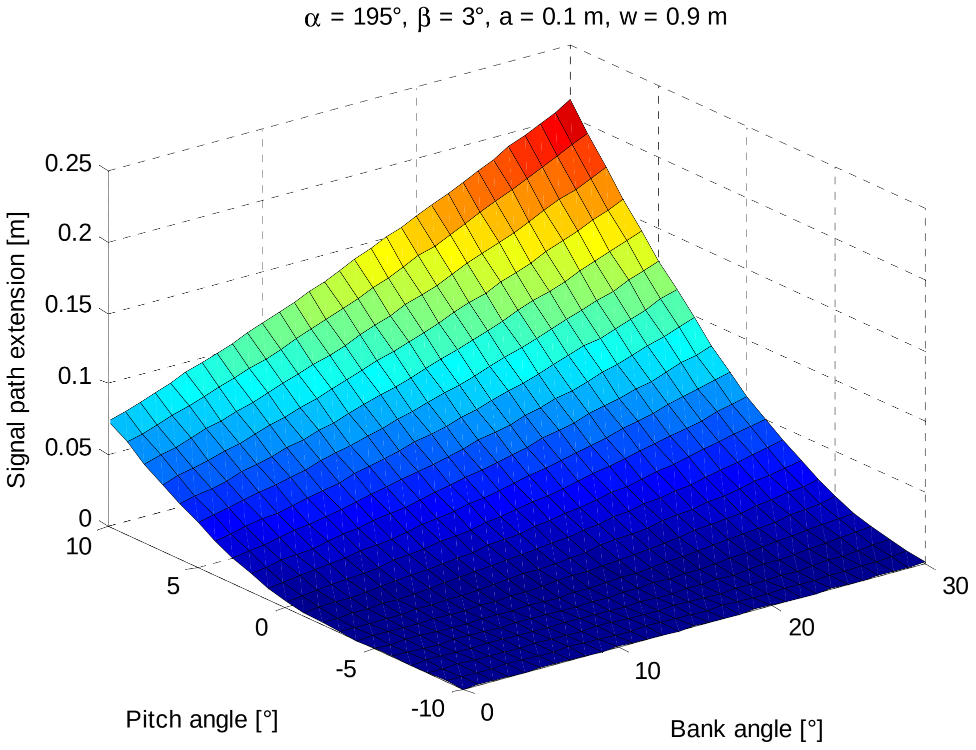

Figure 5-21: SPE of a box-shaped body (Shorts 360) for different angle *θ* and *φ*

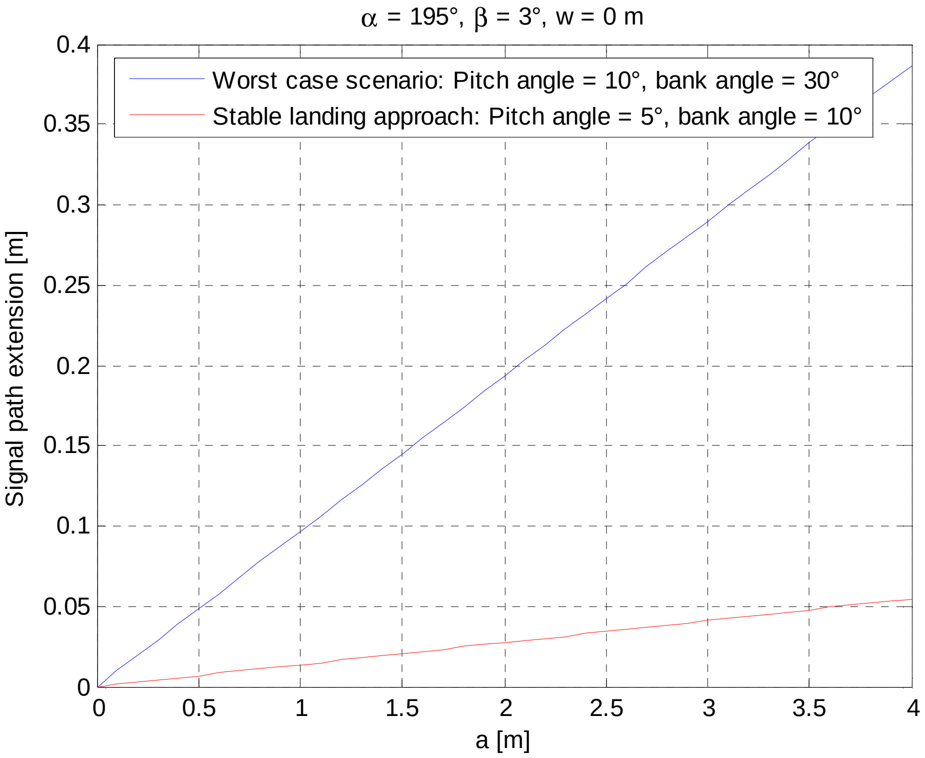

Figure 5-22: SPE of a cylindrical body for different radii *a*

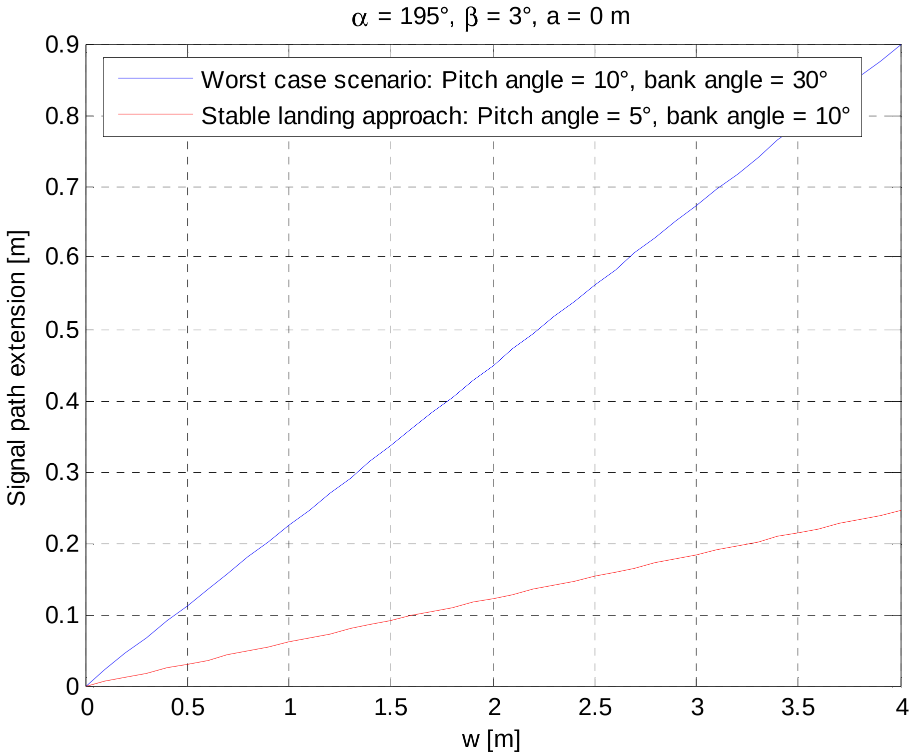

Figure 5-23: SPE of a box-shaped body for different distances *w*

6 Conclusion

With the methods of modelling APL signal propagation and reception on conducting aircraft surfaces, presented in this PhD thesis, the following conclusions regarding error effects can be drawn:

Multipath

Both the numerical and the analytical error modelling of the APL signal reception by a top-mounted aircraft antenna showed no multipath influence of creeping signals on code and carrier-phase tracking of a navigation receiver in an aircraft performing manoeuvres with moderate bank angles (<30°) according to standard instrument flight procedures.

With respect to the numerical error modelling, the possibility to calculate the differences of the absolute values of the correlation functions between a case where the aircraft body is absent and a fully identical case which includes the aircraft body was used to detect slight distortions of the correlation function due to additional signal rays (creeping multipath signals). The investigation with this technique showed no significant distortion of the correlation function for simulations of an aircraft with a cylindrical or box-shaped fuselage (see Figure 4-19, Figure 4-21 and Figure 4-22 in chapter 4.4) on final landing approach with a nominal glide path angle of approximately 3°. Aircraft bank angles up to 40° were simulated.

Concerning the analytical error modelling, the code and phase tracking error caused by creeping multipath signals was analytically quantified by using the Geometrical Theory of Diffraction for calculating signal amplitudes of diffracted navigation signals. For this purpose, different cylindrical fuselage sizes and bank angles of the aircraft were taken into account. The influence of the additional signal rays was shown by computing code and carrier-phase ranging error envelopes (see Figure 5-6 and Figure 5-7 in chapter 5.1.2). These diagrams illustrate the resulting maximum multipath error as a function of the bank angle of the aircraft. No code and carrier-phase ranging errors could be observed for bank angles up to 50°.

Signal Path Extension

The analytical derived signal path extension function (see equation (5-44) in chapter 5.2.1) has been analysed for a cylindrical and a box-shaped aircraft body (Figure 5-16 to Figure 5-21 in chapter 5.2.3) for aircraft attitudes that can occur in an aircraft landing approach scenario with a nominal glide path of approximately 3°. The analysed behaviour of the SPE function leads to worst case ranging error graphs (see blue graphs in Figure 5-22 and Figure 5-23 in chapter 5.2.3) for different aircraft sizes. The polynomial fits of these blue graphs are

$$\Delta_{\text{worst case, cyl}} = 0.0966 \cdot a \tag{6-1}$$

for cylindrical aircraft bodies, where a is the radius of the fuselage and

$$\Delta_{\text{worst case, box}} = 0.2245 \cdot w \tag{6-2}$$

for box-shaped aircraft bodies, where w is half of the fuselage width. The equations (6-1) and (6-2) can be used to determine the maximum ranging errors $\Delta_{\text{worst case, cyl}}$ and $\Delta_{\text{worst case, box}}$ due to

SPE expected for an aircraft on final landing approach. These errors occur, if the aircraft has a high pitch angle of 10°, a large bank angle of 30° and is far away from the APL.

Whereas a navigation receiver in an aircraft on a stable landing approach with small pitch angles of maximum 5° and small bank angles of maximum 10° does experience only small ranging errors (see red graphs in Figure 5-22 and Figure 5-23 in chapter 5.2.3). The polynomial fits of these red graphs are

$$\Delta_{\text{stable appraoch, cyl}} = 0.0137 \cdot a \tag{6-3}$$

and

$$\Delta_{\text{stable approach, box}} = 0.0613 \cdot w\,. \tag{6-4}$$

It should be mentioned that the ranging errors due to SPE for cylindrical aircraft bodies are much smaller than for box-shaped aircraft bodies (compare Figure 5-22 and Figure 5-23 in chapter 5.2.3).

If the APL ranging errors related to SPE shall be corrected, attitude data (pitch angle θ, bank angle φ and azimuth angle ψ) of the aircraft from an Inertial Navigation System (INS) are required. Additionally, the approximate position of the aircraft (determined without APL code- and carrier-phase measurements) and the position of the APL have to be known, to calculate the elevation β and the angle α (with the known azimuth angle ψ) according to Figure 5-8 and Figure 5-9 in chapter 5.2.1. These values and the known parameters a and w (see Figure 5-10 in chapter 5.2.1) are input values for the signal path extension function (see equation (5-44) in chapter 5.2.1). Finally, the computed SPE values have to be subtracted from the APL code- and carrier-phases to correct them and a position solution with the corrected APL measurements can be computed.

GNSS Signals

Similarly for the APL navigation signals, the signals from low-elevated GNSS satellites could experience a SPE during banking of the aircraft. The developed analytical error model for the SPE (see chapter 5.2.1) is also applicable for GNSS signals because it is independent from the signal structure. The term APL in chapter 5.2.1 has to be substituted by the respective GNSS satellite and the SPE function (see equation (5-44) in chapter 5.2.1) can be used to calculate the SPE values for navigation signals coming from GNSS satellites. These SPE values could be an additional consideration in the calculation of the navigation error budget for GNSS based approach systems when using navigation signals from low-elevated satellites for positioning.

7 References

Bauer, M., [1997], *Vermessung und Ortung mit Satelliten*, 4. Auflage 1997, Herbert Wichmann Verlag, Hüthig GmbH, Heidelberg, Germany, 1997.

Braasch, M. S., [1995], *Multipath Effects*, in B. W. Parkinson and J. R. Spilker Jr., *Global Positioning System: Theory and Applications Volume I*, Progress in Astronautics and Aeronautics, Volume 163, American Institute of Aeronautics and Astronautics, Washington, DC, USA, 1996, pp. 547-568.

Biberger, R. J., [2001], **V. Oehler**, **G. W. Hein, B. Eissfeller, T. Schueler**, *Pseudolite Signal Creeping on Conducting Surfaces*, Proceedings of ION-GPS 2001, The Institute of Navigation, Salt Lake City, Utah, USA, September 11-14, 2001, pp. 1238-1244.

Biberger, R. J., [2003], **T. Pany**, **A. Teuber**, **G. W. Hein, T. Schueler**, *A Code and Phase Error Model for Pseudolite Signal Reception on Top Mounted Aircraft Antennas*, Proceedings of GNSS 2003, European Navigation Conference, Graz, Austria, April 22-25, 2003.

Biberger, R. J., [2005], **M. Irsigler**, **A. Teuber**, **F. Kneißl**, **G. W. Hein**, *GNSS/Pseudolite Signal Propagation Errors on Aircraft Bodies*, Proceedings of GNSS 2005, European Navigation Conference, Munich, Germany, July 19-22, 2005.

Bryant, D. E., [1995], *Pseudolites*, in B. W. Parkinson and J. R. Spilker Jr., *Global Positioning System: Theory and Applications Volume II*, Progress in Astronautics and Aeronautics, Volume 164, American Institute of Aeronautics and Astronautics, Washington, DC, USA, 1996, pp. 51-79.

CST, [2002], *CST Microwave Studio Advanced Topics*, CST-Computer Simulation Technology, Version 4.

Cobb, H. S., [1999], **K. R. Zimmermann, D. G. Lawrence, G. M. Gutt, P. Y Montgomery, L. G. Leckie,** *Test Results for the IN500 Airport Pseudolite*, Proceedings of ION-GPS 1999, The Institute of Navigation, Nashville, Tennessee, USA, September 14-17, 1999.

Cosentino, R. J., [1996], **D. W. Diggle**, *Differential GPS*, in E. D. Kaplan, *Understanding GPS Principles and Applications*, Mobile Communications Series, Artech House, Boston, Massachusetts, 1996, pp 321-383.

Dohlus, M., [1992], *Ein Beitrag zur numerischen Berechnung elektromagnetischer Felder im Zeitbereich*, Dissertation, Fachbereich elektrische Nachrichtentechnik der Technischen Hochschule Darmstadt, Darmstadt, Germany, May 12, 1992.

GAO, [2005], *National Airspace System, FAA has made progress but continues to face challenges in acquiring major air traffic control systems*, Report to congressional requesters, United States Government Accountability Office, Washington, D.C., June, 2005.

Graeme, L. J., [1980], *Geometrical Theory of Diffraction for Electromagnetic Waves*, Revised Edition, The Institution of Electrical Engineers, London, England, 1980.

Hannah, B. M., [2001], *Modelling and Simulation of GPS Multipath Propagation*, Dissertation, The Cooperative Research Centre for Satellite Systems, Queensland University of Technology, Queensland, Australia, March 2001.

IntegriNautics, [1999], *IN500 Pseudolite User's manual*, Revision 1.2, December 6, 1999.

Jackson, J. D., [1975], *Classical Electrodynamics*, John Wiley & Sons, New York, USA, 1975.

Kiran, S., [2004], C. Bartone, *Verification and mitigation of the power-induced measurement errors for airport pseudolites in LAAS*, GPS Solutions, Volume 7, Number 4, Springer Berlin/Heidelberg, March 2004, pp 241-252.

Kong, J. A., [1986], *Electromagnetic Wave Theory*, John Wiley & Sons, New York, USA, 1986.

Kuchling, H, [1991], *Taschenbuch der Physik*, 13. korrigierte Auflage, Verlag Harri Deutsch, Thun und Frankfurt/Main, Germany, 1991.

Larrimore, C., [2005], http://www.ngs.noaa.gov/cgi-bin/query_cal_antennas.prl?Model=NOV&Antenna=NOV501,CR, March 10, 2005.

Olson, W., [2003], *Aviation Requirements for Navigation Systems*, Headquarters U.S. Air Force, http://www.eventmakeronline.com/dso/PDF/AFFSA-Olson.pdf, May 27, 2003.

Oppenheim, A. V., [1995], R. W. Schafer, *Zeitdiskrete Signalverarbeitung*, 2. neu übers. und überarb. Auflage, R. Oldenbourg Verlag GmbH, München, Germany, 1995.

Ott, B., [2001], U. Kälberer, E. Gross, V. Oehler, *Ranging and Integrity Pseudolite Augmentations*, Final Report, DLR Project: FKZ 50 NC 9601/2, Document Nr.: RIPA-AS-SP-T017, June 21, 2001.

Pany, T., [2002], *AP 4200 Detection and Tracking*, Technical Note, DLR Project: FKZ 50 NA 0003, Institut für Erdmessung und Navigation, Universität der Bundeswehr München, Neubiberg, Germany, July 26, 2002.

RTCA, [2001], *GNSS-Based Precision Approach Local Area Augmentation System (LAAS) Signal-in-Space Interface Control Document (ICD)*, RTCA/DO-246B, Prepared by SC-159, Washington, DC, USA, November 28, 2001.

Van Dierendonck, A. J., [1995], *GPS Receivers*, in B. W. Parkinson and J. R. Spilker Jr., *Global Positioning System: Theory and Applications Volume I*, Progress in Astronautics and Aeronautics, Volume 163, American Institute of Aeronautics and Astronautics, Washington, DC, USA, 1996, pp. 329-407.

Van Dierendonck, A. J., [1997], P. Fenton, C. Hegarty, *Proposed Airport Pseudolite Signal Specification for GPS Precision Approach Local Area Augmentation Systems*, Proceedings of ION-GPS 1997, The Institute of Navigation, Kansas City, Missouri, USA, September 16-19, 1997.

Van Dierendonck, A. J., [1998], *Report on APL Receiver Pseudorange Bias Investigations*, GPS Silicon Valley, California, USA, July 10, 1998.

Van Rienen, U., [2001], *Numerical Methods in Computational Electrodynamics*, Springer-Verlag Berlin Heidelberg, Germany, 2001.

Ward, P., [1996], *Satellite Signal Acquisition and Tracking*, in E. D. Kaplan, *Understanding GPS Principles and Applications*, Mobile Communications Series, Artech House, Boston, Massachusetts, 1996, pp 119-208.

Weiland, T., [1977], *A discretization method for the solution of Maxwell's equations for six-component fields*, International Journal of Electronics and Communication, Vol. 31, 1977, pp. 116-120.

Werner, W., [1997], B. Ott, *RIPA 2 (Ranging and Integrity Pseudolite Augmentations)*, Pseudolite Design-Dokument, Technical Note, Institut für Erdmessung und Navigation, Universität der Bundeswehr München, Neubiberg, Germany, November 3rd, 1997.

8 Appendix

8.1 Classical Electrodynamics

In this chapter we begin with the field equations and representations of the electromagnetic field which will be required in later developments.

Classical electrodynamics treats macroscopic electrical and magnetic phenomena [*van Rienen, 2001*]. These experimentally observed phenomena have been formally described by James Clerk Maxwell (1831-1879) in Maxwell’s equations. Maxwell’s equations build the axiomatic basis of electrodynamics, analogously to Newton’s axioms for mechanics. This section discusses Maxwell’s equations. Rather than aspiring to a comprehensive treatise, the PhD thesis contains the discussion of only those topics which are important for the main themes oft this thesis. Extensive treatment can be found in many textbooks, e.g., [*Kong, 1986*] or [*Jackson, 1975*].

8.1.1 Maxwell’s Equations and Constitutive Relations

Maxwell’s equations are the fundamental equations of electrodynamics. Time-varying Electric fields cause magnetic fields and vice versa. Therefore, one uses the term electromagnetic fields. Their macroscopic behaviour is described by Maxwell’s equations.

8.1.1.1 Maxwell’s Equations in Differential Form

In three-dimensional vector notation, Maxwell’s equations [*Kong, 1986*] for static media are

$$\operatorname{curl} \mathbf{E} = -\frac{\partial \mathbf{B}}{\partial t} \tag{8-1}$$

$$\operatorname{curl} \mathbf{H} = \frac{\partial \mathbf{D}}{\partial t} + \mathbf{J} \tag{8-2}$$

$$\operatorname{div} \mathbf{D} = \rho \tag{8-3}$$

$$\operatorname{div} \mathbf{B} = 0\,, \tag{8-4}$$

where **E, B, H, D, J,** and ρ (see Table 8-1) are functions of position **r** and time *t*.

Often the electric flux **D** is also referred to as the electric displacement and the magnetic flux **B** as the magnetic induction.

Field Quantity	Description	Unit
$\mathbf{E}(\mathbf{r},t)$	Electric Field Strength	[V/m]
$\mathbf{B}(\mathbf{r},t)$	Magnetic Flux	[T]=[Vs/m^2]
$\mathbf{H}(\mathbf{r},t)$	Magnetic Field Strength	[A/m]
$\mathbf{D}(\mathbf{r},t)$	Electric Flux	[C/m^2]=[As/m^2]
$\mathbf{J}(\mathbf{r},t)$	Electric Current Density	[A/m^2]
$\rho(\mathbf{r},t)$	Electric Charge Density	[C/m^3]=[As/m^3]

Table 8-1: Characteristic quantities of electromagnetic fields

Another field quantity is the electric current density **J** with unit [A/m^2] [*van Rienen, 2001*]

$$\mathbf{J} = \mathbf{J}_L + \mathbf{J}_E + \mathbf{J}_K = \kappa\mathbf{E} + \mathbf{J}_E + \delta \mathrm{grad}\rho\,. \tag{8-5}$$

$\mathbf{J}_\mathrm{L}$ is the conduction current density arising in materials with electric conductivity κ [1/Ωm] from the subsisting field strength. $\mathbf{J}_\mathrm{E}$ represents an impressed current density which is independent of all field forces. The convection current density $\mathbf{J}_\mathrm{K}$ is the density of a current of free electrical charges with the electric charge densities ρ [As/m^3]. The proportionality constant δ is called diffusion constant.

It is of interest how electromagnetic fields behave in the presence of media, whether the wave is diffracted, refracted, or scattered. Thus, material media has to be characterised by the so-called constitutive relations that can be classified according to the various properties of the media.

8.1.1.2 Constitutive Matrices

Constitutive relations in a general form can be written [*Kong, 1986*] as

$$\begin{bmatrix} c\mathbf{D} \\ \mathbf{H} \end{bmatrix} = \mathbf{C} \cdot \begin{bmatrix} \mathbf{E} \\ c\mathbf{B} \end{bmatrix}, \tag{8-6}$$

where c=2.99792458·10^{8}m/s is the velocity of light in vacuum and **C** is a 6×6 constitutive matrix

$$\mathbf{C} = \begin{bmatrix} \mathbf{P} & \mathbf{L} \\ \mathbf{M} & \mathbf{Q} \end{bmatrix} \tag{8-7}$$

which has the dimension of admittance. **P**, **Q**, **L** and **M** are all 3×3 matrices. Their elements are called constitutive parameters.

The constitutive matrix **C** may be a function of space-time coordinates, thermodynamical and continuum-mechanical variables, or electromagnetic field strengths. According to the functional dependence of **C**, the various media can be classified as inhomogeneous if **C** is a function of space coordinates, nonstationary if **C** is a function of time, time-dispersive if **C** is a function of spatial derivatives, nonlinear if **C** is a function of the electromagnetic field, and so forth. In the general case **C** may be a function of integral-differential operators and coupled to fundamental equations of other physical disciplines.

8.1.1.3 Isotropic, Anisotropic, and Bianisotropic Media

In the definition of the constitutive relations, the constitutive matrices **L** and **M** relate electric and magnetic fields [*Kong, 1986*]. When **L** and **M** are not identically zero, the medium is bi-anisotropic. When there is no coupling between electric and magnetic fields, **L**=**M**=0 and the medium is anisotropic. For an anisotropic medium, if

$$\mathbf{P} = c\varepsilon \begin{bmatrix} 1 & 0 & 0 \\ 0 & 1 & 0 \\ 0 & 0 & 1 \end{bmatrix} \tag{8-8}$$

and

$$\mathbf{Q} = \frac{1}{c\mu} \begin{bmatrix} 1 & 0 & 0 \\ 0 & 1 & 0 \\ 0 & 0 & 1 \end{bmatrix} \tag{8-9}$$

the medium is isotropic.

The constitutive relations for an isotropic medium can be written simply as

$$\mathbf{D} = \varepsilon \mathbf{E}, \tag{8-10}$$

where ε is the permittivity and

$$\mathbf{B} = \mu \mathbf{H}, \tag{8-11}$$

where μ is the permeability.

Thus, the field vector **E** is parallel to **D** and the field vector **H** is parallel to **B**. In free space void of any matter, $\mu = \mu_0$ and $\varepsilon = \varepsilon_0$,

$$\mu_0 = 4\pi \cdot 10^{-7} \qquad \text{[H/m]}$$

$$\varepsilon_0 = 8.85418781762 \cdot 10^{-12} \qquad \text{[F/m]}.$$

Inside a material medium, the permittivity ε is determined by the electrical properties of the medium and the permeability μ by the magnetic properties of the medium.

A dielectric material can be described by a free-space part and a part that is due to the material alone. The material part can be characterised by a polarisation vector **U** such that

$$\mathbf{D} = \varepsilon_0 \mathbf{E} + \mathbf{U} \tag{8-12}$$

The polarisation **U** symbolises the electric dipole moment per unit volume of the dielectrical material. In the presence of an external electric field, the polarisation vector may be caused by induced dipole moments, alignment of the permanent dipole moments of the medium, or migration of ionic charges.

A magnetic material can also be described by a free-space part and a part characterised by a magnetisation vector **W** such that

$$\mathbf{B} = \mu_0 \mathbf{H} + \mu_0 \mathbf{W} \tag{8-13}$$

A medium is diamagnetic if $\mu \le \mu_0$, paramagnetic if $\mu \ge \mu_0$. Diamagnetism is caused by induced magnetic moments that tend to oppose the externally applied magnetic field. Paramagnetism is due to alignment of magnetic moments.

In homogeneously polarised materials [*van Rienen, 2001*]

$$\mathbf{U} = \varepsilon_0 \chi_e \mathbf{E}\,, \tag{8-14}$$

where χ_e is the dielectric susceptibility. For the linear materials,

$$\mathbf{D} = \varepsilon_0 \left(1 + \chi_e\right) \mathbf{E} \tag{8-15}$$

and

$$\varepsilon_r \equiv 1 + \chi_e \tag{8-16}$$

is referred to as relative permittivity.

In diamagnetic media, the relation

$$\mathbf{W} = \chi_m \mathbf{H} \tag{8-17}$$

holds, with the magnetic susceptibility χ_m. In magnetic linear materials, we can write

$$\mathbf{B} = \mu_0 \left(1 + \chi_m\right) \mathbf{H} \tag{8-18}$$

and

$$\mu_r \equiv 1 + \chi_m \tag{8-19}$$

is called relative permeability.

In general, the permittivity

$$\varepsilon = \varepsilon_r \varepsilon_0 \tag{8-20}$$

and the permeability

$$\mu = \mu_r \mu_0 \tag{8-21}$$

are tensors depending on time, space, and field. They are scalars in linear isotropic media. In vacuum, they are constant (see above) satisfying the condition

$$c = \frac{1}{\sqrt{\varepsilon_0 \mu_0}}\,. \tag{8-22}$$

8.1.1.4 Maxwell's Equations in Integral Form

The Maxwell equations have been written in differential form (8-1)-(8-4). They must be supplemented with boundary conditions and initial conditions [*van Rienen, 2001*]. The boundary conditions can be derived from the integral form of Maxwell's equations. Let A be a 2-

dimensional domain with boundary ∂A. Upon integrating (8-1) and (8-2) over A, using Stokes' theorem, the first two Maxwell's equations can be written as

$$\oint_{\partial A} \mathbf{E} \cdot d\mathbf{s} = -\int_A \frac{\partial \mathbf{B}}{\partial t} \cdot d\mathbf{A} \tag{8-23}$$

$$\oint_{\partial A} \mathbf{H} \cdot d\mathbf{s} = \int_A \left(\frac{\partial \mathbf{D}}{\partial t} + \mathbf{J} \right) \cdot d\mathbf{A} \,. \tag{8-24}$$

Now let V be a 3-dimensional domain enclosed by the surface ∂V. Integrating (8-2) and (8-3) over V and using Gauß' theorem, the third and fourth Maxwell's equations can be written as

$$\oint_{\partial V} \mathbf{D} \cdot d\mathbf{A} = \int_V \rho \cdot dV \tag{8-25}$$

$$\oint_{\partial V} \mathbf{B} \cdot d\mathbf{A} = 0 \,. \tag{8-26}$$

The continuity equation and the theorem on the conservation of charges

$$\operatorname{div} \mathbf{J} + \frac{\partial \rho}{\partial t} = 0 \tag{8-27}$$

$$\oint_{\partial V} \mathbf{J} \cdot d\mathbf{A} + \frac{\partial}{\partial t} \int_{\mathrm{V}} \rho \cdot dV = 0 \tag{8-28}$$

follow from Maxwell's equations. To get the continuity equation, the operator div has to be applied to both sides of (8-2) and it has to be taken into account that

$$\operatorname{div} \operatorname{curl} \mathbf{H} \equiv 0 \,, \tag{8-29}$$

the order in the mixed derivative with respect to space and time has to be interchanged, and (8-3) has to be used. The conservation law for charges follows from the continuity equation by integration and Gauß' theorem. This law states that the total charge in a volume decreases if and only if the corresponding current flows out at the same time.

The solution of Maxwell's equations depends on the problem. The different permissible assumptions lead to a whole series of different types of differential equations and hence to different solution arrangements.

8.1.2 General Time-Dependent Fields and Electromagnetic Waves

In case of fast varying fields where neither the time variation of the magnetic induction $\partial \mathbf{B}/\partial t$ nor that of the density of displacement current $\partial \mathbf{D}/\partial t$ may be neglected, the set of full Maxwell's equations has to be solved [*van Rienen, 2001*]. Maxwell's equations state that the electric and magnetic fields are interrelated. The time-dependent change of the fields propagates with finite velocity through space. It is called electromagnetic wave.

For fields with general time-dependence where no terms in Maxwell's equations may be neglected, it is convenient to rewrite Maxwell's equations as an initial-boundary value problem for a system of differential equations. For this purpose, the field quantities **E** and **H** first have to be normalised appropriately with the normalisations

$$\mathbf{E} = \sqrt{Z_0}\,\mathbf{E}' \tag{8-30}$$

$$\mathbf{H} = \sqrt{Y_0}\,\mathbf{H}' \tag{8-31}$$

with the square root of the wave impedance

$$\sqrt{Z_0} = \sqrt{\frac{\mu_0}{\varepsilon_0}} \tag{8-32}$$

and the admittance

$$Y_0 = \frac{1}{Z_0}\,. \tag{8-33}$$

This normalisations results in **E**' and **H**' having the same dimension. Introducing an unknown function

$$\mathbf{u}(t) \equiv \begin{pmatrix} \mathbf{E}' \\ \mathbf{H}' \end{pmatrix} \tag{8-34}$$

and an excitation function

$$\mathbf{q}(t) \equiv \begin{pmatrix} -\dfrac{1}{\varepsilon}\rho\mathbf{v} \\ 0 \end{pmatrix} \tag{8-35}$$

for the case of moving charges with velocity **v**, the first two Maxwell's equations can be written as

$$\dot{\mathbf{u}}(t) = \mathbf{L}\mathbf{u}(t) + \mathbf{q}(t)\,, \tag{8-36}$$

where

$$\mathbf{L} \equiv \begin{pmatrix} -\dfrac{\kappa}{\varepsilon} & \dfrac{1}{\varepsilon_r}\,\mathrm{curl}\,\dfrac{1}{\mu_0} \\ -\dfrac{1}{\mu_r}\,\mathrm{curl}\,\dfrac{1}{\varepsilon_0} & 0 \end{pmatrix}. \tag{8-37}$$

Adding the initial conditions

$$\mathbf{u}(t_0) \equiv \begin{pmatrix} \mathbf{E}_0^{'} \\ \mathbf{H}_0^{'} \end{pmatrix}, \tag{8-38}$$

the Maxwell's equations result in an initial-value problem. Its formal solution is given by

$$\mathbf{u}(t) = \mathbf{u}(t_0) + \int_{t_0}^{t} \left(\mathbf{L}\mathbf{u}(t) + \mathbf{q}(t) \right) dt \,. \tag{8-39}$$

8.2 Finite Integration Technique

This discretisation method is chosen to solve Maxwell's equations. It presents a discretisation consistent with Maxwell's equations, i.e., the resulting discrete solutions reflect the analytical properties of the continuous solutions [*van Rienen, 2001*]. The Finite Integration Technique (FIT) can best be described as a finite volume method.

8.2.1 FIT Discretisation of Maxwell's Equations

The Finite Integration Technique (FIT) [*Weiland, 1977*] has been developed specifically for the solution of Maxwell's equations. The goal of this development was the ability to solve numerically the complete system of Maxwell's equations in full generality [*van Rienen, 2001*]. The Finite Integration Technique presents a transformation of Maxwell's equations in integral form

$$\oint_{\partial A} \mathbf{E} \cdot d\mathbf{s} = -\int_{A} \frac{\partial \mathbf{B}}{\partial t} \cdot d\mathbf{A} \tag{8-23}$$

$$\oint_{\partial A} \mathbf{H} \cdot d\mathbf{s} = \int_{A} \left(\frac{\partial \mathbf{D}}{\partial t} + \mathbf{J} \right) \cdot d\mathbf{A} \tag{8-24}$$

$$\oint_{\partial V} \mathbf{D} \cdot d\mathbf{A} = \int_{V} \rho \cdot dV \tag{8-25}$$

$$\oint_{\partial V} \mathbf{B} \cdot d\mathbf{A} = 0 \tag{8-26}$$

onto a grid pair (G, $\tilde{G}$).

The FIT makes only some usual idealisations concerning the materials: The materials of the given objects have to be piecewise linear, homogeneous, and isotropic so that the subdomains with constant material parameters (ε, μ, κ) are at least as big as the elementary volumes used.

8.2.2 FIT Grid

The discretisation of Maxwell's equations, i.e., the field computation in a finite number of discrete points, gives a decomposition of the solution space into grid cells [*van Rienen, 2001*]. The first step towards that goal is to define a finite volume Ω, the calculation domain. Ω is covered with a grid *G*. As an example, a simple Cartesian coordinate system is considered. It has to be stressed at this point, however, that a FIT grid *G* is defined in much more generality and that its definition also includes non-coordinate grids as well as non-orthogonal grids.

The grid is composed of the so-called elementary volumes V_i or FIT cells. Each FIT cell is filled with a homogeneous material. The intersection of two elementary volumes is an elementary area A_i, the intersection of two elementary areas an elementary line L_i, on which the unknown state variables are allocated.

In the next step, the first of Maxwell's equations (8-23) will be transferred to the FIT grid G. An elementary volume V_i for the simplest case is shown in Figure 8-1. The left-hand side of the induction law (8-23) is treated as follows: Introducing the electric (grid-) voltage e_i

$$e_i = \int_{L_i} \mathbf{E} \cdot d\mathbf{s} \tag{8-40}$$

along the elementary line L_i as a state variable on the grid G, the contour integral

$$\oint_{\partial A_m} \mathbf{E} \cdot d\mathbf{s} \tag{8-41}$$

reduces to the difference

$$e_i + e_j - e_k - e_l \,. \tag{8-42}$$

The surface integral

$$-\frac{\partial}{\partial t} \int_A \mathbf{B} \cdot d\mathbf{A} \tag{8-43}$$

on the right-hand side of equation (8-23) has to be transferred appropriately to the grid G. The elementary area A_m has already been chosen as the area of integration. Therefore, the direction of $d\mathbf{A}$ is already determined. Analogously, the magnetic (grid) flux b_m normal to the elementary area A_m is assigned as a state variable to each elementary area A_m:

$$b_m = \int_{A_m} \mathbf{B} \cdot d\mathbf{A} \,. \tag{8-44}$$

The induction law is then given by

$$e_i + e_j - e_k - e_l = -\frac{\partial}{\partial t} b_m \,. \tag{8-45}$$

After appropriate numbering of the points of the grid, the state variables e_i and b_i, can be stored in vectors **e** and **b**. The factors {-1, 0, 1} are stored in a matrix **C** which reflects the topology of the grid. Thus, the discrete form of the induction law is

$$\underbrace{\begin{pmatrix} & & & \vdots & & & \\ 1 & \cdots & 1 & \cdots & -1 & \cdots & -1 \\ & & & \vdots & & & \end{pmatrix}}_{\mathbf{C}} \underbrace{\begin{pmatrix} e_i \\ \vdots \\ e_j \\ \vdots \\ e_k \\ \vdots \\ e_l \end{pmatrix}}_{\mathbf{e}} = -\frac{\partial}{\partial t} \underbrace{\begin{pmatrix} \vdots \\ b_m \\ \vdots \end{pmatrix}}_{\mathbf{b}}, \tag{8-46}$$

or in general

$$\mathbf{Ce} = -\frac{\partial}{\partial t}\mathbf{b}. \tag{8-47}$$

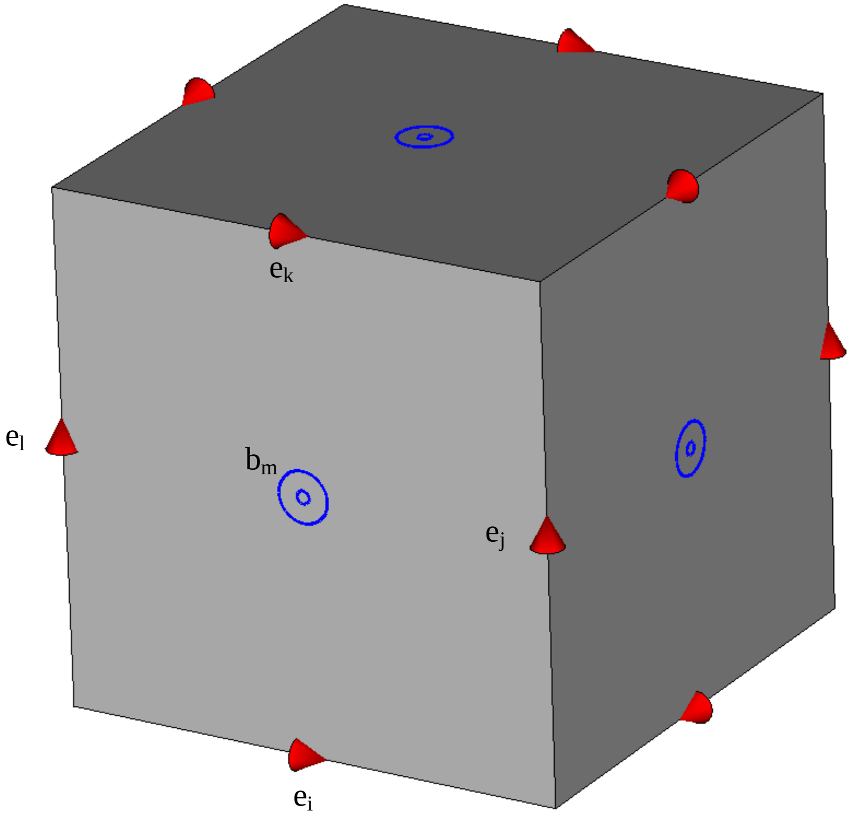

Figure 8-1: Elementary volume of a Cartesian FIT grid *G*

Next, the fourth of Maxwell's equations (8-26) is transferred to the grid G. Again, the total integral can be written as the sum of integrals over the components. Consequently, the surface integrals are over the elementary volumes V_i, and the magnetic fluxes b_i are used again. Figure 8-2 shows the allocation of the magnetic flux on V_i. This yields the difference equation

$$b_m + b_n + b_o - b_p - b_q - b_r = 0. \tag{8-48}$$

Introducing a matrix **S** with elements {-1, 0, 1} corresponding to the topology of the grid, the discrete form of the fourth Maxwellian equation is

$$\underbrace{\begin{pmatrix} & & & & \vdots & & & & \\ \cdots & 1 & 1 & 1 & -1 & -1 & -1 & \cdots \\ & & & & \vdots & & & & \end{pmatrix}}_{\mathrm{S}} \underbrace{\begin{pmatrix} \vdots \\ b_m \\ b_n \\ b_o \\ b_p \\ b_q \\ b_r \\ \vdots \end{pmatrix}}_{\mathbf{b}} = 0\,, \tag{8-49}$$

or in general

$$\mathbf{Sb} = 0\,. \tag{8-50}$$

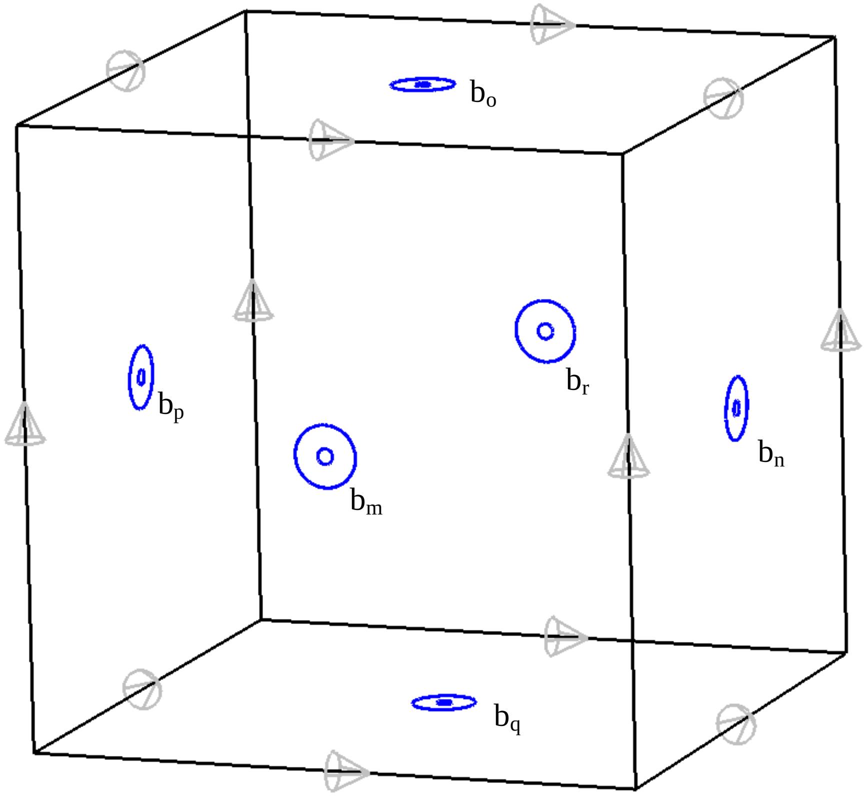

Figure 8-2: Elementary volume of a Cartesian FIT grid *G* with magnetic grid flux

It remains to transfer the second and third Maxwell's equations. This will be completely analogous to the transfer of the first and fourth Maxwell's equations. For that, the so-called dual grid $\tilde{G}$ is introduced. For a Cartesian grid, it equals the grid G shifted by half a cell length (see Figure 8-3).

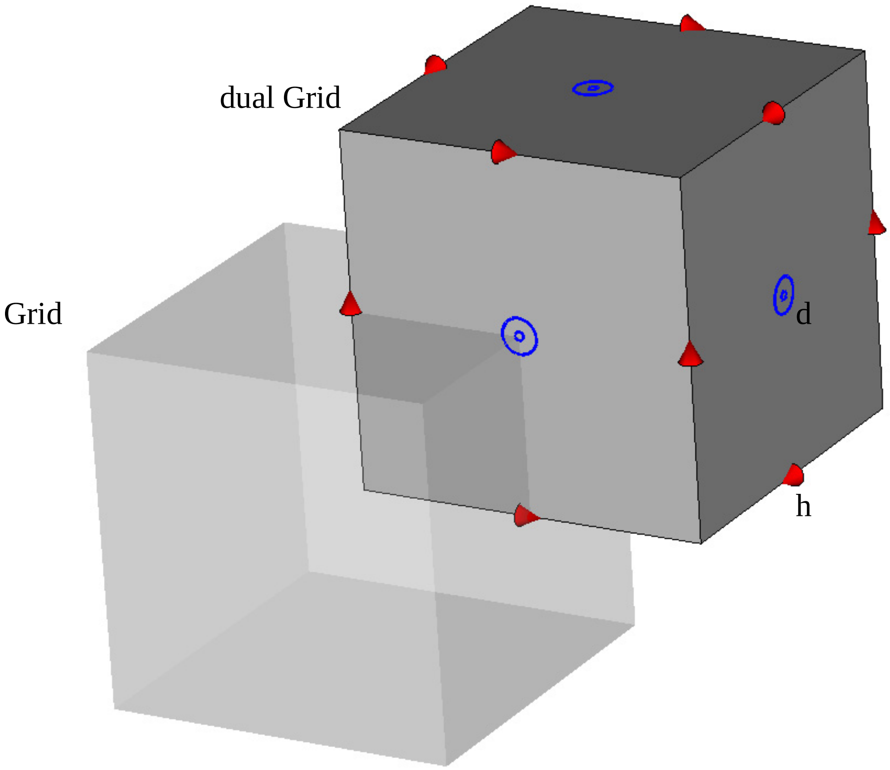

Figure 8-3: Elementary volume of the dual grid $\tilde{G}$ for the Cartesian FIT grid G

The state variables h and d are introduced analogously to e and b. The magnetic voltage h_i is assigned as a state variable to each dual elementary line $\tilde{L}_i$:

$$h_i = \int_{\tilde{L}_i} \mathbf{H} \cdot d\mathbf{s}\,, \tag{8-51}$$

and the electric flux d_i normal to the dual grid surface $\tilde{A}_i$ is assigned as a state variable to each dual elementary area $\tilde{A}_i$:

$$d_i = \int_{\tilde{A}_i} \mathbf{D} \cdot d\mathbf{A}\,. \tag{8-52}$$

Furthermore, the total electric current j_i normal to the dual grid surface $\tilde{A}_i$ is assigned as a state variable to each dual elementary area $\tilde{A}_i$:

$$j_i = \int_{\tilde{A}_i} \mathbf{J}\cdot d\mathbf{A}\,. \tag{8-53}$$

The discrete charges q_i (allocated on the grid points P_i on G) are assigned as state variables to each dual elementary volume $\tilde{V}_i$:

$$q_i = \int_{\tilde{V}_i} \rho\cdot dV\,. \tag{8-54}$$

The values of the state variables are stored in topological matrices $\tilde{\mathbf{C}}$ and $\tilde{\mathbf{S}}$ analogous to **C** and **S**. Thus, the discrete form of Ampere's law is

$$\tilde{\mathbf{C}}\mathbf{h} = \frac{\partial}{\partial t}\mathbf{d} + \mathbf{j} \tag{8-55}$$

and the third Maxwell's equation is

$$\tilde{\mathbf{S}}\mathbf{d} = \mathbf{q}\,. \tag{8-56}$$

8.2.3 Maxwell Grid Equations

To summarise the above, the Maxwell grid equations will be formally defined. It should be emphasised that no approximations have been made so far. Only when the material equations are transferred to the grid space, the FIT will require some approximations [*van Rienen, 2001*].

The following discretisation method for Maxwell's equations is called Finite Integration Technique (FIT).

1. A FIT grid G is chosen for the given solution domain. The grid points are assumed to be numbered appropriately. The following state variables are introduced:

$e_i = \int_{L_i} \mathbf{E}\cdot d\mathbf{s}$	electric (grid)-voltage	(8-40)
$b_i = \int_{A_i} \mathbf{B}\cdot d\mathbf{A}$	magnetic (grid)-flux	(8-57)
$h_i = \int_{\tilde{L}_i} \mathbf{H}\cdot d\mathbf{s}$	magnetic (grid)-voltage	(8-51)
$d_i = \int_{\tilde{A}_i} \mathbf{D}\cdot d\mathbf{A}$	electric (grid)-flux	(8-52)
$j_i = \int_{\tilde{A}_i} \mathbf{J}\cdot d\mathbf{A}$	electric total current	(8-53)
$q_i = \int_{\tilde{V}_i} \rho\cdot dV$	discrete (grid)-charges (allocated in P_i on G).	(8-54)

2. The discrete analogue to Maxwell's equations is given by the following system of linear equations:

$$\mathbf{Ce} = -\frac{\partial}{\partial t}\mathbf{b} \qquad (8\text{-}47)$$

$$\mathbf{Sb} = 0 \qquad (8\text{-}50)$$

$$\tilde{\mathbf{C}}\mathbf{h} = \frac{\partial}{\partial t}\mathbf{d} + \mathbf{j} \qquad (8\text{-}55)$$

$$\tilde{\mathbf{S}}\mathbf{d} = \mathbf{q}\,. \qquad (8\text{-}56)$$

Because of its consistency and generality, this system is referred to as Maxwell grid equations.

3. The operators **C**, $\tilde{\mathbf{C}}$, **S** and $\tilde{\mathbf{S}}$ can be interpreted as follows:

$$\mathbf{C}, \tilde{\mathbf{C}} \quad \equiv \text{curl}$$

$$\mathbf{S}, \tilde{\mathbf{S}} \quad \equiv \text{divergence}$$

$$-\mathbf{S}^{\mathbf{T}}, -\tilde{\mathbf{S}}^{\mathbf{T}} \quad \equiv \text{gradient.}$$

Therefore, they are called the discrete curl operator, the discrete divergence operator and the discrete gradient operator.

8.2.4 Approximation of Material Properties

Until now, no approximations have been used at all. They will be necessary after the transfer of the material equations to the grid space [*van Rienen, 2001*].

The state variables d_i and e_i (b_i and h_i, respectively) are each allocated at the same points. There is an analogue of the material equations relating them to each other. In order to find that analogue of the material equations, the grid flux is divided by the grid voltage. The ratios d_i/e_i and b_i/h_i (j_i/e_i respectively) then will be approximated by averaging the corresponding material parameters. The averaged quantities are then combined in the so-called material matrices $\mathbf{D}_\varepsilon$, $\tilde{\mathbf{D}}_\mu$ and $\mathbf{D}_\kappa$. Thus, the following transfer of the electromagnetic material equations to the grid space results:

$$\mathbf{D} = \varepsilon \mathbf{E} \rightarrow \mathbf{d} = \mathbf{D}_\varepsilon \mathbf{e} \qquad (8\text{-}58)$$

$$\mathbf{B} = \mu \mathbf{H} \rightarrow \mathbf{b} = \tilde{\mathbf{D}}_\mu \mathbf{h} \qquad (8\text{-}59)$$

$$\mathbf{J}_L = \kappa \mathbf{E} \rightarrow \mathbf{j}_l = \mathbf{D}_\kappa \mathbf{e}\,. \qquad (8\text{-}60)$$

8.2.5 Discretisation of Integrals

The state variables are defined as surface or line integrals over elementary areas or elementary lines [*van Rienen, 2001*]. One needs a one-to-one correspondence between the discrete field quantities and the state variables. To obtain such a correspondence, the definition of an integral as a limit is used. The simplest numerical integration over an interval uses one supporting point in the middle of the interval:

$$\int_{x_0}^{x_0+\Delta} \mathrm{f}(x)dx = \Delta \cdot \mathrm{f}(x_0 + \frac{\Delta}{2}) + O(\Delta^3)\,. \tag{8-61}$$

The simplest integration formula for a surface integral is

$$\int_{x_0}^{x_0+\Delta}\int_{y_0}^{y_0+\Delta} \mathrm{f}(x,y)dxdy = \Delta^2 \cdot \mathrm{f}(x_0 + \frac{\Delta}{2}, y_0 + \frac{\Delta}{2}) + O(\Delta^4)\,. \tag{8-62}$$

These approximation formulas are used in the Finite Integration Technique. The field quantities are allocated on the grid pair $(G, \tilde{G})$ in the same way as the state variables. The remainder in the integral formulas has order $O(\Delta^2)$.

8.2.6 General Time-Dependent Fields and Electromagnetic Waves

For general time-dependent fields it is recommended to use the so-called mean-value state variables in Table 8-2 [*Dohlus, 1992*] for the formulation of the discrete initial value problem rather than the integral state variables. The mean-value state variables and the integral state variables are connected via the operators $\mathbf{D}_s$, $\tilde{\mathbf{D}}_s$, $\mathbf{D}_A$ and $\tilde{\mathbf{D}}_A$ for the line (surface) integrals on the primary (dual) grid [*van Rienen, 2001*].

$E_i d_{si} \equiv \int_{L_i} \mathbf{E} \cdot d\mathbf{s} = E_i \int_{L_i} ds = e_i$	$\mathbf{e} = [e_i]$	$\mathbf{D}_s = [d_{si}\delta_{ji}]$
$B_i d_{Ai} \equiv \int_{A_i} \mathbf{B} \cdot d\mathbf{A} = B_i \int_{A_i} t(\mathbf{s}) \cdot dA = b_i$	$\mathbf{b} = [b_i]$	$\mathbf{D}_A = [d_{Ai}\delta_{ji}]$
$H_i \tilde{d}_{si} \equiv \int_{\tilde{L}_i} \mathbf{H} \cdot d\mathbf{s} = H_i \int_{\tilde{L}_i} ds = h_i$	$\mathbf{h} = [h_i]$	$\tilde{\mathbf{D}}_s = [\tilde{d}_{si}\delta_{ji}]$
$D_i \tilde{d}_{Ai} \equiv \int_{\tilde{A}_i} \mathbf{D} \cdot d\mathbf{A} = D_i \int_{\tilde{A}_i} t(\mathbf{s}) \cdot dA = d_i$	$\mathbf{d} = [d_i]$	$\tilde{\mathbf{D}}_A = [\tilde{d}_{Ai}\delta_{ji}]$
$J_i \tilde{d}_{Ai} \equiv \int_{\tilde{A}_i} \mathbf{J} \cdot d\mathbf{A} = J_i \int_{\tilde{A}_i} t(\mathbf{s}) \cdot dA = j_i$	$\mathbf{j} = [j_i]$	
with $t(\mathbf{s}) = \begin{cases} 1 & \text{if } \varepsilon, \mu, \kappa \text{ finite} \\ 0 & \text{else} \end{cases}$		

Table 8-2: Definition of the mean-value state variables [*Dohlus, 1992*]

Let **e**'=[**E'**] be the vector of all mean values of the normalised electric field along the grid lines and **h**'=[**H'**] the corresponding vector for the magnetic field (see appendix 8.1.2), then

$$\mathbf{u}(t) \equiv \begin{pmatrix} \mathbf{E}' \\ \mathbf{H}' \end{pmatrix} \Leftrightarrow \mathbf{u} \equiv \begin{pmatrix} \mathbf{e}' \\ \mathbf{h}' \end{pmatrix}. \tag{8-63}$$

The operator **L** has the following discrete analogue

$$\mathbf{L} \equiv \begin{pmatrix} -\dfrac{\kappa}{\varepsilon} & \dfrac{1}{\varepsilon_r}\mathrm{curl}\dfrac{1}{\mu_0} \\ -\dfrac{1}{\mu_r}\mathrm{curl}\dfrac{1}{\varepsilon_0} & 0 \end{pmatrix}$$

$$\Leftrightarrow \mathbf{A} \equiv \begin{pmatrix} -\mathbf{D}_\kappa \mathbf{D}_\varepsilon^{-1} & \mathbf{D}_{\varepsilon_r}^{-1}\tilde{\mathbf{D}}_A^{-1}\tilde{\mathbf{C}}\tilde{\mathbf{D}}_s\tilde{\mathbf{D}}_{\mu_0}^{-1} \\ -\tilde{\mathbf{D}}_{\mu_r}^{-1}\mathbf{D}_A^{-1}\mathbf{C}\mathbf{D}_s\mathbf{D}_{\varepsilon_0}^{-1} & 0 \end{pmatrix} \tag{8-64}$$

and the excitation function is

$$\mathbf{q}(t) \equiv \begin{pmatrix} -\mathbf{D}_\varepsilon^{-1}\rho\mathbf{v} \\ 0 \end{pmatrix}. \tag{8-65}$$

The initial value problem can be solved by a one-step or multi-step algorithm. Detailed information can be found in the textbook [*Dohlus, 1992*] which is devoted specifically to the initial value problem for high frequency fields described above.

8.3 Pulsing of APL Signals

8.3.1 General Description

A pulser is part of the transmit unit subsystem in an APL. Other devices included in the transmit unit are the PL signal generator and the transmit antenna. A diagram of the transmit unit can be observed in Figure 8-4.

The PL signal generator generates a WB code modulated with navigation data. A carrier signal is modulated with this code and navigation data to produce the required spread spectrum signal. The resulting RF signal is then sent to the pulser. The PL signal generator also provides a code chip clock for the pulser unit.

The pulser is a HF and modular device. It has to maintain two functions: to provide the appropriate RF output power level depending on the actual pulsing duty cycle (this function can be also maintained by an amplifier after the pulser) and to generate the pulsing, i.e. to generate a pulse sequence and then to combine this pulse sequence with the code.

Finally, the antenna transmits the signal result from this combination.

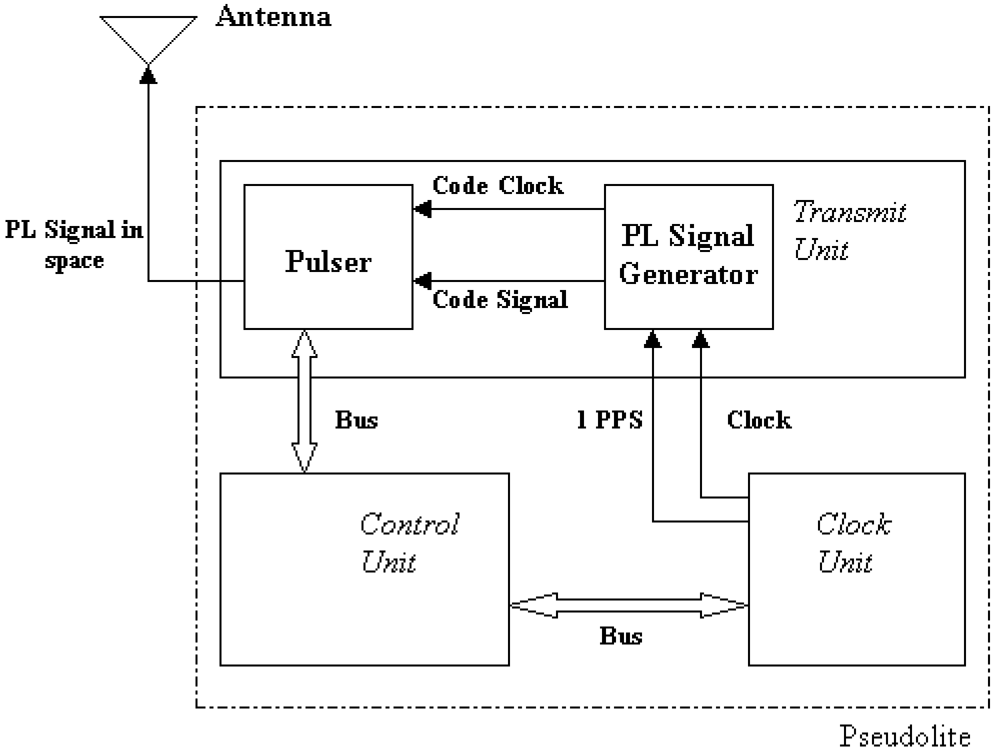

Figure 8-4: PL hardware structure [*Ott et al., 2001*]

8.3.2 Pulser Design

A pulser consists mainly of a Pulse Sequence Generator (PSG) and a Pulser RF Unit (PRU) (HF switch). As it can be seen in Figure 8-5, the pulser has the following inputs and outputs:

Inputs:

- The code to be transmitted
- Synchronisation signals (Code clock, PPS)

Outputs:

- The transmitted pseudolite signal
- Monitoring signals

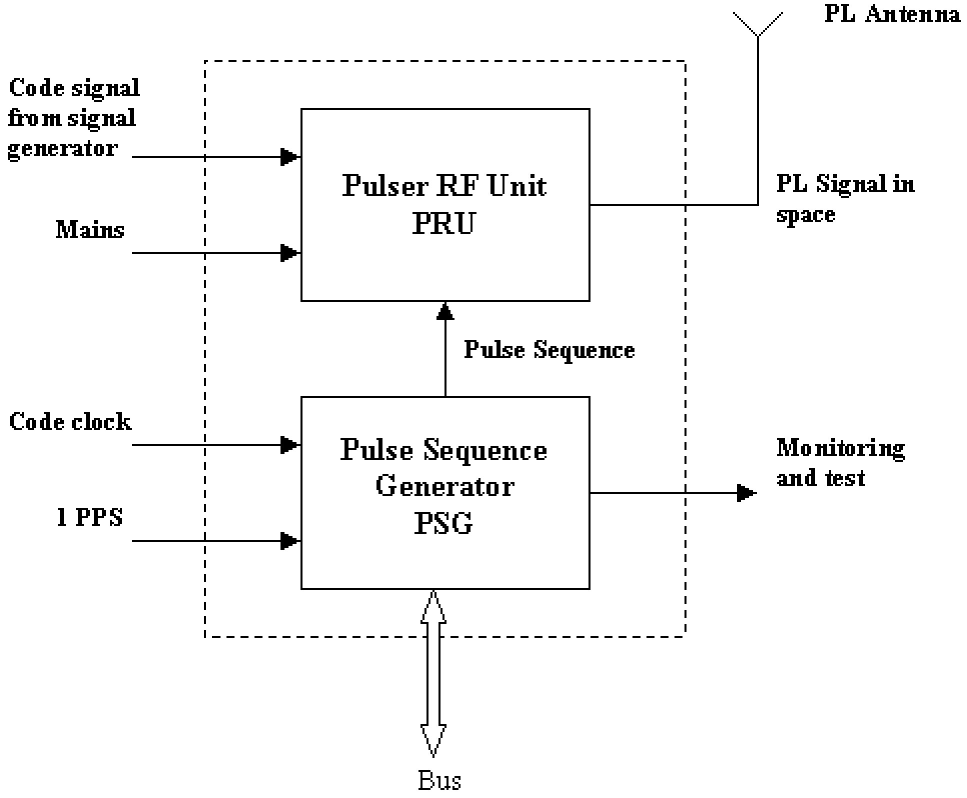

Figure 8-5: Pulser inputs and outputs [*Ott et al., 2001*]

8.3.3 Pulse Sequence Generator

The PSG is used to provide control of the PRU and generates the pulse sequence output signal that usually has a randomised pattern (but it can have also a fixed pattern) which is sent to the PRU.

As it can be observed in Figure 8-4 and Figure 8-5, this device receives a code chip clock from the pseudolite signal generator to allow synchronisation with the pulsing. It can also have an external synchronisation input, an interface to monitor the generated signals and to modify parameters of the pulse and pulse sequence.

The pulses are generated coherently to the chip clock of the lowest frequency spreading code in use. A pseudorandom scheme is usually applied as a pulse pattern but also a fixed scheme can be applied. The pseudorandom scheme is used to prevent the user receiver from locking on to the pulse pattern. This pseudorandom sequence will result in a random pulse repetition rate. The average pulse repetition rate should be sufficiently high, so that the pseudolite signal will appear to be continuous in the user's receiver post correlation signal processing, while appearing to be pulsed during wideband processing prior to correlation.

When using multiple pseudolites and to avoid pulse collision a delay of the pulsing scheme of the pseudolites with respect to each other can be implemented. Another option to avoid pulse collision is to use different random pulse patterns for each pseudolite.

8.3.3.1 RTCA Pulse Pattern

This pulse mode is specified in [*RTCA, 2001*]. It is a pseudorandom sequence of pulses generated by a feedback shift register, similar to the way the WB code is generated. Each pulse is 140 WB chips wide.

8.3.3.2 RTCM Pulse Pattern

The RTCM pulsing is based on dividing 1 ms into either 11 or 33 even time-slots and then start pulsing during a particular time-slot specified by either a pseudorandom sequence or a fixed pattern [*IntegriNautics, 1999*].

8.3.3.3 Fixed Pulse Patterns

The use of not-randomised pulse patterns can be also taken into account. In a fixed pulse pattern, the pulses are generated in specified periods of time. Static and sweep are examples of fixed pulse patterns [*IntegriNautics, 1999*].

In static pulse patterns, the pulse occurs at a fixed period.

In sweep pulse patterns, pulses occur at incrementally greater offsets from the trigger. The offset returns to zero when it reaches a full epoch delay.

8.3.3.4 Average Pulse Duty Cycle

The average pulse duty cycle PDC_{av} can be defined as the number of pulses per second (n_{pulse}) multiplied by the chips per pulse ($n_{chips/pulse}$) and divided by the total number of chips per second ($n_{chips/sec}$):

$$PDC_{av} = \frac{n_{pulse} \cdot n_{chips/pulse}}{n_{chips/\mathrm{s}}} . \tag{8-66}$$

8.3.4 Pulser RF Unit

The Pulser RF Unit's main task is to control and process the RF input signal by means of the pulse sequence. The RF input signal is provided by the pseudolite signal generator. The pulse sequence is provided by the PSG and is used to control the signal flow through the PRU. When the pulse sequence is in the on state, the RF input signal is amplified to an appropriate power level. In the off state, the RF output is isolated from the RF input.

The PRU's output is the PL transmitted signal.

8.4 Modelling the APL RF Signal

Since the processing of the full APL RF signal with an electromagnetic simulator is too complex and time consuming, a special approach will be presented to reconstruct the full IF signal from only one chip of the RF signal [*Pany, 2002*].

8.4.1 Signal Generation

We assume that the signal emitter (APL) has a fixed position. The emitted signal has the form

$$s_e(t) = Ac_e(f_C t)\cos(2\pi f_P t). \tag{8-67}$$

$s_e(t)$	emitted signal in the I-channel, Q-channel and navigation data are not considered
A	signal amplitude
$c_e(f_C t)$	emitted code as a function of code-phase
$f_C = 1/T_C$	chipping rate
T_C	chip length in [s]
f_P	frequency of the carrier-phase [1/s]
c	speed of light in [m/s]
t	time in [s]

Table 8-3: Characteristic quantities of the emitted signal

8.4.2 Signal Synthesis

A non-moving signal receptor located immediately after the signal emitter sees the following signal

$$s_1(t) = \sum_{j=-\infty}^{\infty} Ac_j p_1\left(t - jT_C\right). \tag{8-68}$$

Where one (+1) chip of a BPSK signal at RF level -*the single chip function at RF level*- of the emitted signal can be written as

$$p_1(t) = \begin{cases} \cos(2\pi f_P t) & 0 \le t < T_C \\ 0 & \text{else} \end{cases} \tag{8-69}$$

and the whole signal can be reconstructed via proper convolution with the code data c_j. If Binary Offset Carrier (BOC) signals shall be tested, equation (8-69) must be modified to include also the rectangular subcarrier. It should be noted that also Sinusoidal Offset Carrier (SOC) signals, raised cosine signals or other modulation schemes can be handled in this way.

Note that a possible Doppler shift due to the motion of the receiver is of no importance to this investigation.

8.4.3 Signal Propagation

We assume that all aspects of signal propagation (including atmospheric effects, multipath, scattering, diffraction, …) are linear and time invariant and thus can be described by convoluting s_1 with a function H_1:

$$s_2(t)=\int_{-\infty}^{\infty} s_1(t')H_1(t-t')dt' . \tag{8-70}$$

$H_1(t)$ vanishes for $t<0$, since the process is causal. Inserting equation (8-68) into (8-70) yields

$$s_2(t)=\sum_{j=-\infty}^{\infty} Ac_j\, p_2(t-jT_C) \tag{8-71}$$

and

$$p_2(t)=\int_{-\infty}^{\infty} p_1(t'')H_1(t-t'')dt'' . \tag{8-72}$$

The specific form for H_1 will not be specified, instead p_2 will be calculated directly. If signal creeping shall be investigated, p_2 will be calculated by solving Maxwell's Equations numerically. The input to Maxwell's Equations is related to p_1.

It is important to note that p_2 needs not to vanish for $t>T_C$.

8.4.4 Down conversion

Bandpass filtering of the antenna input signal is included in H_1 (cf. equation (8-70)) since both operations (signal propagation and bandpass filtering) are represented by convolution operators and the product of two convolution operators is again a convolution.

Mathematically the multiplication with the carrier frequency is written as

$$\begin{aligned} s_3'(t) &= s_2(t)\exp(i2\pi f_P t) = \sum_{j=-\infty}^{\infty} Ac_j\, p_2(t-jT_C)\exp(i2\pi f_P t) = \\ &= \sum_{j=-\infty}^{\infty} Ac_j\, p_2(t-jT_C)\exp(i2\pi f_P (t-jT_C))\exp(i2\pi f_P jT_C) = \\ &= \sum_{j=-\infty}^{\infty} Ac_j\, p_3'(t-jT_C)\exp(i2\pi f_P jT_C) \end{aligned} \tag{8-73}$$

with

$$p_3'(t)=p_2(t)\exp(i2\pi f_P t) . \tag{8-74}$$

Lowpass filtering of the output signal of the multiplier is equivalent to a convolution with an appropriate Kernel H_3:

$$s_3(t)=\int_{-\infty}^{\infty} s_3'(t')H_3(t-t')dt' = \sum_{j=-\infty}^{\infty} Ac_j\, p_3(t-jT_C)\exp(i2\pi f_P jT_C) \tag{8-75}$$

with

$$p_3(t) = \int_{-\infty}^{\infty} p_3'(t') H_3(t - t') dt' . \tag{8-76}$$

The signal s_3 represents the output (IF) signal which is a complex signal. It is a convolution of the code sequence with the *single chip function* p_3 *at IF level*. From equation (8-75) and (8-76) one sees that the output for the whole code sequence of the GPS/APL receiver frontend can be reconstructed, if the single chip function p_3 at IF level is known.

It is important to note that this approach covers all possible signal propagation aspects and is computationally very efficient.